Characterization of 4H-SiC/High-κ Dielectric Interfaces via First Principles Calculations

by

Lu Wang

A dissertation submitted to the Graduate Faculty of
Auburn University
in partial fulfillment of the
requirements for the Degree of
Doctor of Philosophy

Auburn, Alabama
August 06, 2022

Keywords: Wide band gap semiconductors, Interface, high-κ dielectrics

Approved by

Marcelo A. Kuroda, Chair, Associate Professor of Physics
Sarit Dhar, Professor of Physics
Jianjun Dong, Professor of Physics
Yu Lin, Professor of Physics
Siyuan Dai, Assistant Professor of Mechanical Engineering

Abstract

For power electronic devices, wide band gap (WBG) semiconductors are most attractive owing to their excellent physical properties, that they can sustain much higher voltages, frequencies, and temperatures than conventional semiconductors. As the most common power device, the metal–oxide–semiconductor field-effect transistor (MOSFET) has been driving the rapid exponential growth of modern semiconductor technology since the 1960s. With continuous development of device optimization and improvements in the production process, MOSFET fabricated based on the Si is reaching its performance limit. Instead, 4H-SiC has become prevalent for power device applications. However, the greatest challenge in 4H-SiC MOSFET is the low channel mobility that is primarily attributed to the poor SiC/SiO_2 interface quality. Various chemical treatments have been adopted to reduce the interface trap densities, the channel mobility is still low. Alternatively, using high-κ dielectrics with suitable band gaps to replace the conventional SiO_2 as gate insulators is a promising approach for improving the SiC device performance.

In this study, we first produce an array of realistic models of the (0001) Si-face of the 4H-SiC with SiO_2 using first principles calculations within the density functional theory (DFT) to understand the role of nitrogen in the improvement of the SiC/SiO_2 interface. Electron density profiles of the model interfaces match those obtained by X-ray reflectivity (XRR), suggesting that nitridation of the interfaces from NO annealing yields a higher Si density near the interfaces. Moreover, we find that the addition of N stabilizes the interface by reducing strain with no introduction of interfacial gap states. Subsequently, we screen high-κ dielectrics for 4H-SiC MOSFETs using first principles calculations within the DFT and identify alkaline earth metal fluorides AF_2 (A = Mg and Ca) and LiF as promising high-κ/large band gap dielectrics candidates. The properties of model interfaces formed using similar approaches to those of SiC/SiO_2 systems, as well as the 4H-SiC/Al_2O_3 interface models are analyzed and the band offsets of these 4H-SiC/high-κ dielectrics interfaces are compared against limited experimental data. We

find that O terminated 4H-SiC (0001) surface is advantageous to LiF/4H-SiC and AF$_2$/4H-SiC (A = Ca and Mg) interfaces in reducing mid-gap states. We note that both H and N passivated Al_2O_3/4H-SiC interfaces effectively remove the mid-gap states. Lastly, we investigate other alternative high-κ dielectrics for 4H-SiC, such as MgO and $Mg_xCa_{1-x}O$. The electronic band structures of MgO/4H-SiC and $Mg_xCa_{1-x}O$/4H-SiC heterostructures are analyzed as well as the band offsets. Overall, this work offers insights on the potential use of alternative high-κ dielectric materials in wide band gap electronic applications.

Acknowledgments

First and foremost, I would like to express my sincere gratitude to my advisor Dr. Marcelo A. Kuroda for his continuous support, priceless advice, and being the best mentor during my Ph.D study at Auburn University.

Most of our work together would not be possible without the financial backing of the US Army Research Lab, National Science Foundation, and the computational resources of Auburn's Hopper and Easley Clusters.

I greatly appreciate all my committee members Dr. Sarit Dhar, Dr. Jianjun Dong, Dr. Yu Lin, and Dr. Siyuan Dai for their valuable time and advice.

I am thankful to our collaborators Dr. Sarit Dhar and Dr. Leonard Feldmann for their assistance in our paper on 4H-SiC/SiO_2 interface, and Dr. Masoud Mahjouri-Samani for involving us in their paper on WSe_2 biosensor.

Special thanks go to my colleagues Dr. Isanka Udayani Jayawardhena, Dr. Ryan Thorpe and Dr. Xiuyan Li for their selfless help with my questions, fruitful discussions and sharing experimental data.

I want to thank the members within my research group, Jonathan Heath, Adam Pfeifle and Dakotah Kirk, as well as all my classmates for their friendship and help.

I am so grateful for all my family in China for their prayer and unconditional love for me during these trying times. Last but not the least, I want to thank my loving husband and best friend Yufeng for his endless support and sincere love, and our adorable little boy Cosmo baby. This work is for you. Mama loves you forever.

Table of Contents

List of Figures

List of Tables

List of Abbreviations

2D	Two-dimensional
3D	Three-dimensional
AFM	Atomic force microscopy
ALD	Atomic layer deposition
AX_2	Alkaline earth metal dihalides
BCO	Base-centered orthorhombic
BZ	Brillouin zone
CBM	Conduction band minimum
CUB	Cubic
DFT	Density Functional Theory
DOS	Density of states
EDMR	Electrically detected magnetic resonance
FCC	Face-centered cubic
FET	Field effect transistor
GGA	Generalized gradient approximation
GS	Gaussian smoothing

HEG Homogeneous electron gas

HEX Hexagonal

HF Hartree-Fock

HK Hohenberg–Kohn

HSE Heyd–Scuseria–Ernzerhof

KS Kohn–Sham

LAMMPS Large-Scale Atomic/Molecular Massively Parallel Simulator

LDA Local density approximation

LDOS Local density of states

LEED Low energy electron diffraction

LOD Limit of detection

MBE Molecular beam epitaxy

MD Molecular dynamics

MOSFET Metal–oxide–semiconductor field effect transistor

MUA 11-mercaptoundecanoic acid

ORT Primitive orthorhombic

PAW Projector augmented wave

PBE Perdew–Burke-Ernzerhof

PBS Phosphate-buffered saline

PDOS Projected density of states

PLV Primitive lattice vector

POA Post oxidation annealing

REELS Reflection electron energy loss spectroscopy

SAM Self-assembled monolayer

SG Space group

SiON Silicon-oxynitride

STD Standard deviation

TET Tetragonal

TMDC Transition metal dichalcogenide

TR Transition region

TRI Triclinic

VBM Valence band maximum

vdW van der Waals

WBG Wide Band Gap

XPS X-ray photoelectron spectroscopy

XRR X-ray reflectivity

Chapter 1

Introduction

1.1 Wide Band Gap Semiconductors

1.1.1 Background

Power electronics have penetrated almost all fields where the conversion of electric power is involved, from our daily life to military defense and aerospace. They can be widely used as switching power supply, DC motor drivers, power factor correction, and so on. The conventional silicon (Si) technology has been dominant in power electronics for many years but is reaching its performance limits in new emerging applications [20]. Therefore, the key for the next step towards the next-generation power electronics lies in the use of new semiconductors endowed with superior physical properties than Si.

In comparison with the conventional semiconductors whose band gap are in general below 2 eV, wide band gap (WBG) semiconductors have larger band gaps allowing them to sustain higher voltages, frequencies, and temperatures [21]. In fact, the wide band gap factor is particularly important for permitting devices to operate at high temperatures. The band gap decreases with the increasing temperatures. The device made with a WBG semiconductor can continue to function in much higher temperatures, on the order of 300 °C [22]. Withstanding the higher temperatures, it can also operate at much higher power. Moreover, most WBG materials also have high drift velocity that is directly representing high frequency switching capabilities. In light of these intrinsic properties, WBG semiconductors become the ideal options for power electronics with greater power efficiency and harsh environment tolerance.

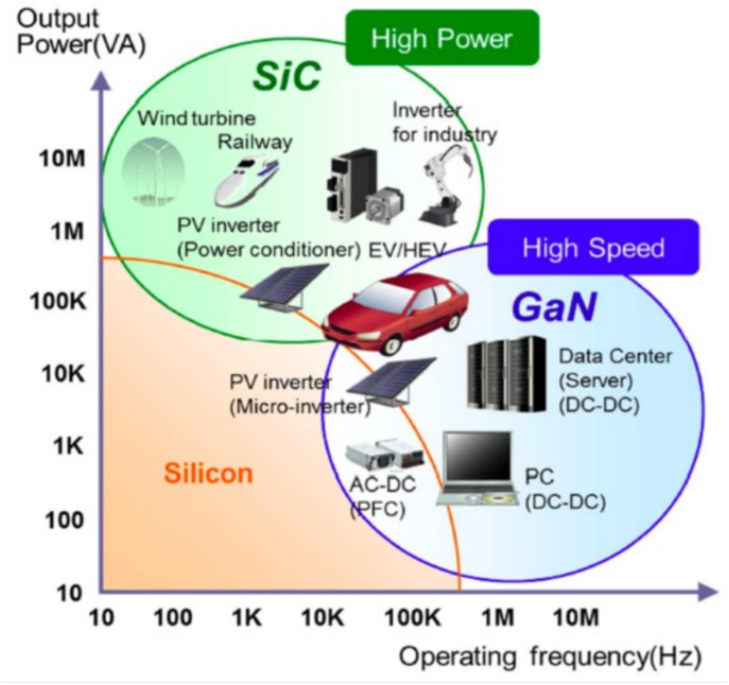

Figure 1.1: Possible power electronics applications of GaN and SiC from the aspects of output power and operating frequency, adapted from [1].

1.1.2 Wide Band Gap Semiconductors for Power Electronics

Many IV materials, III-V, II-VI compound semiconductors and oxides such as Boron Nitride (BN), Aluminum Nitride (AlN), Zinc Oxide (ZnO) and $\beta-Ga_2O_3$ are WBG materials. The current research focus is the WBG materials such as Silicon Carbide (SiC), Gallium Nitride (GaN) and Diamond. Though diamond has ultra wide band gap as well as excellent thermal conductivity, the relevant research is still in the early stages. Figure 1.1 [1] shows the possible applications of GaN and SiC in future market when compared to Si. Both GaN and Si are constricted in the low and medium range of the output power, but GaN can work at relatively high operating frequencies that makes it suitable for electric power conversion, such as AC to DC rectifiers, DC to AC inverters, DC to DC and AC to AC converters circuits. In contrast, the target of SiC is higher output power making it ideal for generation of power switching devices.

The unique advantages of SiC and GaN over Si are shown in Fig. 1.2 [2]. The SiC dominates the high-voltage range (above $\sim$1000 V) and high-temperature applications due to its high thermal conductivity, high melting point, and wide band gap, along with the low defect density

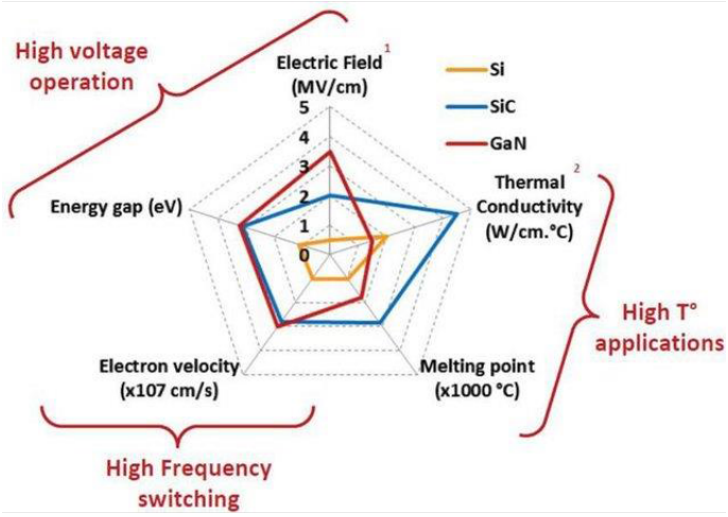

Figure 1.2: Comparison of the figures of merit of Si and WBG semiconductors SiC and GaN, adapted from [2].

in the bulk that is not shown here. The overwhelming performance in high frequency switching of GaN is resulted from its high carrier mobility. Current GaN on Si substrates via epitaxial growth technology operate well only at mid-range voltage range and has been prevented from operating at higher voltages. For instance, the breakdown voltage of GaN transistors is merely up to 1000 V, which is attributed to its high defect density. Without appealing unique properties as the WBG semiconductors, Si is not competitive in the high-voltage and high-temperature condition, in particular at the high frequency switching [2, 23].

Table 1.1: Physical properties of Si and several common WBG semiconductors [13].

Properties	Si	4H-SiC	GaN	Diamond
Band gap E_g (eV)	1.12	3.26	3.45	5.45
Dielectric constant ϵ_r	11.9	10.1	9	5.5
Electric breakdown field E_c (kV/cm)	300	2200	2000	10000
Electron mobility μ_n (cm^2/V·s)	1500	1000	1250	2200
Hole mobility μ_p (cm^2/V·s)	600	115	850	850
Thermal conductivity λ (W/cm·K)	1.5	4.9	1.3	22
Baliga's figure of merit (BFM)	1	223.1	186.7	25106

The Properties of Si and some common WBG semiconductors are shown in Table 1.1 [13]. Here the Baliga's figure of merit (BFM) measures the specific on-resistance ($R_{on-ideal}$) (per unit area) of the drift region of a vertical field effect transistor (FET). The specific $R_{on-ideal}$ corresponds to the resistive energy loss in the ideal material that can be impacted by the physical

properties of semiconductors. Thus, BFM is given by Eq. 1.1 [24]:

$$BFM = \epsilon_r \mu_n E_c^3 = \frac{4B_V^2}{R_{on-ideal}} \tag{1.1}$$

where ϵ_r is the dielectric constant of semiconductor, μ_n is the electron mobility, E_c is the electric breakdown field, and B_V is the desired breakdown voltage. Based on the definition, E_c has a larger impact on the BFM due to the cubic factor.

WBG semiconductors are expected to revolutionize the power electronics at high power and high frequencies. Both SiC and GaN are important at present, although each of them offers unique advantages over the other. This work is focused on discussion of SiC-based platforms and its performance improvement via different aspects.

1.2 Silicon Carbide

Silicon carbide (SiC) is a WBG semiconductor compound containing silicon and carbon. The Si and C atoms in the crystal are linked by strong tetrahedral covalent bonds sharing electron pairs in sp^3 hybrid orbitals. The natural occurrence of SiC is extremely rare as mineral moissanite. Despite its rareness, SiC is found substantially common in space and in meteorites. Hence, the majority of SiC in the market is synthetic in various processes after the first SiC was grown by Edward G. Acheson in 1890 [25].

1.2.1 Crystal Structure

SiC can exist in more than 250 different structures called polymorphs, that have been identified by 2006 [26]. Apart from various amorphous forms of SiC in thin film and fibers [27], a large number of similar crystalline structures called polytypes are also observed. These polytypes remain the same chemical compound but differ in the stacking sequences of the basic SiC bilayer component [28]. Therefore, they can be viewed as closely stacked layers with two identical dimensions but different third dimension.

Three most common SiC polytypes are shown in Fig. 1.3 [3]. They are hexagonal SiC (6H- and 4H-SiC) and cubic SiC (3C-SiC, also known as β-SiC). The number in the definition

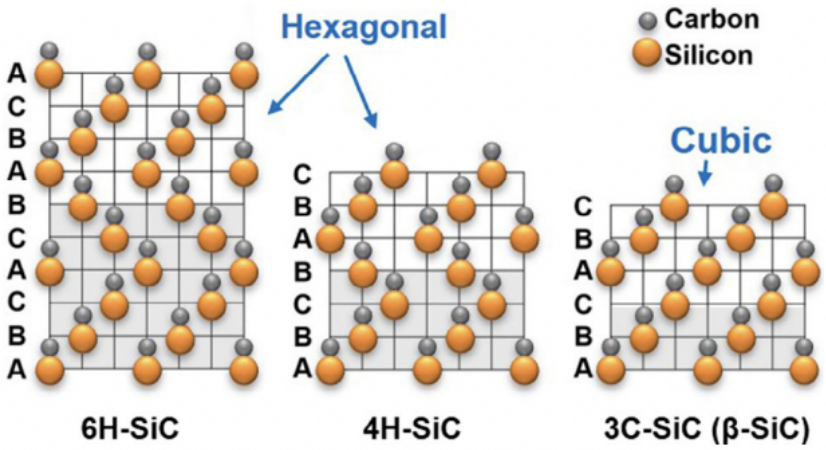

Figure 1.3: The stacking sequence of three most commonly SiC polytypes, 6H-SiC, 4H-SiC, and 3C-SiC, adapted from [3].

originates the number of SiC bilayers in the staking sequence. For instance, in the unit cell of 6H-SiC, the SiC bilayers along the third (vertical as shown) direction are stacked in a repeated sequence ABCACB. The stacking sequences of 4H-SiC and 3C-SiC are ABCB and ABC, respectively. Here, A, B, and C label the atoms' configuration in the layers.

1.2.2 Physical Properties

As described in Section 1.2.1, both 6H- and 4H-SiC have a wurtzite (hexagonal) structure and 3C-SiC has a zincblende (cubic) structure. A polarization is spontaneously generated in the direction [0001] of the wurtzite structure. Hence, two polar faces (the Si-face and C-face) would posse higher planar charge density than the bulk. The properties of those SiC polytypes are shown in Table 1.2 [14], compared with those of silicon. As discussed prior, SiC is more beneficial than Si for enhancement of device performance at high voltage due to the larger band gap. Among the polytypes, 4H-SiC has larger band gap and higher breakdown field than the 6H-SiC and 3C-SiC, that results in higher breakdown voltage for a fixed thickness of device active layer. Based on Eq. 1.1, higher breakdown field allows drastic reduction of $R_{on-ideal}$, and correspondingly the power loss. Furthermore, 4H-SiC has low intrinsic carrier concentration at room temperature, which effectively prevents the leakage currents even in high-temperature operations. Thus, we are convinced that 4H-SiC is more desirable for power electronics applications.

Table 1.2: Physical properties of Si and the most common SiC polytypes in comparison with those of Si, adapted from [14].

Properties	Si	6H-SiC	4H-SiC	3C-SiC
Band gap E_g (eV)	1.12	3.08	3.26	2.35
Breakdown field E_c (kV/cm) (at N_D = 5$\times$ 10^{15} /cm)	300	2200	2300	1500
Intrinsic carrier concentration n_i (/cm^3) (at T=300 K)	1.0×10^{10}	1.6×10^{-6}	5×10^{-9}	1.5×10^{-1}
Electron mobility μ_n (cm^2/V·s)	1350	370	800	900
Hole mobility μ_p (cm^2/V·s)	480	80	120	40
Saturated electron velocity v_s (10^7 cm/s)	1	2	2	2
Thermal conductivity λ (W/cm·K)	1.5	4.9	4.9	4.9
Dielectric constant ϵ_r	11.8	9.7	9.7	9.6
Electron affinity (eV)	4.05	3.3	3.1	3.8

The significance of the wide band gap for SiC has been fully emphasized. The dependence of band gap on temperature is also worth a discussion, as shown in Fig. 1.4 [4]. The band gap of SiC polytypes decreases as temperature increases. This is because the interatomic spacing increases and less energy is needed to break a bond, leading to a smaller potential seen by electrons in the materials. In addition, SiC can be doped with different impurities to form n- or p-type semiconductor. Figure 1.5 [5] shows the variations of band gap (the energy distance between the valence band and conduction band shifts) versus doping density. The band gap narrowing of n-type 4H-SiC is evidently larger than that of 6H-SiC at high donor concentrations (left). In contrast, the p-type SiC polytypes have almost the same band gap narrowing for a fixed acceptor concentration (right).

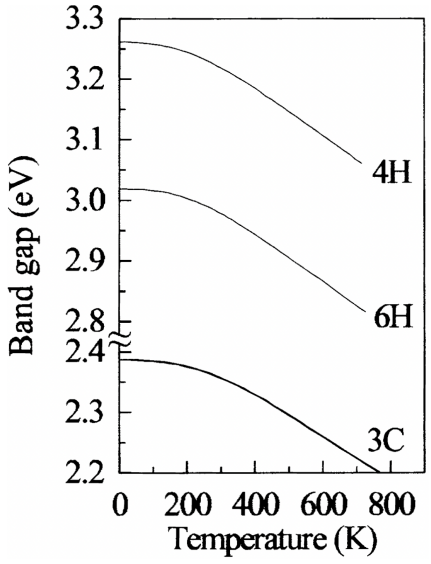

Figure 1.4: The band gap of SiC polytypes versus temperature [4].

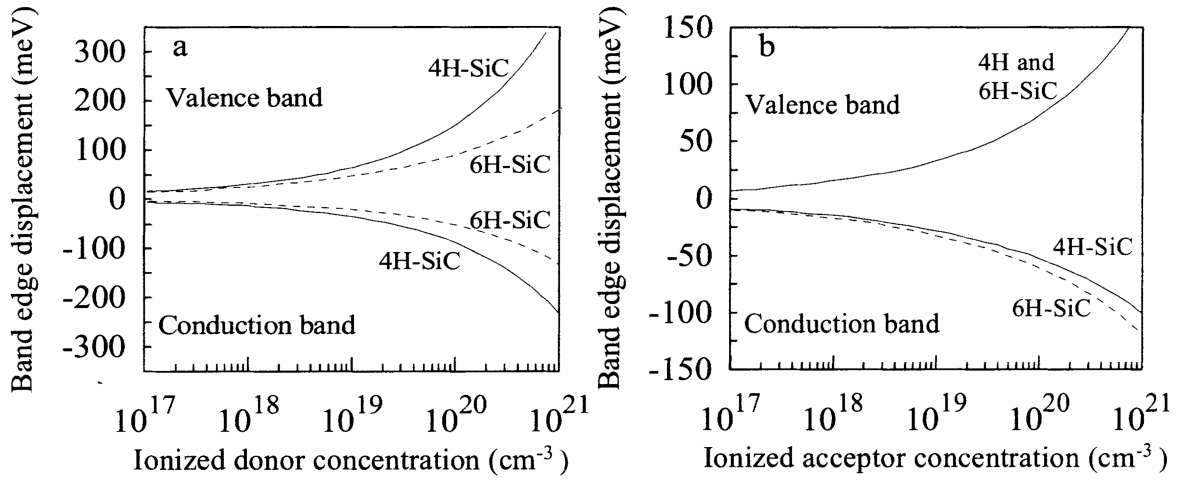

Figure 1.5: Conduction band (in the lower half) and valence band shifts (in the upper half) for 4H– and 6H–SiC versus ionized donor concentration in purely (a) n-type and (b) p-type material, adapted from [5].

1.3 Metal–Oxide–Semiconductor Field Effect Transistor

Metal–oxide–semiconductor field effect transistor (MOSFET) is the most widely used semiconductor device [29] functioning as the core component in an integrated circuit [30] since its first appearance in 1960. The MOSFET is commonly used as a small signal linear amplifier or a switch in power electronics. It is available in very small size and easy to manufacture on a mass-production basis. There is no doubt that the development of MOSFET is driving the rapid growth of electronic semiconductor technology.

1.3.1 Device Structure

A MOSFET is a four-terminal device that is comprised of source (S), gate (G), drain (D) and body (B) terminals. The S and B terminals are usually connected to the ground. The basic MOSFET structure is shown schematically in Fig. 1.6. The gate electrode (metal material or polysilicon) is electrically isolated from the body substrate by an insulating layer. If a dielectric material other than an oxide is inserted between the gate and body, the device is referred more precisely as a metal-insulator-semiconductor field effect transistor (MISFET). The S and D terminals are connected to individual highly doped regions between which the conduction channel is formed. The current flowing through the channel can be modulated by the voltage

applied to the gate. Hence, A MOSFET acts like a resistor where the current is changing with the controlled gate voltage, leading to its use for amplifying or switching electronic signals.

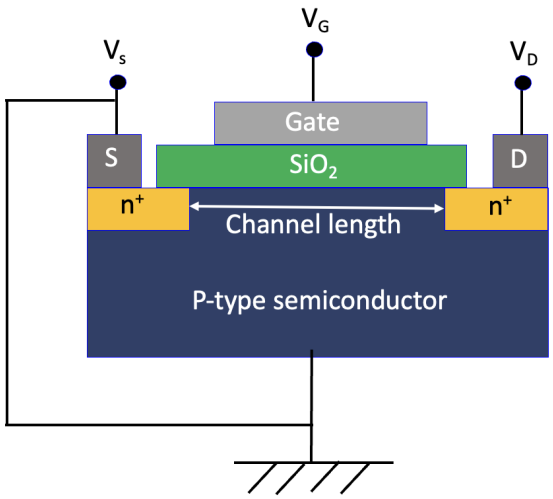

Figure 1.6: Schematic of a (n-channel) MOSFET.

The MOSFET is classified into two types based on the majority charge carriers in the conduction channel. The electrons (holes) flow in the n-channel (p-channel) MOSFET. Accordingly, the two regions connected to S and D terminals are n-type (p-type) and the semiconductor body is p-type (n-type). The conventional MOSFET is fabricated typically by the controlled oxidation process of Si. During this process, the gate dielectric silicon dioxide (SiO_2) can be easily grown on Si substrate.

1.3.2 Modes of Operation

A MOSFET can function in two different modes: depletion mode and enhancement mode. The former is less common than the latter. The depletion MOSFET is a ”normally closed” device in which the channel conducts even without an applied gate voltage. In contrast, the enhancement MOSFET is normally “OFF” when the gate voltage is equal to zero. The device has to be turned on by a non-zero gate voltage. Namely, a positive gate voltage turns on the n-channel enhancement mode MOSFET; in contrast a negative gate voltage makes the p-channel enhancement mode MOSFET conduct. Figure 1.7 [6] shows that for n-channel enhancement mode MOSFET the conductivity (as shown in current I_D) is enhanced with a positive gate voltage (V_{GS}) with different values.

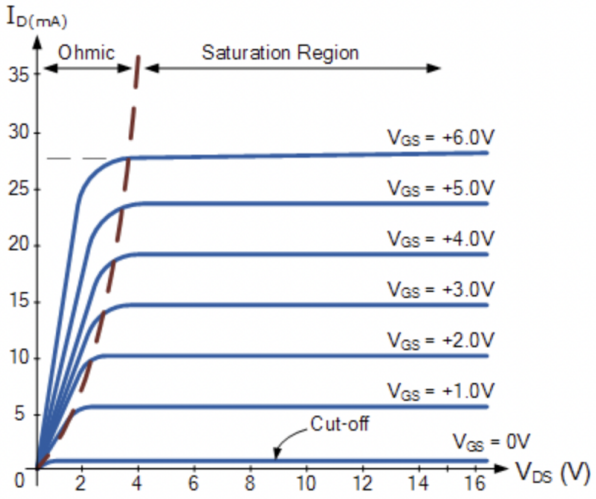

Figure 1.7: The current through the channel I_D for n-channel enhancement mode MOSFET versus the source to drain voltage V_{DS} at different gate voltages V_{GS}, adapted from [6].

1.4 Interface Defects

The 4H-SiC based MOSFET has been recognized as an excellent candidate for power electronics due to its wider band gap and higher breakdown field than Si as discussed earlier. 4H-SiC also shares SiO_2 as the native oxide with Si. Therefore, the mature Si technology can be easily applied to enable the design of SiO_2/4H-SiC interface. However, the dominant factor that limits the implementation of 4H-SiC based MOSFET is the poor quality of the SiO_2/4H-SiC interface. The channel mobility for devices fabricated with oxidized 4H-SiC is very low, typically less than 10 $cm^2/V{\cdot}s$ [31], despite its high bulk mobility.

Previous reports have ascribed the low channel mobility to the high densities of interface states near the SiO_2/4H-SiC interface [32, 33, 34, 35]. When compared to SiO_2/Si interface that has defect density of below $10^{10}/cm^2{\cdot}eV$, the interface states of the SiO_2/4H-SiC interface are found to be order of $10^{11}/cm^2{\cdot}eV$ in the middle of the band gap and $10^{13}/cm^2{\cdot}eV$ within $\sim 0.05-0.2$ eV of the conduction band edge [36, 37]. The distribution of defect states for 4H-SiC MOS devices is illustrated in Fig. 1.8, adapted from [7]. It has been agreed upon that the π-bonded carbon clusters and dangling bonds are responsible for the mid-gap states, whereas the intrinsic defects in SiO_2 very close to the interface, so called near-interface traps and π-bonded carbon clusters are the main reason for the interface states near the conduction band edge [38, 39, 40, 41, 42, 43, 44, 45, 46, 47, 48]. The SiC MOS devices are mainly

n-channel designed, thus the acceptor-like near-interface traps have the most impact on the channel conductivity because they can result in charge trapping and Coulomb scattering [49].

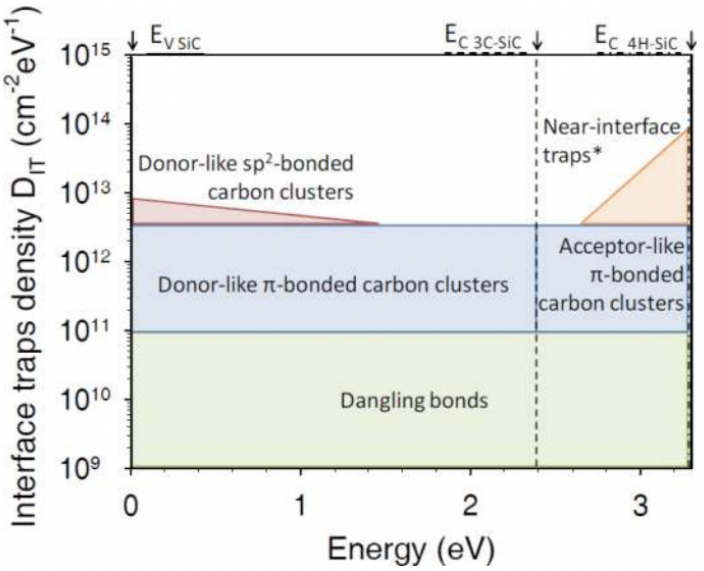

Figure 1.8: Interface trap density versus energy, adapted from [7].

.

1.5 Motivations

1.5.1 Nitrogen-induced Changes in The Properties of SiO_2/4H-SiC Interfaces

The 4H-SiC MOS devices performance is limited by the high densities of interface states. Considerable efforts have been made to measure quantitatively the densities of interface defects and ascribe the interface states in a certain energy range in the band gap to certain type of defects. However, it is incredibly difficult to identify all the defects as a result of the highly disordered interface structures obtained in experiments. Hence, systematic studies of the SiO_2/4H-SiC model interfaces are essential to understand the atomic configurations of the interfaces and qualitatively characterize the resulting properties.

Simultaneously, various surface treatments have been employed to passivate the defects of high densities, such as wet or dry oxidation [50, 51], using doped gate oxide [52], nitridation including either post oxidation annealing [53, 54, 55, 56, 57, 58, 59, 60, 61, 62, 63, 64, 65, 38, 66, 67, 68] or combined oxidation/annealing [69, 70]. Nitridation has become the most reliable and effective treatment by experiments. However, it is found that the channel mobility is still

low. Therefore, with the realistic SiO_2/4H-SiC model interfaces, understanding the effects of nitrogen atoms on the electronic and structural properties of SiO_2/4H-SiC model interfaces might provide us a good starting point for upgrading the device performance via effectively improving the chemical treatments.

1.5.2 Alternative High-κ Dielectrics for 4H-SiC

The SiO_2 can be easily grown on 4H-SiC, but it is not precisely qualified as a good gate dielectric for 4H-SiC. Aside from the high densities of interface states near the SiO_2/4H-SiC interface, the physical properties of SiO_2 itself also hinder the full advantages of 4H-SiC for power electronics. As a result of size-scaling in 4H-SiC based MOSFET, the thickness of SiO_2 film becomes so thin. However, this thin oxide layer is insufficient to effectively prevent the gate leakage current due to direct tunnelling of electrons. Thus it is desirable to replace SiO_2 as a gate oxide for 4H-SiC. The leakage current decreases with increasing thickness of gate dielectric film. The central part of a MOSFET is the MOS structure (see Fig. 1.6). The insulating dielectric is adjacent to the semiconductor substrate. According to Gauss' law, the electric field in the MOS structure can be expressed as:

$$E_{ins} = \frac{\epsilon_s}{\epsilon_{ins}} E_s \tag{1.2}$$

where the ϵ_s (ϵ_{ins}) is the dielectric constant of the 4H-SiC (insulator), and E_s (E_{ins}) is the electric field in the 4H-SiC (insulator) [71, 72]. The dielectric constant of 4H-SiC (ϵ_s =9.7) is $\sim$2.5 times higher than that of SiO_2 (ϵ_{ins} =3.9). Thus, the breakdown of SiO_2 would occur before that of 4H-SiC because the electric field in SiO_2 is $\sim$2.5 times higher than 4H-SiC. The MOS device will experience breakdown below the critical electric field of 4H-SiC. As a result, the advantages of 4H-SiC are not demonstrated if the gate dielectric has a much lower dielectric constant than 4H-SiC. Hence, using alternative high-κ dielectrics to replace SiO_2 as the gate dielectric for 4H-SiC is beneficial for device operation at high voltage. From the perspective of

the MOS capacitance, that is simply the capacitance of a parallel plate capacitor:

$$C = \epsilon_{ins} \frac{A}{d} \tag{1.3}$$

where A is the area of plates and d is the thickness of the gate insulator. If we desire to achieve a capacitance equivalent as in SiO_2, the MOS capacitor can be made thicker using a dielectric with higher dielectric constant than SiO_2. Consequently, the device performance is advanced because of smaller gate leakage current due to thicker dielectric film.

1.6 Thesis Outline

The goal of this work is to characterize the properties of the interfaces formed by 4H-SiC (0001) and oxides (and dielectrics) using first principles calculations within Density functional theory (DFT). Understanding the nitrogen effect on the SiO_2/4H-SiC interfaces reveals the mechanisms of chemical treatments which in turn help further improve the device performance. Moreover, identifying promising alternative high-κ dielectrics as the suitable gate dielectrics for 4H-SiC offers a different path for upgrading the device performance and reliability.

In Chapter 2, the methodologies employed to calculate the properties of crystals are discussed, including the density functional theory (DFT) and electrostatic potential-based alignment method. In Chapter 3, the role of nitrogen in the SiO_2/4H-SiC interfaces is investigated via large scale first-principles calculations within DFT. The electric and structural properties of a series of SiO_2/4H-SiC model interfaces are also computed. In Chapter 4, alternative high-κ dielectric candidates are identified from high throughput screening of alkaline earth metal dihalides (AX_2) formed by alkaline earth metal (A = Mg, Ca, Sr and Ba) and halogen (X = F, Cl, Br and I). The stable phases, band gaps and dielectric constants of AX_2 are computed within DFT framework. In Chapter 5, the electrical properties of the model interfaces between 4H-SiC and the candidate high-κ dielectrics are characterized within DFT framework. Different surface passivation methods are employed to form those model interfaces and the relation between the properties and atomic configurations of intefaces are discussed. In Chapter 6, the MgO/4H-SiC and $Mg_xCa_{1-x}O$/4H-SiC heterostructures are formed to study their electronic properties. The

band offsets of the heterostructures are estimated. In Chapter 7, the conclusions of this work are summarized and the future work is also described.

Chapter 2

Methodology

2.1 Summary

In this Chapter, we describe the density functional theory employed through this work to characterize the properties of bulk materials and interface models, as well as Hartree and Hartree-Fock methods for solving the many-body problem in solids. We also introduce the electronic band structure and crystal lattice (both direct and reciprocal lattice). Furthermore, the post-calculation analysis of data is discussed that includes the search of epitaxial relation between two materials for heterostructure building, computing the macroscopic average of electron density profiles, and evaluating the band alignments using electrostatic potential-based alignment method.

2.2 The Many-body Problem and Hartree-Fock Method

A solid is a collection of atoms that are composed of heavy nuclei and lighter electrons bound to the nuclei. The prediction of the properties of systems from the first principles calculations, requires solving the many-body problem. The Born-Oppenheimer approximation [73] made the first simplification that the electronic and nuclear degrees of freedom are separated, which is justified by that the electrons are much less massive and move much faster than the nuclei. Thus, the Hamiltonian for many-electron system is written as Eq. 2.1

$$\hat{H} = \hat{T} + \hat{V} + \hat{V}_{ext} \tag{2.1}$$

where $\hat{T}$ corresponds to the kinetic energy of the electron gas, $\hat{V}$ is the potential energy due to electron-electron interactions, and $\hat{V}_{ext}$ refer to the potential energy of the electrons in the (now external) potential of the nuclei. The first two terms are universal but $\hat{V}_{ext}$ is dependent on the specific system.

Hartree approach simplifies the problem by assuming the form of the many-electron wavefunction is the product of many single-electron wavefunctions. The Hamiltonian of the system can be found using the variational principle. Nonetheless, this approach does not produce particularly good results, as a result of ignorance of the Pauli exclusion principle. In other words, the product wavefunction is symmetric.

As an improvement, Hartree-Fock (HF) method writes the ground state wavefunction as a slater determinant of single particle orbitals [74, 75, 76, 77, 78]. In such way, the wavefunction is more complicated but now antisymmetric. The energy of the system is evaluated by the sum of the one-electron Fock operator, $\hat{F}[\phi_j](1)$ generated by the orbitals ϕ_j, that is outlined below:

$$\hat{F}[\phi_j](1) = \hat{H}^{core}(1) + \sum_{j=1}^{N/2}[2\hat{J}_j(1) - \hat{K}_j(1)] \tag{2.2}$$

where the expectation value of one-electron core Hamiltonian $\hat{H}^{core}(1)$ produces the single electron kinetic energy and potential energy due to N_α atomic nuclei:

$$\hat{H}^{core}(1) = -\frac{1}{2}\nabla_1^2 - \sum_\alpha \frac{Z_\alpha}{r_{1\alpha}} \tag{2.3}$$

Also, the Coulomb operator $\hat{J}_j(1)$ defines the electron–electron repulsion energy due to each of the two electrons in the j_{th} orbital, and the exchange operator $\hat{K}_j(1)$ defines the electron exchange energy as a consequence of the Pauli exclusion principle.

The HF method has proven to produce more creditable results for small molecules but fails for solids. The reason is that this method ignores the electrostatic correlation effect that originates the correlated motion of electrons, though the exchange effect has been taken into account.

2.3 Density Functional Theory

Density functional theory (DFT) is based upon Hohenberg-Kohn (HK) theorems [79] that state, for an interacting many-body system, the one-to-one correspondence between the external potential V_{ext} and the ground state density $\rho(\mathbf{r})$ which minimizes the energy of the system. Thus based on Eq. 2.1, the ground state energy functional $E[\rho(\mathbf{r})]$ can be written as an unique functional of $\rho(\mathbf{r})$:

$$E[\rho(\mathbf{r})] = F[\rho(\mathbf{r})] + \int \rho(\mathbf{r}) V_{ext}(\mathbf{r}) d\mathbf{r} \tag{2.4}$$

where $F[\rho(\mathbf{r})]$ = $T + V$ is called HK density functional that is unknown and universal for any many-electron system. Until 1965, the Kohn-Sham (KS) equation [80, 81] decomposes $F[\rho(\mathbf{r})]$ explicitly into several contributions to the total energy. Therefore, the total energy of a Kohn–Sham system is expressed below:

$$E[\rho] = T_s[\rho] + E_H[\rho] + E_{xc}[\rho] + \int \rho(\mathbf{r}) V_{ext}(\mathbf{r}) d\mathbf{r} \tag{2.5}$$

where T_s is the non-interacting (single particle) kinetic energy, E_H is the Hartree (or Coulomb) energy, and E_{xc} is the exchange-correlation energy. Here, the exact ground-state density $\rho(\mathbf{r})$ of an N-electron system is given by the single-electron wavefunction ϕ_i:

$$\rho(\mathbf{r}) = \sum_{i=1}^{N} \phi_i(\mathbf{r})^* \phi_i(\mathbf{r}) \tag{2.6}$$

By invoking the variational principle, the KS equation is solved in a self-consistent way, as shown in Fig. 2.1 [8]. Provided that the closer the initial guess of $\rho(\mathbf{r})$ is to the correct wave function, the less the number of iterations is.

2.3.1 Local Density Approximation

To solve for the KS equation, approximations have to be made for the exchange-correlation energy $E_{xc}(\rho)$. The simplest approximation is the local density approximation (LDA), assuming that the exchange-correlation energy depends solely upon the local density at a point $\mathbf{r}$, which

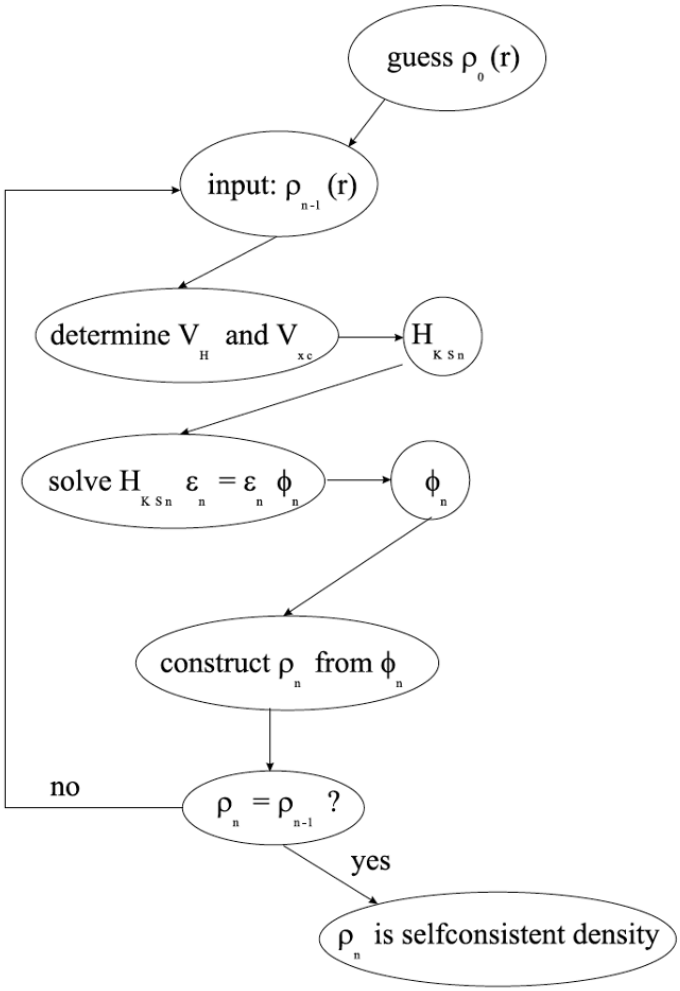

Figure 2.1: Flow chart of self-consistent procedure to solve the Kohn-Sham equation, adapted from [8].

may be expressed as an explicit functional of $\rho(\mathbf{r})$ [80]:

$$E_{xc}^{LDA}(\rho) = \int \rho(\mathbf{r})\epsilon_{xc}^{HEG}[\rho(\mathbf{r})]d\mathbf{r} \tag{2.7}$$

$$= \int \rho(\mathbf{r})\epsilon_{x}^{HEG}[\rho(\mathbf{r})]d\mathbf{r} + \int \rho(\mathbf{r})\epsilon_{c}^{HEG}[\rho(\mathbf{r})]d\mathbf{r} \tag{2.8}$$

$$= E_{x}^{LDA}(\rho) + E_{c}^{LDA}(\rho) \tag{2.9}$$

where $\epsilon_{xc}^{HEG}(\rho(\mathbf{r}))$ represents the exchange-correlation energy per particle of a homogeneous electron gas (HEG) of density $\rho(\mathbf{r})$. The exchange energy functional $E_{x}^{LDA}(\rho) \sim \rho(\mathbf{r})^{4/3}$ [82] and the correlation energy functional $E_{c}^{LDA}(\rho)$ can be extrapolated numerically from analytical

low and high density limits [83, 84] and quantum Monte Carlo results [85, 86, 87, 88] for intermediate densities. The LDA in general produces smaller band gap values because the simple assumption of uniformity in LDA underestimates the exchange energy while overestimating the correlation energy [79, 89].

2.3.2 Generalized Gradient Approximation

Another approximation to the $E_{xc}(\rho)$ is the generalized gradient approximation (GGA), which depends not only on the local density but also on the density in the neighbouring volumes (the gradient of the density) that can be expressed as:

$$E_{xc}^{GGA}(\rho) = \int \rho(\mathbf{r})\epsilon_{xc}^{GGA}[\rho(\mathbf{r}), \nabla\rho(\mathbf{r})]d\mathbf{r} \tag{2.10}$$

where $\epsilon_{xc}^{GGA}[\rho(\mathbf{r}), \nabla\rho(\mathbf{r})]$ is the gradient expanded single particle exchange-correlation function. This is a further improvement on LDA via a gradient correction which helps describe the inhomogeneity in the electron density. The Perdew-Burke-Ernzerhof (PBE) functional [90] remains the most popular choice among GGA because it is a non-empirical functional and produces results with reasonable accuracy over a wide range of systems. In comparison with the LDA that is known to overbind, the GGA tends to overcorrect LDA's overbinding and overestimate the cell parameters [91, 92]. Both LDA and GGA in general produce smaller band gap than experiment.

2.3.3 Heyd–Scuseria–Ernzerhof Functional

The Heyd–Scuseria–Ernzerhof (HSE) screened hybrid functional[93] is a common hybrid approach that approximates the $E_{xc}(\rho)$ in DFT by incorporating a certain amount of the HF exchange with the rest of exchange–correlation energy from other sources. The HSE functional is an adaptation of the PBE0 functional which mixes the exact non-local HF exchange with the exchange from PBE, where only short-range HF exchange but no long-range HF exchange is mixed. The reason for avoiding the effect of long-range HF exchange is the exact-exchange energy converges very slowly with the distance for periodic systems, the short range screened

Coulomb potential enables higher electron localization which in turn improves the electronic band structure calculations. The most general form of the HSE functional is expressed in Eq. 2.11:

$$E_{xc}^{\omega PBEh} = \alpha E_x^{HF}(\omega)\Big|_{SR} + (1-\alpha)E_x^{PBE}(\omega)\Big|_{SR} + E_x^{PBE}(\omega)\Big|_{LR} + E_c^{PBE}(\omega) \qquad (2.11)$$

where ω is the screening length, and α is the mixing parameter, which is 0.25 in the PBE0 functional. The HSE calculation produces better results in band gap for most systems when compared to the LDA or GGA. However, computational cost of the HF portion scales as N^4 (where N is the number of electrons) instead of N^3 of DFT [94]. This poor scaling makes the study of the systems using hybrid approaches computationally prohibitive.

2.4 Electronic Band Structure

The electrons in an isolated atom occupy only discrete energy levels. When two atoms are brought together very closely, the electrons from two atoms interact with each other via overlapping their atomic orbits. In the two-atom system, the energy levels of electrons will split into closely spaced two energy levels. Similarly, the electrons of N atoms in a solid interact, causing each energy level to split into closely spaced N energy levels. As N is a very large number, the energy of the adjacent levels is so close together to form a continuous energy band [95]. The bands represent the available electronic states, while band gap is an energy range where no electronic states can exist. The Fermi energy refers to the highest energy level that an electron can occupy at the absolute zero temperature. Metals exhibit no band gap at the Fermi energy, semiconductors exhibit a small band gap and insulators exhibit large band gap [96]. Hence, the electronic band structure is used to visualize the wavevector-dependence of the energy levels that electrons may have and not have within it, the band-gap, as well as electronic transition.

2.5 Crystal Lattice

The arrangement of atoms in a crystal is described by the crystal (Bravais) lattice that spans the entire space by the repetition of unit cell in different directions. For any three-dimensional

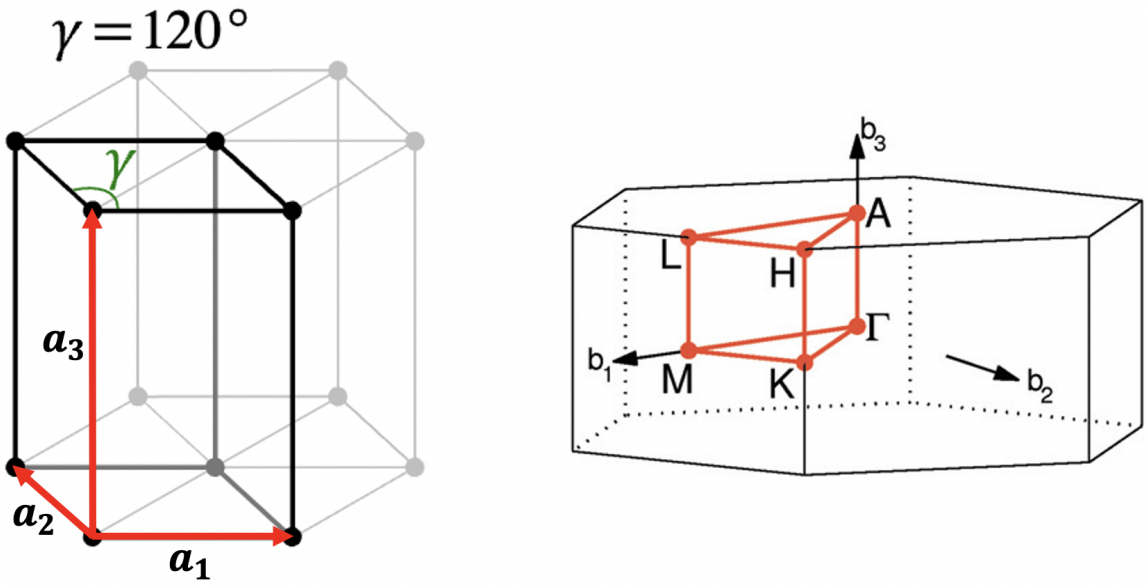

Figure 2.2: (Left) The unit cell of hexagonal lattice, where $\mathbf{a_x}$ (x = 1,2,3) are the primitive lattice vectors, and γ is the angle between $\mathbf{a_1}$ and $\mathbf{a_2}$. (Right) The first Brillouin zone (BZ) of hexagonal lattice, where $\mathbf{b_x}$ (x = 1,2,3) are the reciprocal lattice vectors. The high-symmetry $\mathbf{k}$ points Γ, M, K, A, L and H are also shown [9].

(3D) lattice, the unit cell is a parallelepiped defined by a set of lattice parameters (length and angles) [97]. As one of the fourteen Bravais lattices, the hexagonal (HEX) unit cell is shown in Fig. 2.2 (left). The angle between the primitive lattice vectors $\mathbf{a_1}$ and $\mathbf{a_2}$ is 120°, while the primitive lattice vectors $\mathbf{a_1} \perp \mathbf{a_3}$ and $\mathbf{a_2} \perp \mathbf{a_3}$. Due to the periodicity of the lattice, electrons in a crystal may be subjected to a periodic potential. Bloch theorem states that the eigenfunctions (also known as Bloch states) of the Schrödinger equation for a periodic potential can be written as the product of a plane wave $e^{i\mathbf{k}\cdot\mathbf{r}}$ and a function $u_{\mathbf{k}}(\mathbf{r})$ with the same periodicity as the crystal lattice [98]:

$$\varphi_{\mathbf{k}}(\mathbf{r}) = e^{i\mathbf{k}\cdot\mathbf{r}} u_{\mathbf{k}}(\mathbf{r}) \tag{2.12}$$

where $\mathbf{k}$ is the crystal momentum vector. Similar to the concept of unit cell in Bravais lattice, $\mathbf{k}$ can be restricted to the first Brillouin zone (BZ) of the reciprocal lattice [99]. The Brillouin zone of HEX lattice is shown in Fig. 2.2 (right) [9], where the reciprocal lattice vectors $\mathbf{b_x}$ (x= 1,2,3) traces three sides of the unit cell of the reciprocal lattice.

Based on the Bloch theorem, for the same $\mathbf{k}$, the eigenstates can vary with the periodic component $u_{\mathbf{k}}(\mathbf{r})$, resulting in a more accurate expression $\varphi_{n\mathbf{k}}(\mathbf{r})$ in which n is the band index.

Within a band, $\varphi_{n\mathbf{k}}(\mathbf{r})$ is dependent on $\mathbf{k}$. Consequently, the eigenvalue corresponding to each band varies with $\mathbf{k}$, which requires sampling the BZ. Although $\mathbf{k}$ is a 3D vector, it is common just to visualize the eigenvalues along special high-symmetry directions. As shown in Fig. 2.2 (right), the first BZ for HEX lattice can be sampled along the path: Γ-M-K-Γ-A-L-H-A. The electronic band structure of 4H-SiC is shown in Fig. 2.3, where the band gap (∼2.2 eV) is underestimated by DFT calculation using PBE functional. In order to visualize the contribution to the overall electronic band structure by different atoms, the projections of Bloch states onto localized atomic orbitals of C (yellow) and Si (blue) are superimposed on the total band structures. The size of the markers are scaled based on the magnitude of the total atomic projections. The full density of states (DOS) across the whole BZ rather than just the special directions is shown as well.

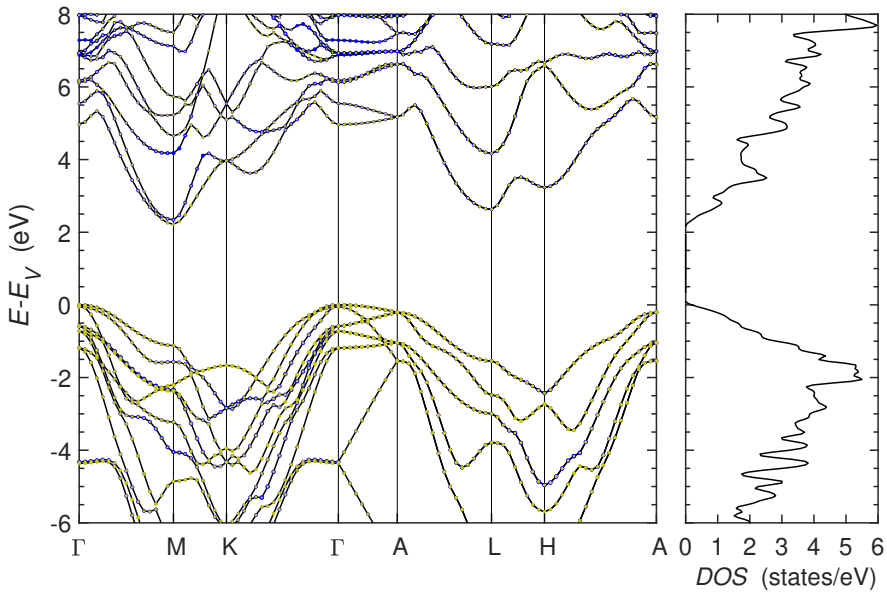

Figure 2.3: Electronic band structure of 4H-SiC and corresponding density of states (DOS). The projections of Bloch states onto localized atomic orbitals of C (yellow) and Si (blue) superimposed on the total band structures are plotted as markers.

2.6 Epitaxy

In order to theoretically characterize the properties of an interface (or heterostructure), noted as A/B that is an overlayer of crystalline material A deposited onto material B, the supercell of

the interface model is built based on an epitaxial relation found from the lattice match between material A and B.

We develop a code in MATLAB to create the supercell of interface model by searching the epitaxial relation between material A and B. This epitaxial relation refers to that the resulting primitive lattice vectors (PLVs) $\mathbf{a}'_x$ (x = 1,2,3) of slab A (or B) in the heterostructure A/B supercell are expressed in terms of the original PLVs $\mathbf{a}_x$ (x = 1,2,3) of the unit cell of bulk material A (or B). Here the parameters matrix representing $\mathbf{a}'_x$ (x = 1,2,3) is denoted as [n_1^1 n_2^1 n_3^1;n_1^2 n_2^2 n_3^2;n_1^3 n_2^3 n_3^3], which links $\mathbf{a}'_x$ and $\mathbf{a}_x$(x = 1,2,3) in a linear relationship. More specifically, the epitaxial relation is given by Eq. 2.13:

$$\mathbf{a}'_x = n_1^x \mathbf{a}_1 + n_2^x \mathbf{a}_2 + n_3^x \mathbf{a}_3 \tag{2.13}$$

The code automatically check the epitaxies under the constraint of several aspects, such as tolerance of the angle difference between the resulting in-place lattice vectors $\mathbf{a}'_1$ and $\mathbf{a}'_2$, in-plane lattice constants a and b, the number of atoms in slab A and B and so on. Figure.2.4 illustrates an epitaxy that accommodates the 2×2 supercell of material A on top of material B. The original unit cell of material A (B) shown in red (green) square are constructed by the PLVs $\mathbf{a}_1$ and $\mathbf{a}_2$. A compressive strain is applied to the 2×2 supercell of material A. Thus the two sides of the resulting supercell (red dashed squares) overlap with the diagonals of the unit cell of material B. It is evident that the slab A must rotate in counterclockwise a small angle before the overlapping.

Once we are content with the lattice strain and size of supercell associated with the epitaxy, the heterostructure is then built using the geometry files of material A and B according to the selected epitaxial relation. In the building process, we can set the in-plane lattice constants of the desired heterostructure to those of substrate material B while a lateral tensile or compressive strain is applied to material A. For example, the formation process of a SiO_2/4H-SiC interface is shown in Fig 2.5. The primitive unit cells of bulk β-cristobalite SiO_2 (ICSD 162246) and 4H-SiC (ICSD 164971) are traced by the primitive lattice vectors. The heterostructure as shown is built with a $\sim$4% tensile strain applied to the SiO_2 slab. The SiC slab are formed based on the

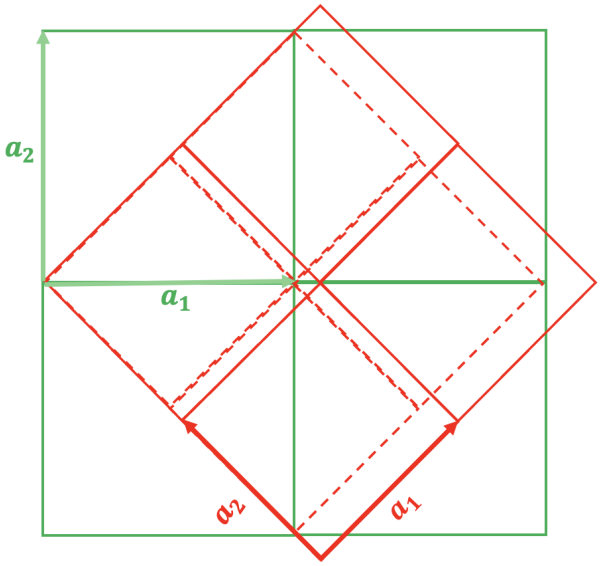

Figure 2.4: Schematic of an epitaxy that accommodates the 2×2 supercell of material A (red) on top of material B (green). The unstrained supercell is shown in solid squares while the strained supercell is shown in dashed square. The primitive lattice vectors $\mathbf{a}_1$ and $\mathbf{a}_2$ are color coded based on materials.

parameters matrix [4 1 0; 3 4 0; 0 0 -2] and SiO_2 slab follows the parameters matrix [2 -1 0; 2 1 0; 3 3 6]. In Chapter.3, we present a different epitaxy using this SiO_2 and 4H-SiC with a lower strain.

2.7 Electron Density

In Chapter 3, the electron charge density profiles of SiO_2/4H-SiC interfaces are computed in comparison with those obtained from experiment. In order to determine the electronic density profile $\rho_e(z)$ across the interface from our first principles calculations, we account for both valence and core electrons:

$$\rho_e(z) \equiv \rho_c(z) + \rho_v(z) \tag{2.14}$$

Contributions from localized core electrons of all atoms are included as Gaussian distributions:

$$\rho_c(z) = \frac{1}{\sqrt{2\pi} A\, \sigma} \sum_i Z_i^c e^{-\frac{(z-z_i)^2}{2\sigma^2}}, \tag{2.15}$$

where Z_i^c is the core charge of the i-th atom ($Z_i^c \equiv 0$ for H, 2 for C, O and N, and 10 for Si atom), z_i is the z-position of the i-th atom, and A represents the surface area of the supercell.

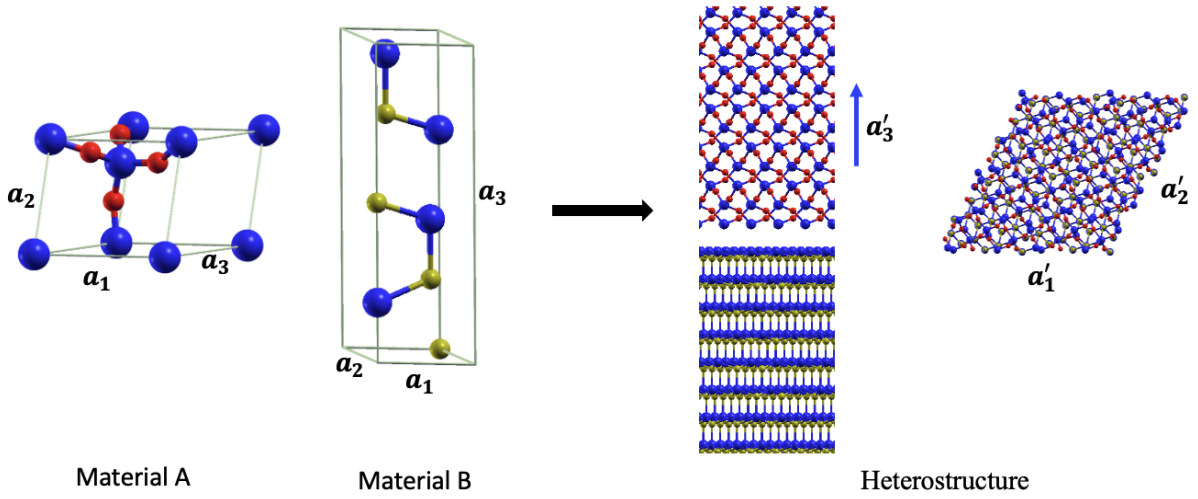

Figure 2.5: The unit cell of A/B heterostructure built from the unit cell of crystal A and B, where the unit cells of crystals are defined by their primitive lattice vectors (PLVs) $\mathbf{a}_x$ (x = 1,2,3). The PLVs $\mathbf{a}'_x$ (x = 1,2,3) of slab A and B in the heterostructure are obtained using Eq. 2.13.

Likewise, the valence electron density profile $\rho_v(z)$ is obtained by averaging the local electron density of valence electrons from DFT $\rho_{\text{DFT}}(\mathbf{r})$ over the surface and smoothed along the z-direction using a Gaussian smoothing (GS):

$$\rho_v(z) = \iiint \rho_{\text{DFT}}(\mathbf{r}')e^{-(z'-z)^2/2\sigma^2}\, dx'dy'dz' \tag{2.16}$$

The broadening σ is chosen by minimizing the dispersion of electron densities that would yield an uniform density in the bulk.

As an example, for one of the interfaces built with 4H-SiC and β-cristobalite form of silica (ICSD 162246), named as model 3 in next chapter, the breakdown of the valence and core electron density is shown in Fig 2.6. The variation of $\rho_{\text{DFT}}(\mathbf{r})$ is shown along the direction z perpendicular to the interface, plotted in solid black as a planar average of the $\rho_{\text{DFT}}(\mathbf{r})$. This planar-averaged potential exhibits periodic oscillations along the z direction due to the spatial distribution of the electrons and ionic cores. After GS described in Eq. 2.16, this oscillations are replaced by a smoother curve in black dash representing the $\rho_v(z)$. The core electrons in this system have integer charges that are highly localized. Similarly, the core electron density profiles ($\rho_c(z)$) are smoothed out based on Eq. 2.15, as shown in black dotted. As expected,

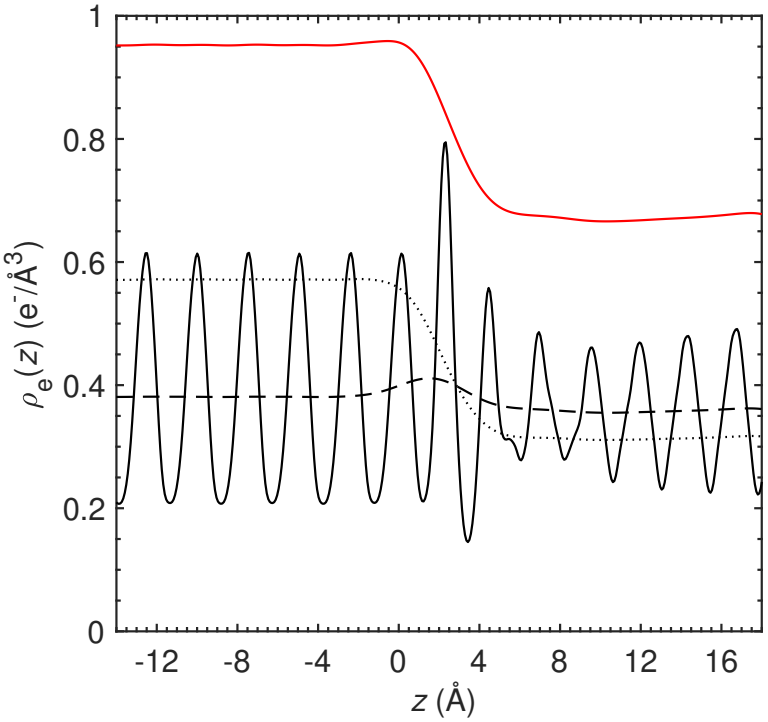

Figure 2.6: For interface model 3: valence electron density profile (black solid line) prior to GS, valence electron density profile after GS (black dashed line), core electron density profile after GS (black dotted line), and the total electronic density profile as a function of z. The broadening σ used in the smoothing is 1.6 Å, according to the bulk analysis.

the macroscopically averaged electron density (after GS) in both SiC and silica bulk regions is constant, and indeed it reaches a plateau value in the bulk-like regions of the interface. Lastly, the sum of the $\rho_v(z)$ and $\rho_c(z)$ is compared to the electron density profiles of SiO_2/SiC interface measured from XRR. Here, the broadening σ = 1.6 Å.

As already mentioned, the broadening σ is determined from the analysis of electron density for silica bulk, as shown in Fig 2.7. The average volume densities of valence ($\langle\rho_v(z)\rangle$ = 0.361 e$^-$/Å^3) and core ($\langle\rho_c(z)\rangle$ = 0.316 e$^-$/Å^3) electrons are constant values for the specific interface system. For both valence and core electrons, the variation of macroscopically averaged electron density from the average volume density is dependent on the choice of σ. Consistently, we observe the oscillations when σ is picked far from satisfactory. Therefore, one more step that is taken to identify the optimal σ is calculating the standard deviation (STD) of data points of both $\rho_v(z)$ and $\rho_c(z)$. The result is plotted in the bottom of Fig. 2.7. A set of σ values results in low STD indicating that values of both $\rho_v(z)$ and $\rho_c(z)$ are clustered close to their mean. In

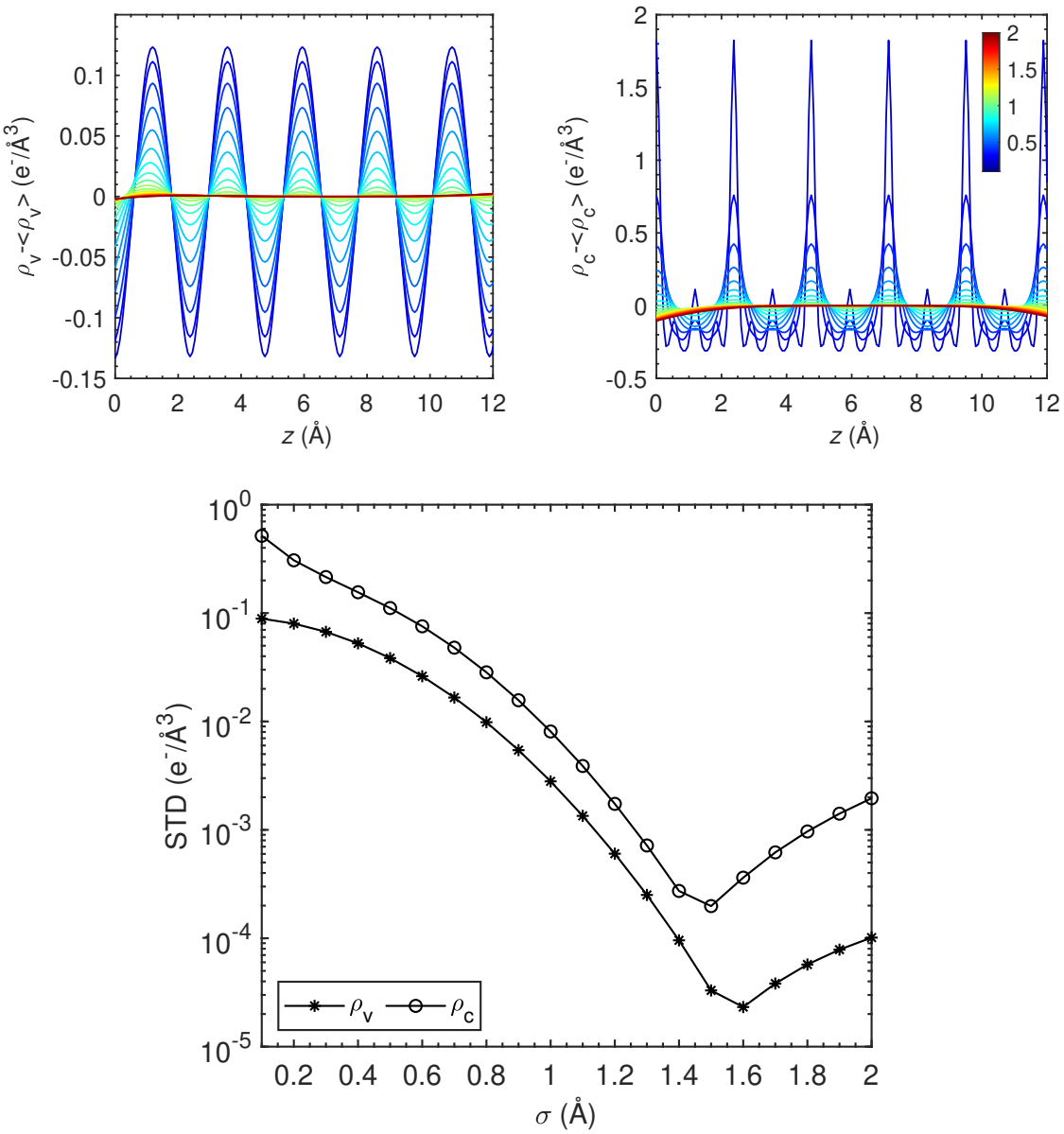

Figure 2.7: For interface model 3: (Top Left) Valence electron density profile ($\rho_v(z) - \langle\rho_v(z)\rangle$) after Gaussian smoothing using different σ, as a function of z; (Top Right) Core electron density profile ($\rho_c(z) - \langle\rho_c(z)\rangle$) after Gaussian smoothing using different σ, as a function of z, where $\langle\rho_v(z)\rangle$ and $\langle\rho_c(z)\rangle$ are the average volume densities of valence and core electrons, respectively. The color bar refers to the values of σ in unit of Å. (Bottom) Standard deviation (STD) of electron density versus σ. The optimal value is chosen σ = 1.6 Åwhen STD of ρ_v is seen at the lowest.

the end, we choose σ = 1.6 when the STD of ρ_v is found at the lowest among those σ that are verified.

2.8 Band Alignment

For heterostructures of interest in the forthcoming Chapters 3, 5, and 6, the valence band (ΔE_V) and conduction band (ΔE_C) offsets can be accurately and efficiently evaluated using first principles calculations within the DFT framework. This approach is performed by aligning the local band edges with respect to the local electrostatic potential [100, 101]. That is to say, the band edge alignment of the bulk A and B that comprise the heterostructure A/B, is achieved through a potential-alignment term from an explicit heterostructure A/B calculation. This methodology that combines DFT and the screened hybrid HSE functional [102, 93] offers improved descriptions of the band gaps to overcome well-known limitations of DFT [103].

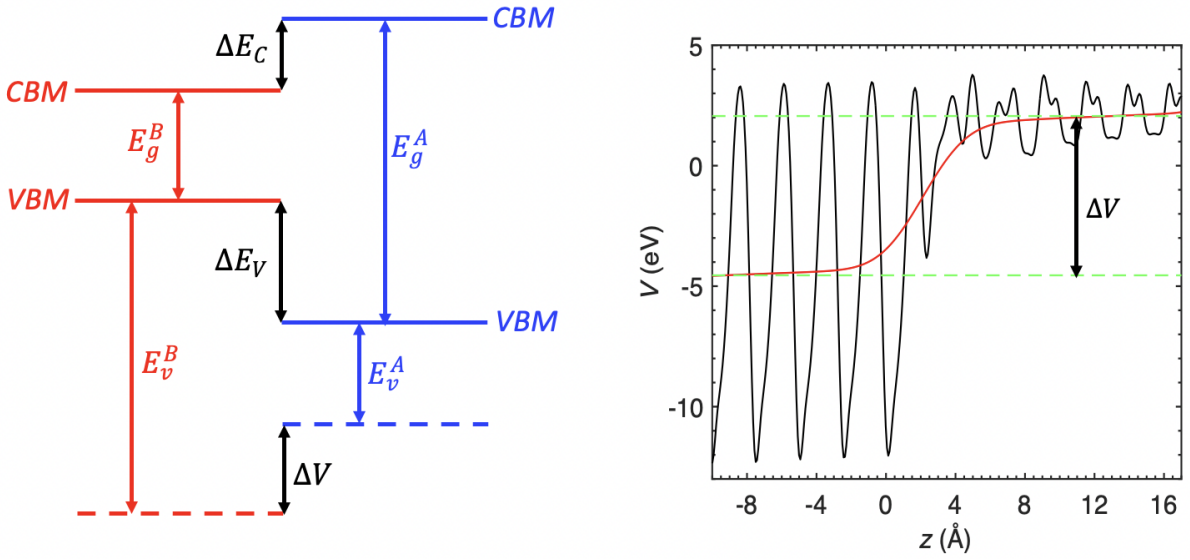

Figure 2.8: (Left) Schematic of band alignment between material A and B that comprise heterostructure A/B. The band edge with respect to the local electrostatic potential E_v^A and E_v^B, the band gaps E_g^A and E_g^B are obtained from separate bulk calculations using HSE functional. The potential alignment ΔV is found from superlattice calculation. The band offsets (ΔE_V) and (ΔE_C) are derived from Eq. 2.17 and Eq. 2.18, respectively. (Right) Planar-averaged (black solid line) and macroscopically averaged electrostatic potential (red dash line) for SiO_2/4H-SiC interface system.

The method is conducted in three steps as illustrated in Fig. 2.8. First, we perform separate HSE calculation for bulk materials A and B, in which produces valence band maximum (VBM)

and conduction band minimum (CBM) with respect to the average electrostatic potential in the respective material. Here, the HSE mixing parameter is optimized to bring the calculated band gap (E_g^A and E_g^B) in agreement with experimental value. Second, the alignment of the average electrostatic potential is determined between the two materials from an explicit heterostructure calculation. The macroscopic average of the electrostatic potential is found via applying similar smoothing procedure for the electron density as already discussed in Section 2.7 to planar potentials of corresponding models. The proper reference for aligning valence and conduction bands is obtained by calculating the difference (ΔV) between the macroscopic average of potentials in the bulk-like regions of material A and B from standard DFT calculations with taking dipole correction into account. Hence, the thickness of each material in the superlattice is large enough to contain a bulk-like region. We do not employ HSE calculation for the heterostructure because it will be extremely computationally expensive for structure with large unit cell. Lastly, the band edges between material A and B can be aligned via the potential-alignment term ΔV. The local valence band edges of material A and B with respect to their local electrostatic potential are denoted as E_v^A and E_v^B, correspondingly. ΔE_V can be easily derived via Eq. 2.17 once the potential alignment is known:

$$\Delta E_V = (E_v^B - E_v^A) - \Delta V \tag{2.17}$$

Subsequently, ΔE_C is determined according to Eq. 2.18 by using band gaps from the respective bulk calculations:

$$\Delta E_C = E_g^B - E_g^A - \Delta E_V, \tag{2.18}$$

To give an illustration of the determination of ΔV, Fig. 2.8 (right) also demonstrates the macroscopic average of potentials (red) across a SiO_2/4H-SiC interface. The planar-averaged electrostatic potential (black) converges to its bulk value within two or three atomic layers of the interface, which was found in common for other interface systems studied by [101].

2.9 Computational Details

The results presented in following chapters are obtained by performing first principles calculations within the DFT that are carried out using the Quantum Espresso software [104]. Unless otherwise noted, we employ the Perdew-Burke-Ernzerhof (PBE) parameterization of the exchange-correlation functional [90] including dispersion forces (vdW-DF-C09) [105, 106, 107, 108]. Description of core electrons is performed with projector augmented wave (PAW) pseudopotentials [109]. Due to periodic boundary conditions assumed in all three dimensions, a vacuum space of at least 12 Å along the z-direction is set to prevent interactions with periodic repetitions of the supercell of interfaces. Atomic positions are fully relaxed until the forces become smaller than 0.005 eV/Å. The supercells account for the dipole correction [110] to minimize surface effects. The formation of SiO_2 amorphous structure and classical molecular dynamics (MD) annealing of interfaces are performed in the Large-Scale Atomic/Molecular Massively Parallel Simulator (LAMMPS) [111]. All calculations are performed on the Hopper and Easley Clustes.

Chapter 3

SiO_2/SiC Interfaces

3.1 Summary

In this chapter, we analyzed the changes in the electron density profiles and strain upon the introduction of nitrogen in 4H-SiC (0001)/SiO_2 interfaces using first-principles calculations with the density functional theory (DFT). By comparing systems with different geometric and atomic compositions, we find that nitrogen preferably forms a Si_3-N structure (1 N atom is bonded to 3 Si atoms) and stabilizes the interface by reducing the abruptness of Si density between SiC and silica. Our calculations confirm that the unexpected reduction in the electron density observed in X-ray reflectivity (XRR) experiments at the as-grown 4H-SiC/SiO_2 interface is removed upon nitridation. The shorter interatomic distances in nitrided systems and the higher atomic density near the interface help alleviating the local strain. Analysis of the electronic band structures in these nitrided interface models reveals alignments comparable to those found experimentally and the presence of nitrogen that creates interface states near the valence band edge.

3.2 Background

Chemical treatments of interfaces have proven important to the achievement of high-quality interfaces between 4H-SiC and dielectric materials for wide band gap semiconductor applications [38, 66]. Easily grown interfaces with the SiC native oxide, SiO_2, can present a high density of interface states that largely degrades performance of power devices by reducing carrier mobility and changing the threshold voltage [32, 33, 34, 35]. The C face of 4H-SiC

shows much larger channel mobility ($\sim$100 $cm^2/V{\cdot}s$) when wet oxidation or hydrogen incorporation is involved. In contrast, the interface state density near the conduction band has shown much higher value on the Si face of 4H-SiC resulting in much lower channel mobility [112]. Therefore, the improved carrier mobilities after post oxidation annealing (POA) of 4H-SiC/SiO_2 interfaces, particularly on the 4H-SiC (0001), in N-rich conditions (N_2, NO or N_2O) [53, 54, 55, 56, 57, 58, 59, 60, 61, 62, 63, 64, 65, 38, 66, 67, 68] or combined oxidation/annealing [69, 70] have led to the adoption of the nitridation process in the production of SiC power electronics applications. The underlying mechanism of this process, however, is still elusive despite the considerable efforts made to date in modeling these interfaces [113, 114, 115, 41, 116, 117], with suggested mechanisms ranging from healing of dangling bonds to removal of interstitial C atoms [38, 39, 40, 41, 42, 43, 44, 45, 46, 47].

Owing to the large number of silica polymorphs and amorphous structures attained experimentally, describing silica interfaces to SiC with adequate atomic configurations is challenging. Previous studies on the effects of nitrogen in SiC grown under ultra-high vacuum conditions were based on thin epitaxial silicon-oxynitride (SiON) layers [115, 41, 116]. These models contained a monolayer of O atoms on the 4H-SiC (0001), that was later confirmed by X-ray photoelectron spectroscopy (XPS) [118, 119]. However, N-rich annealing processes employed in device processing typically give nitrogen areal densities smaller than those of epitaxial SiON layers. More recent models, incorporating nitrogen amounts associated with device processes, have been limited to ultra-thin SiO_2 layers [43]. Yet, theoretical atom-level descriptions are needed to establish a correlation between nitridation and physical properties of these interfaces as reported in recent experiments [10, 67] and envision novel mechanisms to systematically improve properties arising from chemical treatments.

3.3 Crystal Structures

In order to provide an interpretation to the electron density variations observed in XRR measurements, we created an array of models to the 4H-SiC/SiO_2 interfaces. The models differ in the atomic configuration of the transition region (TR) that must accommodate the silicon density mismatch between the SiC and the oxide. Each model contains slabs of 4H-SiC (0001)

and an extended silica layer of approximately 20 Å thickness each, yielding about 250 atoms in the unit cell, as illustrated in Fig. 3.1(a). For the oxide we chose the β-cristobalite form of silica that gives low epitaxial mismatch with 4H-SiC ($\sim$1%) for the supercells considered here and has a mass density (2.18 g/cm^3) close to the experimental value (2.2 g/cm^3) of amorphous silica (a-SiO_2). The 4H-SiC slab consists of 3×3 unit cell arrangement, with in-plane lattice constants $a = b = 9.28$ Å. For each model we form a defect-free TR, beginning with a monolayer of O atoms on SiC (0001), featuring schemes previously proposed [115, 41] and supported by XPS observations [118, 119]. Different atomic arrangements combining O, Si, N, and H form the $<$1 nm thick suboxide TR. This agrees with the earlier report that nitrogen is confined to within 1 nm of the surface [43]. The C and O atoms at the end are H-passivated. A vacuum space of approximately 18 Å along the z-direction prevents interactions with periodic repetitions of the supercell.

In addition to the computational details described in Section 2.9, the wave functions and density are expanded in a plane-wave basis set using an energy cutoff of 60 Ry and 500 Ry, respectively. The self-consistent electron density is determined using $4\times4\times1$ Monkhorst-Pack k-point grid [120] with the Quantum Espresso suite [104]. To confirm the lowest phase of the relaxed models, we also perform classical molecular dynamics (MD) annealing of the models in the Large-Scale Atomic/Molecular Massively Parallel Simulator (LAMMPS) [111] using the optimized Reactive force field ReaxFF [121, 122]. The models are slowly heated to 1000 K using the canonical ensemble, where the annealing process is maintained at 1000 K for 200 ps. During the simulation, the Si and O atoms of the oxide are allowed to evolve whereas the substrate is kept frozen. The structures generated in this way are adopted for the calculations of the structural and electronic properties using DFT.

3.4 Interface Formation Energy

For a given supercell, we evaluate the interface formation energy (E_{if}) from the DFT calculations as [123]:

$$E_{if} = E_f - E_0 - \sum_i n_i \mu_i \tag{3.1}$$

In this equation, E_f is the total energy of the fully relaxed supercell after changing its composition while E_0 is the energy of a reference supercell. The quantities μ_i and n_i denote the chemical potential of i-species (i = Si, C, O, N and H) and the corresponding number of atoms that has been added to (n_i >0) or removed from (n_i <0) the reference interface. The reference chemical potentials depend on the experimental conditions, and choices usually represent specific limits.

In this work we adopt the choices previously used for 4H-SiC/SiO_2 interfaces [124] for the C-poor and O-poor regime, or the Si-poor and O-poor regime. The values of the reference chemical potential for different elements μ_i established from the DFT ground state energies of crystals/molecules as follows: $\mu_{\text{Si}} = E_{\text{Si}}/2$ for C-poor condition (or $\mu_{\text{C}} = E_{\text{C}}/4$ for Si-poor), $\mu_{\text{C}} + \mu_{\text{Si}} = E_{\text{SiC}}$, $\mu_{\text{O}} = (E_{\text{SiO}_2} - \mu_{\text{Si}})/2$, $\mu_{\text{N}} = E_{\text{N}}/2$, and $\mu_{\text{H}} = (E_{\text{SiH}_4} - \mu_{\text{Si}})/4$, where E_{Si}, E_{C}, E_{SiC}, E_{SiO_2}, E_{N}, and E_{SiH_4} are the DFT energies of diamond Si, graphite, 4H-SiC, bulk β-cristobalite SiO_2, N_2 and SiH_4 molecule per formula unit, respectively. The nitrogen reference is chosen because nitridation is either produced through N_2 or NO during post oxidation annealing processes [38, 66, 67, 68]. Additionally, other reference chemical potential choices (e.g. N and O) that could impact our results are discussed in the Appendix B.

3.5 Electron Density

3.5.1 Non-nitrogen Passivated SiO_2/SiC Interfaces

First, we consider the 4H-SiC/SiO_2 interfaces without nitrogen. For the epitaxies of our supercells, we created interfaces whose TR accommodate between 3 or 4 Si atoms to compensate for bonds originating in the semiconductor and the oxide slabs. From the different configurations created for such interfaces, model 1 with 3 Si atoms, as illustrated in Fig. 3.1(b), in the TR were thermodynamically more favorable. (For the remainder of this work we use this interface, model 1, as the reference one in Eq. 3.1.) Model 2 with 4 atoms in the TR presented formation energies E_{if} at least 1.5 eV higher than those of model 1, depicted in Fig. 3.1(c).

For the geometric arrangement of model 1, we analyze the electron density profile $\rho_e(z)$ along the z-direction (perpendicular to the interface), as presented in Fig. 3.1(d). The profile is established by computing the macroscopic average that includes both the core and valence

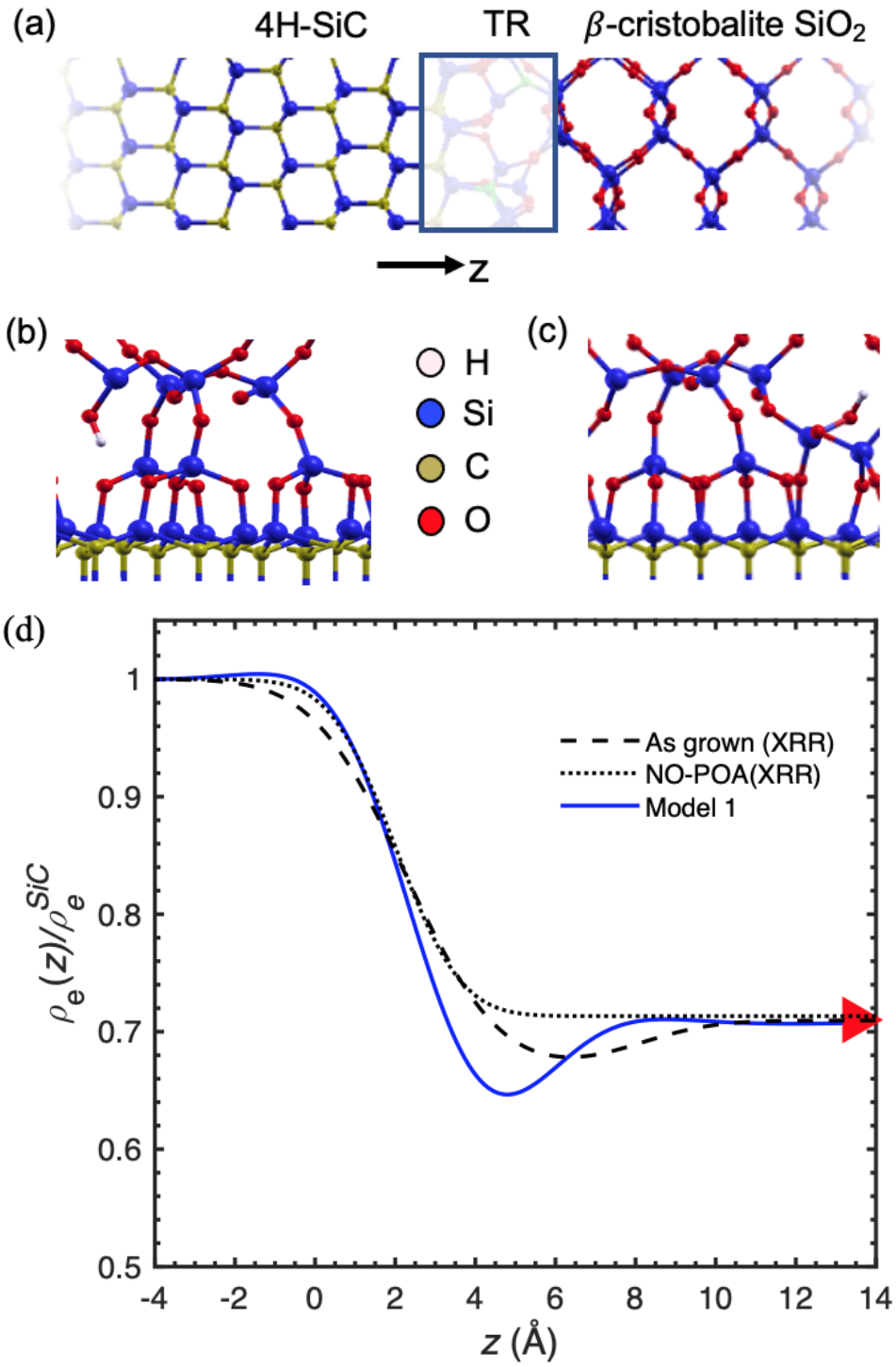

Figure 3.1: (a) Schematic representation of 4H-SiC/SiO_2 interface model, SiC substrate, transition regions (TR), and oxide slab as labeled. Details of TR for the interfaces without N: (b) model 1 and (c) model 2. (d) Electron density profiles $\rho_e(z)$ normalized by ρ_e^{SiC} for interface with no nitrogen that presented the lowest formation energy (model 1 shown in Fig. 3.1(b)). Origin is defined as the location of the C plane adjacent to the interface. For comparison XRR measurements for interface as grown (dashed) is shown in black [10]. The normalized electron density for bulk β-cristobalite SiO_2 is specified with triangle symbol in red at $\sim$0.71.

electron densities (see Section 2.7 for details). For the sake of comparison, the origin of the interface is placed at the C plane adjacent to the interface; alignment with respect to XRR density profiles [10], however, is arbitrary. The electron density, normalized by the SiC bulk density ($\rho_e^{\text{SiC}} \approx 0.95\,\text{e}^-/\text{Å}^3$), reaches the constant bulk value (~ 0.71 for our epitaxy) about 10 Å away from the TR, indicating that size effects in these systems are not influencing our analysis.

The electron density for model 1 shows a minimum value of 0.65 $\text{e}^-/\text{Å}^3$ at ∼4.8 Å from the interface origin ($z = 0$). This density drop below the oxide bulk value is qualitatively similar to the one found in the XRR experiment for as grown SiO_2 on SiC. We found that addition of Si and O atoms near the interface in the metastable model 2 produces a higher electron density (see Appendix C) that removes the unexpected reduction observed in the TR of model 1, resembling that of the NO-annealed interface. However, from our prior analysis of the formation energy of these interfaces, in the absence of nitridation, high Si density is less likely to occur very near the interface.

3.5.2 Nitrogen Passivated SiO_2/SiC Interfaces

We then analyze the cases with nitrided TRs where 3 N atoms yield an areal density of $\sim 4 \times 10^{14}$ cm^{-2} similar to experimental estimates [41, 42, 43]. Among the possible coordination arrangements of the N atoms we adopt the configuration where they are bonded to 3 Si atoms (Si_3-N) over the 2 Si and 1 O (Si_2-N-O), or 1 Si and 2 O (Si-N-O_2) cases. This choice is based on the lowest formation energy results obtained for interface models with different nitrogen coordination environments, as shown in Figs. 3.2(a)-3.2(c). The Si_3-N configuration has also been reported to be dominant through XPS analysis [43]. As a consequence of these arrangements, nitrided cases yield a larger Si density in the TRs than those lacking N, as shown below.

Models 3 and 4 that emulate nitrided interfaces are shown in Figs. 3.2(d)-3.2(e). In model 3, we include 5 Si atoms in the TR to accommodate 3 N atoms. In model 4, a total of 6 Si atoms are added in the TR albeit spread over a wider region than model 3. In both models, the N atoms are bonded to atoms on the Si-face of SiC. A variation of model 3 with the same

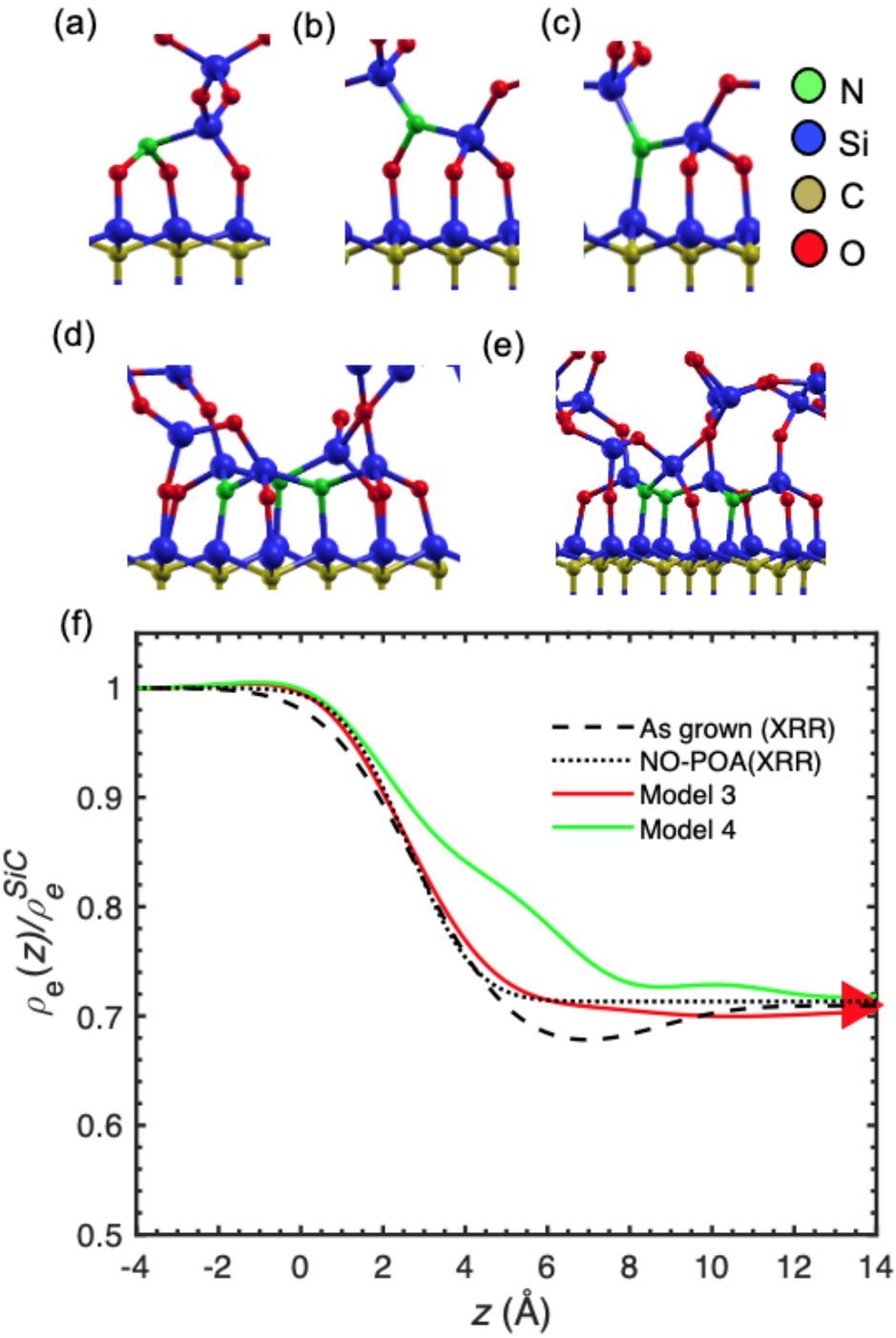

Figure 3.2: Schematic representations of interfaces with N passivation with different geometric arrangements: (a) Si-N-O_2 (b) Si_2-N-O and (c) Si_3-N. We find that the formation energy of the Si_3-N configuration is 2.9 eV and 6.5 eV lower than the Si_2-N-O and Si-N-O_2 cases, respectively. Details of the TRs for the nitrided 4H-SiC/β-cristobalite SiO_2 interfaces: (d) model 3 and (e) model 4. (f) Normalized electron density profiles ($\rho_e(z)/\rho_e^{\mathrm{SiC}}$) for models 3 and 4. For comparison XRR measurements after NO-POA (dotted line) is shown [10].

nitrogen density but differing atomic configuration gives a higher interface formation energy, as discussed in Appendix B. Computations of E_{if} for these nitrided interfaces yield considerably lower values than that of model 1: -4.7 eV (-3.5 eV) for model 3, -5.7 eV (-4.5 eV) for model 4 when considering C-poor (Si-poor) regime. We note here that while the magnitude of the interface formation energy varies depending on the reference chemical potentials (i.e. C-poor or Si-poor conditions), the relative stability for different interface models is consistent between those choices. Therefore, nitridation of the TR stabilizes the interface by allowing for the compensation of the Si density mismatch between 4H-SiC and SiO_2.

When compared to the results of model 1, electron densities for models 3 and 4 increase in the TR, with model 4 exhibiting a larger increase because of its higher atomic density. Features of models 3 and 4 agreeing with XRR measurements for NO-annealed interfaces [10] allude to a high atomic density thermodynamically favored by nitridation prevents the reduction in the electron density below the oxide bulk value. Hence, we speculate that if the N areal density in the TR of an interface model is increased above the experimental estimates, electron densities for the corresponding interface would be even higher those of model 3 and 4. We highlight that previous models, suggesting that N atoms solely substitute for O atoms and heal dangling bonds, would result in a reduced electron density near the interface [10] unless accompanied with an increased atomic density to compensate the Si density deficit in the TR. Owing to the similar trends for other oxide phases, we expect that our observations would likely hold in different silica cases including a-SiO_2, as discussed in Appendix C.

3.6 Projected Density of States Profiles

We next study the electronic structures of the interface models. The in-plane average of the local density of states (DOS) is calculated by projecting wavefunctions onto localized atomic orbitals. The results corresponding to the interface models 1, 3 and 4 are plotted in Fig. 3.3. We observe that the SiC region ($z < 0$) possesses a smaller gap than the oxide ($z > 0$) with no mid-gap states appearing in either, consistent with the fact that these models are dangling bond-free. In the case of model 3 and 4 we superimpose the corresponding projections of the

local DOS onto N atomic orbitals ($0 \lesssim z \lesssim 5$ Å) to find that their interfacial N-states primarily reside below the valence band edge.

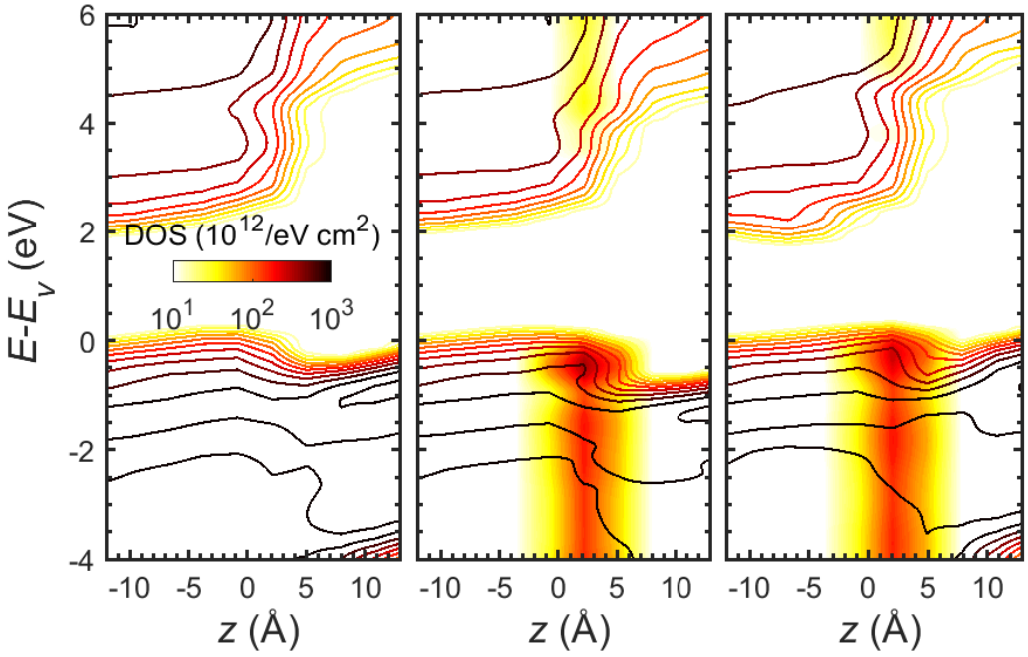

Figure 3.3: In-plane average local DOS profiles (contour lines in log scale) along z direction for (left) model 1, (middle) model 3 and (right) model 4. In model 3 and model 4, the contribution from N states is also included as a surface plot. The position z is referred to the topmost C plane; the valence band maximum is set at 0.

3.7 Band Alignment

Considering thick oxide slabs also allows us to quantify valence (ΔE_V) and conduction (ΔE_C) band offsets by aligning local band edges with respect to the local electrostatic potential [100, 101]. This methodology that combines DFT and the screened hybrid Heyd-Scuseria-Ernzerhof (HSE) functional [102, 93] offers improved descriptions of the band gaps to overcome well-known limitations of DFT [103]. The band gap energies for 4H-SiC ($E_g^{\mathrm{SiC}} = 3.2$ eV) and SiO_2 ($E_g^{\mathrm{SiO_2}} = 8.3$ eV) are determined by choosing the optimum mixing parameter (0.25 for SiC and 0.35 for SiO_2 [100]) in the HSE calculations. The resulting band offsets for our systems show values comparable to previous experimental results [67, 125] but no definite change under nitridation (Table 3.1). Namely, the most stable case (model 4) exhibits a slight increase in ΔE_C, while models 3 presents reduced barrier heights in closer agreement with experiments [67, 125].

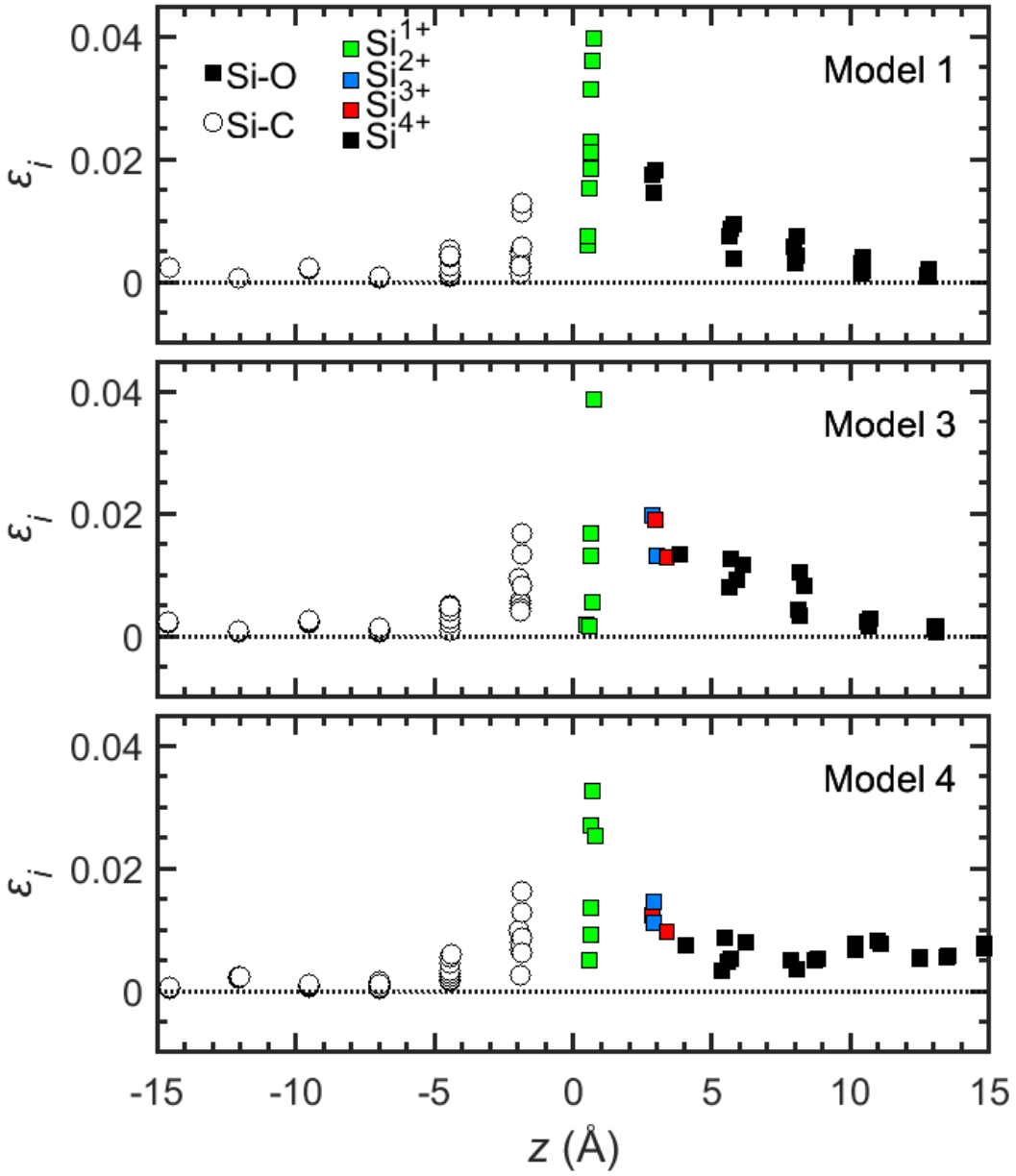

Figure 3.4: Average strain (ε_i) in Si-C and Si-O bonds for different Si atoms as a function of z position of Si atoms for models. Colors discriminate the number of O atoms (n in Si^{n+}) bonded to individual Si atom.

Table 3.1: Properties of different interface models and experiments (no nitridation). Valence (ΔE_V) and conduction (ΔE_C) band-offsets obtained from calculations. Total bond strain square ε^2 in Si-C and Si-O bonds for interface models.

Interface Model	ΔE_V (eV)	ΔE_C (eV)	ε^2 (Si-C)	ε^2 (Si-O)
1	1.8	3.3	0.0013	0.0078
2	2.7	2.5	0.0027	0.0086
3	2.4	2.8	0.0019	0.0056
4	1.7	3.4	0.0017	0.0060
Expt. [67, 125]	2.5-2.9	2.7-2.9	–	–

3.8 Mechanical Strain

To assess the correlation between the composition and geometric structure of interfaces, we analyze strain fluctuations in both the SiC and SiO_2 slabs. For the i-th Si atom we compute the average bond strain as follows:

$$\varepsilon_i = \sqrt{\frac{1}{N_{i,\alpha}} \sum_{\alpha=1}^{N_{i,\alpha}} \left(\frac{\delta r_{i,\alpha}^X}{r_0^X} \right)^2} \tag{3.2}$$

In the above equation, $N_{i,\alpha}$ is the number of X bonds that the i-th Si atom forms and $\delta r_{i,\alpha}^X = r_{i,\alpha}^X - r_0^X$ is the bond length difference with respect to the average bulk value (r_0^X), where X stands for Si-C or Si-O bond ($r_0^{\text{SiC}} = 1.89$ Å and $r_0^{\text{SiO}_2} = 1.64$ Å). Results for the average bond strain ε_i as a function of the z position of the i-th Si atoms are presented in Fig. 3.4. As bond lengths may change based on chemical environment [126], we distinguish Si atoms according to their coordination number with O atoms (Si^{n+}) with different colors. The Si^{1+} atoms (green) correspond to those in the 4H-SiC (0001) surface that produce the O-monolayer [115]; the Si^{2+} and Si^{3+} are only found in nitrided interfaces for our models. Far from the interface all models exhibit minimal strain in the bulk of both SiC and the oxide. In contrast, the strain increases significantly near the interface.

Computation of the total strain square, as elastic energy $u_{el} \propto \sum_i \varepsilon_i^2$, provides a qualitative insight on the role of nitrogen in the 4H-SiC/SiO_2 interface. We calculate the quantity $\varepsilon^2 = \sum_i \varepsilon_i^2$ for Si-C and Si-O bonds independently for each interface model (Table 3.1). Comparison of the results shows that strain in Si-O bonds for model 1 is larger than that of nitrided interface

models. We note, however, that strain values of model 1 are sensibly lower than those of model 2 suggesting that in the absence of nitrogen, a higher atomic density near the interface increases the elastic energy. Therefore, the introduction of nitrogen not only increases the atomic density near the interface smoothing the density mismatch between SiC and silica but also appears to reduce the local strain in Si-O bonds.

Chapter 4

High-κ Dielectric Candidates

4.1 Summary

We have successfully described the 4H-SiC (0001)/SiO_2 interfaces in Chapter 3. For this chapter, high throughput screening of alternative dielectrics to replace SiO_2 for 4H-SiC based devices is described. We are the first to conduct a systematic study of alkaline earth metal dihalides (AX_2) as the gate dielectrics for 4H-SiC by analyzing their structural and electronic properties using first principles calculations within the density functional theory (DFT). Through analysis of their formation energies, we identify the most stable AX_2 crystal structures. According to those stable structures, the band gaps are evaluated using generalized gradient approximation (GGA) or Heyd–Scuseria–Ernzerhof (HSE) functional. As a result, HSE calculations produce more consistent band gaps with experiments in contrast to the band gaps underestimated by GGA calculations. Furthermore, the dielectric constants are computed within density functional perturbation theory using three different approximations regarding the exchange-correlation functional. We find that the dielectric constants calculated from GGA including dispersion forces highly agree with those calculated from local density approximation (LDA). Based on our results, the most promising candidate high-κ dielectrics are determined to be AF_2. Moreover, we examine the properties of other possible high-κ dielectrics such as Al_2O_3 and LiF in a similar process legitimating their potentials as candidate high-κ materials for 4H-SiC.

4.2 Background

For SiC MOS devices, the native oxide SiO_2 represents the most widely used dielectric due to the high compatibility of SiC with mature Si processing [32, 33, 34, 35]. The density of several miscellaneous defects in the thermal SiO_2 and at SiC/SiO_2 interfaces is several orders of magnitude higher than in Si/SiO_2 interface, which hampered the favourable properties of SiC for power electronics applications [113, 127]. Although C related defects such as C-dangling bonds, C-interstitials, and C-dimers are believed to be dominant[38, 39, 40, 41, 42, 43, 44, 45, 46, 47], a qualitative measurement of the defects introduced into the SiC/SiO_2 interface and oxide during the oxidation of SiC is still missing. In addition, many passivation methods or post oxidation annealing have been proceeded to reduce the interface defect density [53, 54, 55, 56, 57, 58, 59, 60, 61, 62, 63, 64, 65, 38, 66, 67, 68, 69, 70]. However, after surface treatments, 4H-SiC/SiO_2 MOSFETs still exhibit much lower channel mobility in contrast to bulk 4H-SiC. Furthermore, as the transistors and capacitors in electronics are continued to be scaled down to less than a few nanometers, SiO_2 can not fulfill this mission without compromising the gate capacitance. If SiO_2 is used, the leakage currents through the thin film pose a serious problem to the device's reliability.

One approach to solve these problems involves the use of alternative dielectric to replace SiO_2 as the gate dielectric for 4H-SiC. The ideal dielectric exhibiting a larger dielectric constant and wider band gap than SiO_2 can enhance the capacitance and block leakage simultaneously. The experimental band gap and dielectric constant of various alternative gate dielectrics that likely are applied to Si are shown Fig. 4.1, adapted from [11]. We observe a roughly inverse relation between band gap and dielectric constant of these materials. For wide band gap semiconductor electronics, however, the dielectrics with larger band gap and dielectric constant than SiO_2 are scarce. In addition, the dielectric is expected to have large band offsets with 4H-SiC to minimize leakage in the off state. For those potential candidates for 4H-SiC gate dielectrics such as aluminum oxide (Al_2O_3), aluminum nitride (AlN), hafnium oxide (HfO_2), lanthanum oxide (La_2O_3), zirconium oxide (ZrO_2), tantalum pentoxide (Ta_2O_5), and titanium

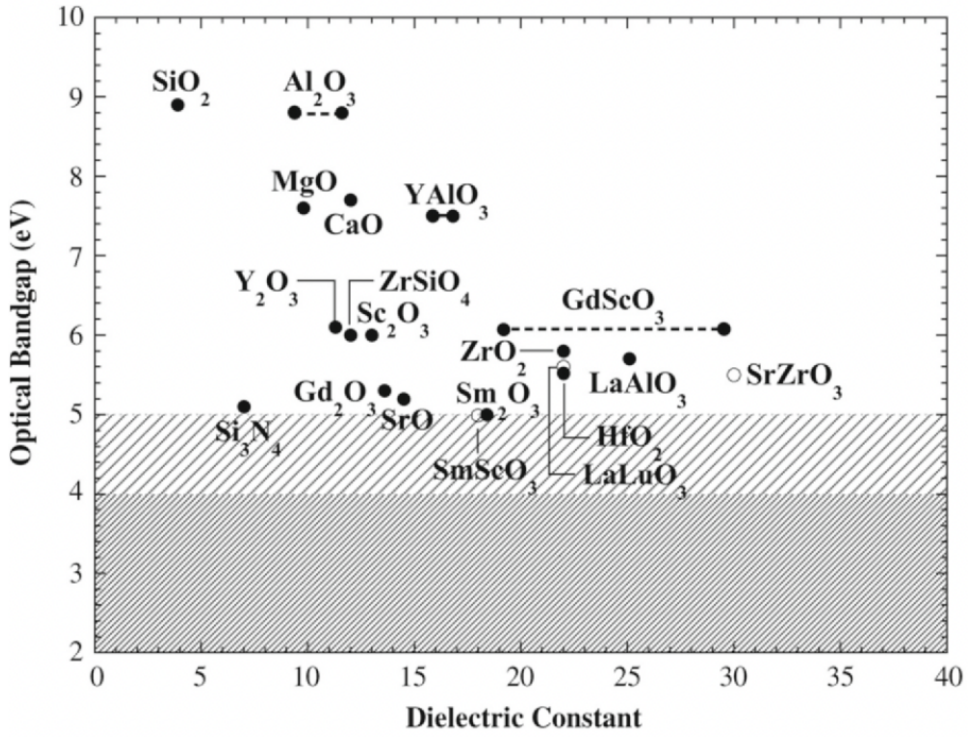

Figure 4.1: Experimental band gap versus dielectric constant of alternative dielectric materials, adapted from [11].

dioxide (TiO_2), and their combinations with each other, and with SiO_2, their dielectric constants, breakdown electric field, band gap, and band offsets with respect to 4H-SiC are demonstrated in Fig. 4.2 from [12]. It is clear that not only the band gaps of these newly explored dielectrics are not comparable with that of SiO_2 but also the band offsets with respect to 4H-SiC are not much favorable.

In light of the advantages of high-κ dielectrics and the associated challenges, here we focus on searching for alternative dielectrics among alkaline earth metal dihalides in this chapter. Previous research showed the significant potential of CaF_2 as a gate dielectric in 2D materials-based FETs [128, 129, 130, 131], as well as an insulation layer in metal–semiconductor–metal structures [132]. Also, the CaF_2/Si (111) interface has been experimentally [133] and theoretically [134, 135] characterized in great detail. Although research has illuminated the wonder of this class of dielectrics, yet their properties are not fully understood. For instance, available experimental band gaps and dielectric constants for some of the interested materials have

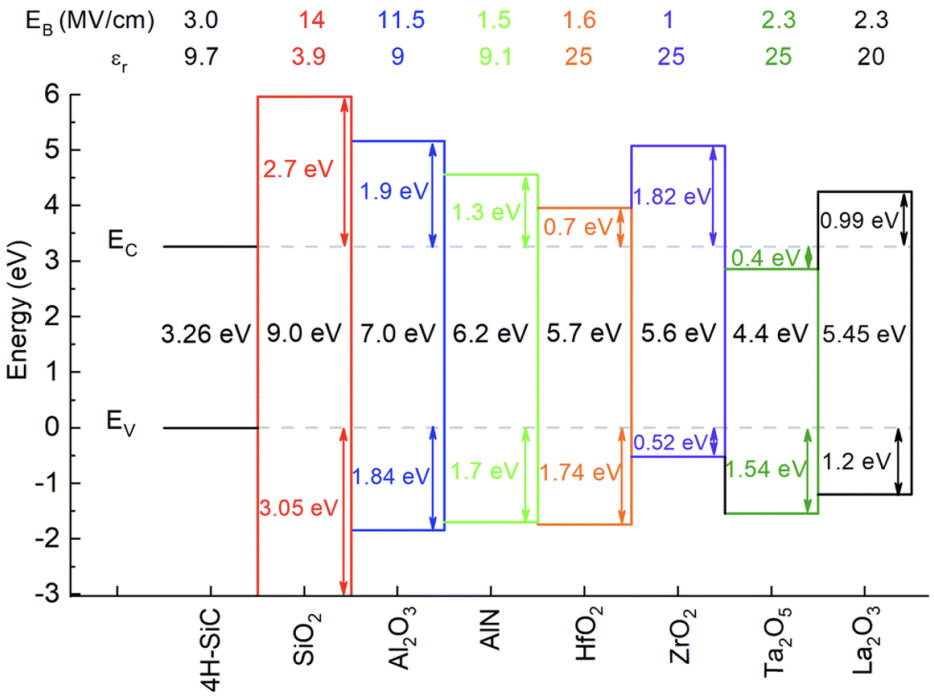

Figure 4.2: Properties of various high-κ dielectrics including their breakdown field, dielectric constant, band offsets and band gap in comparison to 4H-SiC, adapted from [12].

shown certain uncertainties [15, 16, 17, 18, 19]. Therefore, we are intended to conduct a systematic study of this class of materials within DFT, and answer the question that which one of the candidate materials could be suitable in a theoretical basis.

4.3 High Throughput Screening

We conduct a comprehensive study of alkaline earth metal dihalides (AX_2) formed by alkaline earth metal (A = Mg, Ca, Sr and Ba) and halogen (X = F, Cl, Br and I), including the phase analysis, calculations of band gap, electronic properties, and dielectric constant. Following that, similar analysis is applied to other dielectrics, such as Al_2O_3 and LiF. Implementation of this process is demonstrated in Fig. 4.3. Hundreds of initial AX_2 crystal structures are found from AFLOW data base [136]. Thus our search is not only limited to the most stable or experimentally observed phases but also includes all the theoretically stable structures. It turns out that 65 distinct outputs are selected after excluding equivalent structures.

To obtain the most stable AX_2 phases, the atomic positions and lattice parameters of the supercell cells are fully optimized while the convergence threshold on total energy (forces) for

ionic minimization is set to value of 1.0×10^{-8} Ry (2.5 meV/Å). The core-valence interactions are described through normconserving pseudopotentials generated at the PBE level. The wave functions are expanded in a plane-wave basis set using an energy cutoff of at least 80 Ry (90 Ry for MgX_2). The Brillouin zone (BZ) is sampled using a sufficient Monkhorst-Pack k-point mesh [120]. The size of k-point mesh is chosen to be inversely proportional to lattice constants. Based upon the equilibrium configurations, their band gap and dielectric constant are computed to reproduce the property map of band gap versus dielectric constant.

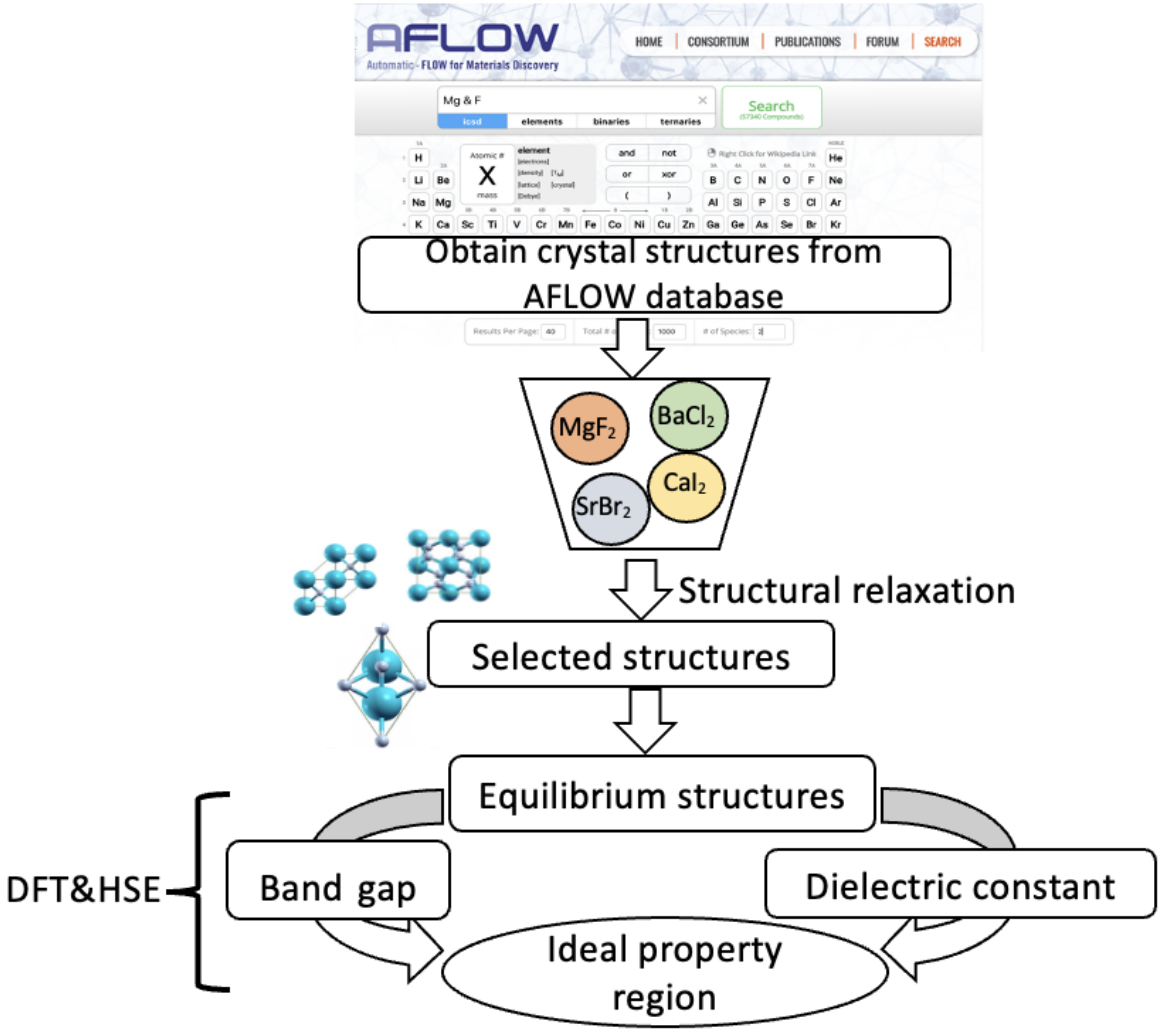

Figure 4.3: Workflow for the implementation of high throughput screening candidate high-κ dielectrics.

4.4 Formation Energy

The number of formulas (AX_2) varies with the number of atoms in the primitive unit cell for crystal structure. In order to compare the stability of different crystal structures, the crystal formation energy E_{uc} is defined as:

$$E_{\text{uc}} = \frac{E_{DFT}}{N_{AX_2}} \tag{4.1}$$

where the E_{DFT} is the DFT ground state energy and N_{AX_2} is the number of formulas in the unit cell. For instance, there are six distinct crystal structures of MgF_2 available from AFLOW database, with different primitive unit cells as illustrated in Fig. 4.4. They correspond to simple Cubic (CUB), Face-Centered Cubic (FCC), Hexagonal (HEX), Base-Centered Orthorhombic (BCO), Tetragonal (TET) and Triclinic (TRI) cells (from left to right). Their optimized lattice constants, formation energies and space group are summarized in Table 4.1. The most stable phase is determined to be the TET phase with the smallest value of E_{uc}. The band gap and dielectric constant of MgF_2 are subsequently determined for the TET crystal structure.

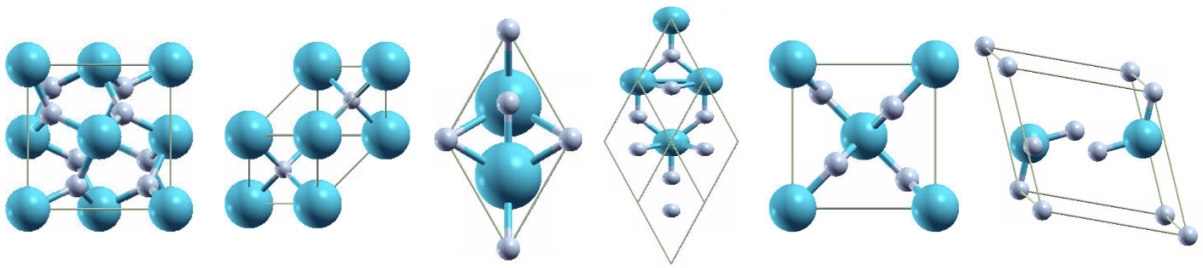

Figure 4.4: Primitive unit cells of MgF_2 phases found from AFLOW (from left to right): simple Cubic (CUB), Face-Centered Cubic (FCC), Hexagonal (HEX), Base-Centered Orthorhombic (BCO), Tetragonal (TET) and Triclinic (TRI) cells.

Table 4.1: PBE lattice constants, formation energy (E_{uc}) and space group (SG) of MgF_2 phases from AFLOW database.

	CUB	FCC	HEX	BCO	TET	TRI
a (Å)	5.01	4.99	3.38	2.83	4.69	5.87
b (Å)	5.01	4.99	3.38	6.99	4.69	5.85
c (Å)	5.01	4.99	6.50	3.23	3.09	3.91
E_{uc} (Ry)	-204.630	-204.610	-204.556	-204.587	-204.645	-204.623
SG no.	205	225	194	38	136	12
SG symbol	Pa	Fmm	$P6_3/mmc$	Amm2	$P4_2mnm$	C2/m

We show the results of the formation energy for all distinct AX_2 crystal structures available from AFLOW as seen in Fig. 4.5. The formation energy results are categorized in the panels (from left to right) corresponding to $A\mathrm{F}_2$, $A\mathrm{Cl}_2$, $A\mathrm{Br}_2$ and $A\mathrm{I}_2$, respectively. In each panel, different symbol represents distinct crystal structure. The most stable phase with the smallest value of E_{uc} is set at 0. Hence, ΔE_{uc} refers to the formation energy difference value with respect to the the most stable phase. We find that among different crystal structures, the calculated energies differ from one another up to 1.5 eV. The most stable phases are rocksalt (FCC), Hexagonal (HEX) and Tetragonal (TET).

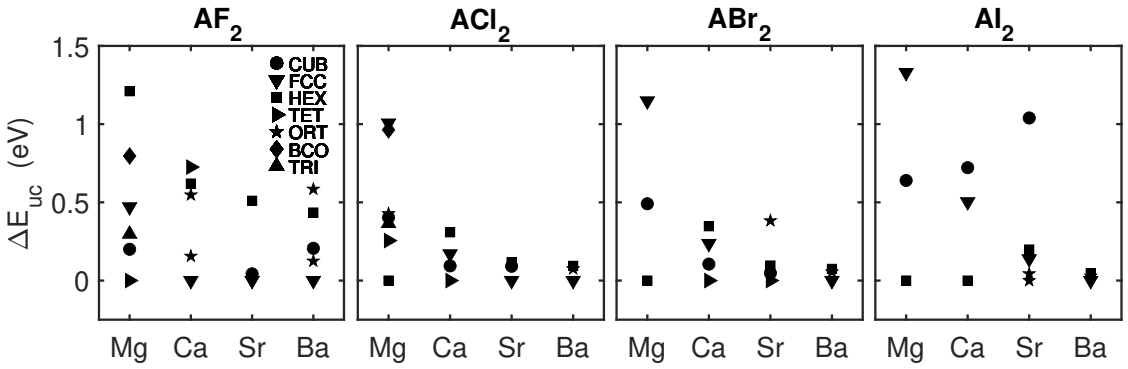

Figure 4.5: Formation energy difference (ΔE_{uc}) versus alkaline earth metals (A = Mg, Ca, Sr and Ba), for $A\mathrm{F}_2$, $A\mathrm{Cl}_2$, $A\mathrm{Br}_2$ and $A\mathrm{I}_2$ (from left to right). Symbols for different crystal structures: simple Cubic (CUB), Face-Centered Cubic (FCC), Hexagonal (HEX), Tetragonal (TET), Base-Centered Orthorhombic (BCO), Primitive Orthorhombic (ORT) and Triclinic (TRI) cells.

4.5 DFT Band Gap

The calculated DFT band gap is plotted for the same AX_2 crystal structures in Fig. 4.6. In order to have a closer look at the relation between the band gap and the formation energy, each symbol is color coded according to the formation energy of the crystal structure. As observed for each type of dihalides from left to right panel, the crystals as shown in blueish color representing more stable phases have larger band gap energies. Furthermore, $A\mathrm{F}_2$ approximately have the highest and $A\mathrm{I}_2$ have the lowest band gaps. While comparing our calculations with the experiments [15, 17, 18], it is expected that the DFT underestimates the band gap for a bulk solid as it commonly fails to perfectly describe the exchange-correlation functional.

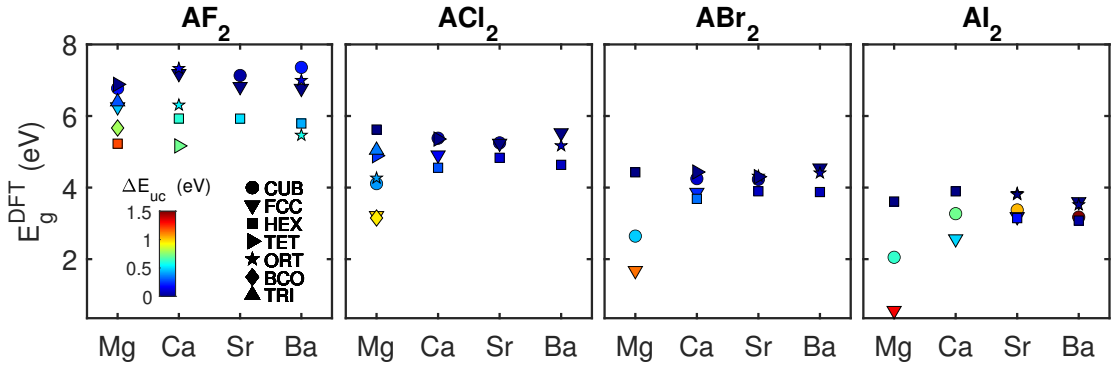

Figure 4.6: DFT band gap (E_g^{DFT}) versus alkaline earth metals (A = Mg, Ca, Sr and Ba), for AF_2, ACl_2, ABr_2 and AI_2 (from left to right). Symbols for different crystal structures: simple Cubic (CUB), Face-Centered Cubic (FCC), Hexagonal (HEX), Tetragonal (TET), Base-Centered Orthorhombic (BCO), Primitive Orthorhombic (ORT) and Triclinic (TRI) cells. Colors refer to the magnitude of the formation energy.

In order to improve the results from DFT, we compute band gap energy within the DFT by including the Heyd–Scuseria–Ernzerhof (HSE) exchange-correlation functional [102, 93] which yields comparable band gap values to the experiments, suggesting more validity of our results. In terms of the band structures, HSE functional effectively capture all the bands at consistent energy levels as the GGA functional, except the former gives an increase of $\sim$20% in the band gap, as seen in Fig. 4.7. Though HSE calculations can improve band gap to some extent, the GGA calculations are normally $100-10000$ times less computationally expensive. Here we are dealing with several-atom systems in affordable computational efforts. Therefore, it is no harm to conduct both calculations providing us meaningful insights on obtaining consistent results.

4.6 Dielectric Constant

The dielectric constant is a key piece of information that must be taken into account when designing the thin film for SiC MOSFETs where the dielectric material functions as the dielectric in a capacitor. Under such circumstance, the dielectric constant should be high so that not only the breakdown electric field across the dielectric can be reduced but also the gate leakage currents can be effectively reduced. Hence, the dielectric materials under the search with higher dielectric constant than SiO_2 are preferred. Although some remarkable experimental

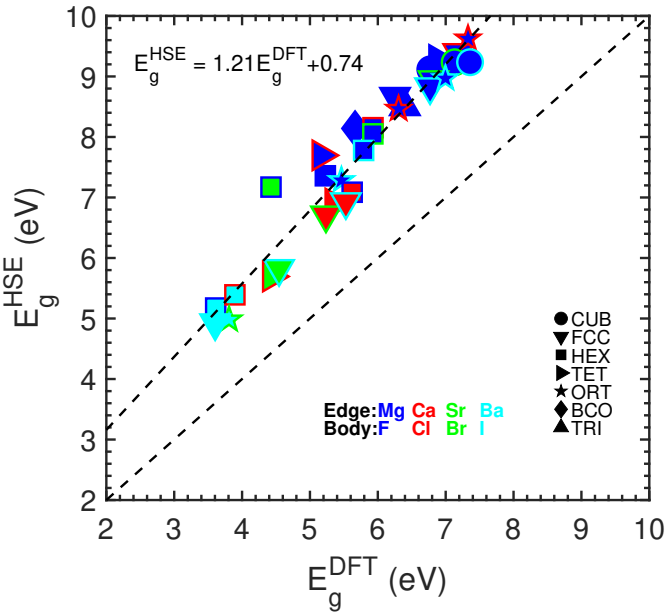

Figure 4.7: HSE band gap (E_g^{HSE}) versus DFT band gap (E_g^{DFT}). Symbols in the figure correspond for different crystal structures. The face of symbols is color coded based on the halides and the edge is color coded according to the alkaline earth metals. The trend line for data is shown in dash line, as well as the equal line ($E_g^{HSE} = E_g^{DFT}$). The fitting equation to data demonstrates that HSE calculation achieves 20% improvement of band gap energy, which is underestimated by DFT calculation.

measurements of the dielectric constant of AX_2 have been produced, it requires systematically computational estimations with high accuracy for all AX_2.

Here, the dielectric constant is computed by employing external perturbation within the density functional framework, which includes the electronic response (first term in Eq. 4.2) and the ionic response (second term in Eq. 4.2) that can be written as [137]:

$$\varepsilon_{\alpha\beta} = \varepsilon^{\infty}_{\alpha\beta} + \frac{4\pi}{\Omega_o}\sum_m \frac{S_{m,\alpha\beta}}{\omega_m^2} \tag{4.2}$$

where the mode oscillator strength is defined through

$$S_{m,\alpha\beta} = (\sum_{\kappa\alpha'} Z^*_{\kappa,\alpha\alpha'} U^*_{mq=0}(\kappa\alpha'))(\sum_{\kappa'\beta'} Z^*_{\kappa',\beta\beta'} U_{mq=0}(\kappa'\beta')) \tag{4.3}$$

In above equations, the electronic dielectric permittivity tensor $\varepsilon^{\infty}_{\alpha\beta}$ in direction α and β is obtained directly from DFT calculations, as well as the unit cell volume Ω_o, the phonon

frequency ω_m for mode m, and the Born effective charge tensor $Z^*_{\kappa,\alpha\alpha'}$ for atom κ. In order to compute $S_{m,\alpha\beta}$, the phonon eigendisplacements $U_{mq=0}$ at zone-center (q=0) is found by diagonalizing the dynamical matrix that is also available from DFT calculations.

Regarding the exchange-correlation functional between electrons, three different approximations are used: local density approximation (LDA) [138], generalized gradient approximation (GGA) [139], and GGA functional including dispersion forces (vdW-DF-C09) [105, 106, 107, 108]. The LDA commonly overestimates cohesive energies and underestimate cell parameters, whereas the GGA softens interatomic bonds to overestimate cell parameters [91, 92]. Thus, the GGA is known to be good for estimating the band gap and LDA is better for phonon calculation. Comparing the calculated dielectric constant from different functional, as shown in Fig. 4.8, the GGA results exhibit a larger error than those of LDA. This is because the ionic response of dielectric is sensitive to the low frequency phonon modes which has been significantly softened in GGA [140]. Having said that, the dispersion forces are accounted for consistent results with LDA.

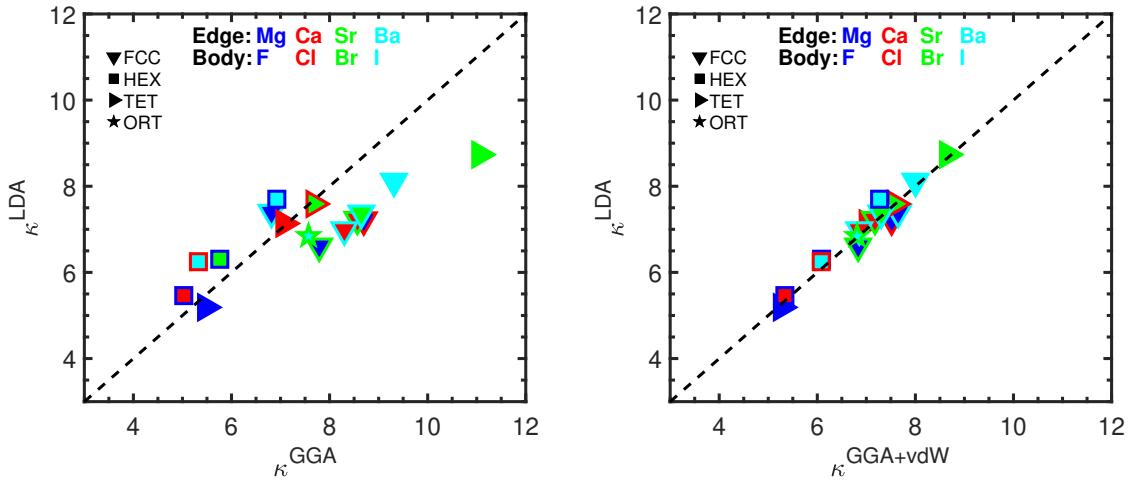

Figure 4.8: Comparison of static dielectric constant (κ) of the most stable AX_2 obtained using different exchange-correlation functional: (left) Local density approximation versus generalized gradient approximation; and (right) Local density approximation versus generalized gradient approximation including van der Waals forces. Symbols in the figure correspond for different crystal structures. The face of symbols is color coded based on the halides and the edge is color coded according to the alkaline earth metals. The equal line ($\kappa^{LDA} = \kappa^{GGA} = \kappa^{GGA+vdW}$) is shown in dash line.

4.7 Candidate High-κ Dielectrics

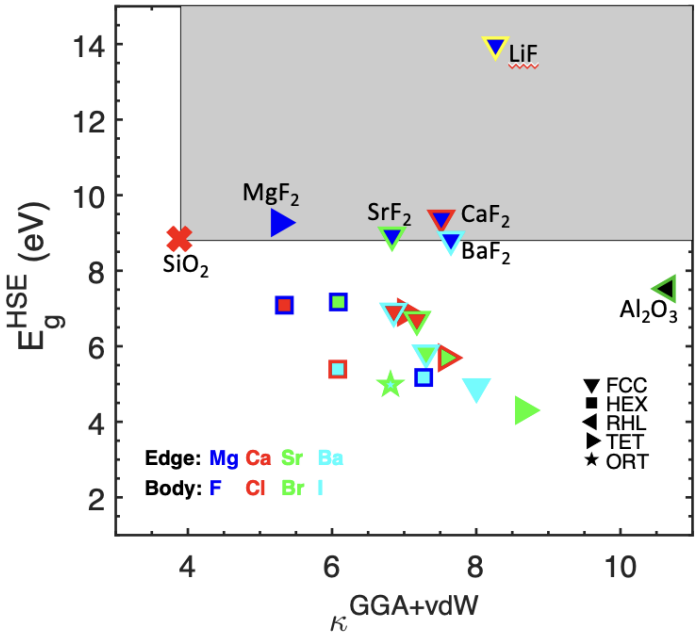

Figure 4.9: Band gap energies as a function of dielectric constants. Symbols in the figure correspond for different crystal structures. The face of symbols is color coded based on the halides and the edge is color coded according to the alkaline earth metals. Shaded area denotes the property region where candidate high-κ dielectrics may offer competitive advantage over SiO_2 for SiC based devices.

In addition to the investigations of a class of AX_2 dielectrics, we perform similar analysis to other dielectric materials that may be suitable for replacing SiO_2, such as LiF and Al_2O_3. The most stable phases are found to be LiF in FCC phase and Al_2O_3 in rhombohedral Bravais lattice. In terms of the band gaps calculated within HSE functional and the dielectric constants calculated within GGA+vdW functional, we present the property map of the band gap as a function of the dielectric constant for the most stable crystal structures. In accordance with trends observed in previous work [140], the band gap decreases as the dielectric constant increases. The dielectric constant increases as the alkaline earth metal or the halogen element of the compounds become heavier. The grey area is labeled as the property region that might be ideal for candidate dielectrics with wider band gap and higher dielectric constant than SiO_2. Our calculations demonstrate that LiF is suitable for 4H-SiC. Within the class of AX_2 materials, the band

gap appears to vary as the halide changes. Moreover, all fluorides exhibit comparable or larger band gap values than SiO_2, which also offer alternative options of dielectrics for 4H-SiC.

Table 4.2: The band gap and dielectric constant of the most stable fluorides. AF_x^{exp} denote the experimental values of fluorides. [15, 16, 17, 18, 19])

Compound	E_g^{HSE}	E_g^{exp}	κ^{DFT}	κ^{exp}
MgF_2	9.3	12.4[15]	5.3	4.9, 5.9[16]
CaF_2	9.4	12.0[17]	7.5	6.8-7.4[15]
SrF_2	8.9	11.1[17]	6.8	6.5-7.7 [15]
BaF_2	8.8	10.5 [17]	7.6	7.32 [15]
LiF	13.4	13.6[18]	8.3	8.3 [19]

It must be pointed out that the band gap values obtained from calculations, however, appear to be lower than those reported in the literature as shown in Table 4.2. The dielectric constant values of fluorides agree well with those measured experimentally. As mentioned earlier, on the one hand, alternative high-κ dielectric materials lead to thicker dielectric film at the same capacitance thereby reducing the leakage currents and their large band gaps also help suppress the charge injection from electrodes into dielectrics that cause the leakage current. On the other hand, the quality of the interface between the dielectric and 4H-SiC plays an important role in improvement of the channel mobility. Hence in next chapter we will focus on discussion of the interfaces formed with 4H-SiC and different flourides (LiF, MgF_2, and CaF_2), as well as Al_2O_3.

Chapter 5

High-κ dielectrics/4H-SiC Interfaces

5.1 Summary

In this chapter we describe the interfaces formed using 4H-SiC and candidate high-κ dielectrics (Al_2O_3, LiF, MgF_2 and CaF_2) identified from the studies described in Chapter 4 using first principles calculations within the density functional theory (DFT). Our results confirm that different surface treatments are essential to optimize the interfacial structures. Analysis of the local density of states (DOS) profiles of 4H-SiC/high-κ dielectric interfaces reveals the effect of 4H-SiC surface treatments on the reduction of interface defect states.

The main results found from this chapter are: 1) Both H and N passivated Al_2O_3/4H-SiC interfaces effectively remove the mid-gap states that are attributed to C dangling bonds residing topmost SiC layer, which validates the recent experimental findings that H_2 annealing or interfacial nitridation combined with H_2 annealing at high temperature prior to atomic layer deposition (ALD) leads to low interface trap density resulting in improved channel mobility and stability for the Al_2O_3/4H-SiC MOSFETs; 2) O terminated 4H-SiC (0001) surface is advantageous to LiF/4H-SiC and AF_x/4H-SiC (A = Ca or Mg) interfaces in reducing mid-gap states; 3) The presence of interface dipoles can significantly impact the band alignments between MgF_2 and 4H-SiC, though incorporation of F atoms can help to resolve the polar instability by modifying the charge distribution near the interface to some extent. Lastly, the band offsets for those 4H-SiC/high-κ dielectric interfaces are computed to compare with available experimental values.

5.2 Background

Among the candidate high-κ dielectrics for 4H-SiC, ALD of Al_2O_3 has shown promising results in experiments reported with excellent channel mobility and low interface trap density. The 4H-SiC (0001) before the deposition of Al_2O_3 films is prepared under various surface treatments aiming for passivating interfacial defects of high density. The surface treatments that have been applied in Al_2O_3/4H-SiC interfaces are sacrificial oxidation in O_2 [141, 142], nitradation [53, 54, 55, 56, 57, 58, 59, 60, 61, 62, 63, 64, 65, 38, 66, 67, 68], H_2 annealing [143, 144, 145], and growing a 0.7 nm thick interfacial SiO_2 layer via thermal oxidation of 4H-SiC [146, 147, 148]. They have been proven to modify 4H-SiC (0001) prior to ALD chemically and energetically with the aid of different techniques. Aside from experimental measurements using XPS [149, 43, 42], low energy electron diffraction (LEED) analysis [115], low-temperature electrically detected magnetic resonance (EDMR) spectroscopy and other related techniques [46], considerable theoretical efforts have also been made to help identify the chemical mechanisms of those surface treatments [115].

Regarding the discussions above, in the case of nitradation, it may form a Si-N-O bonded SiON layer [115, 43, 42] between the substrate and Al_2O_3 films; As observed in 6H-SiC, H_2 annealed 4H-SiC prior to the ALD Al_2O_3 generates a H-terminated surface in the form of Si-H bonds on top SiC layer but easily convert into Si-OH bonds to favor the ALD process [150, 151, 152, 153, 154], which results in a monolayer of O atoms bridging the substrate and Al_2O_3. It is worth mentioning that an exact 0.7 nm SiO_2 layer between Al_2O_3 and 4H-SiC has been proven to produce the lowest interface trap density and highest channel mobility. However, formation of this SiO_2 layer is not as practical as other surface treatments considering that many factors associated with the implementation of experiments are easily varied. These existing theoretical studies of the interfacial structure between Al_2O_3 and 4H-SiC accounting for the surface treatments are encouraging, however, systematic studies examining the full Al_2O_3/4H-SiC interface composition and the structural dependence of electrical properties in the interface are still missing. Hence, we determine the most stable phase of Al_2O_3 from Chapter 4, followed by the band gap energy and dielectric constant. In this chapter we create realistic

Al_2O_3/4H-SiC interface structures relating to the surface treatments, more specifically, we look into the Al_2O_3/4H-SiC interfaces including H and N passivation because it has been found that sacrificial oxidation of 4H-SiC prior to ALD Al_2O_3 in O_2(or NO) followed by H_2 annealing produce lower interface defect density [155] suggesting that H or N atoms are probably incorporated near the interface to passivate the defects.

Apart from the Al_2O_3/4H-SiC interface, we explore the interfaces between 4H-SiC and candidate high-κ dielectrics identified from Chapter 4, for instance, LiF, MgF_2 and CaF_2, in a similar approach that has been applied to SiO_2/4H-SiC interfaces. Sharopov et al. demonstrated that epitaxial LiF film can be grown on the Si (111) using electron irradiation and negative potential treatment during film growth [156]. As far as we know, no previous research has investigated the interfaces between 4H-SiC and these fluorides experimentally or theoretically. This work on study of AF_x/4H-SiC interfaces could prove quite beneficial to more future researches. Our approach to characterize these interfaces involves the use of surface treatments discussed previously that work well for Si or SiC based MOS interface for high channel conductivity. It is important to highlight the fact that oxidation of 4H-SiC, H or N involved surface treatments could be used for LiF, MgF_2 and CaF_2 as well, and in return, similar interfacial schemes can be applied for these candidate high-κ dielectrics if deposited on 4H-SiC (0001).

5.3 Computational details

In addition to the computational details described in Section 2.9, the equilibrium configurations are obtained by allowing all atoms to fully relax, while the convergence threshold on total energy (forces) for ionic minimization is set to value of 1.0×10^{-4} Ry (10 meV/Å). The atomic cores are characterized via projector augmented wave (PAW) pseudopotentials [109] with different energy cutoffs regarding the Kohn-Sham wave functions and densities, respectively. The Brillouin zone (BZ) is sampled using a Monkhorst-Pack mesh [120] (see Table 5.1), where BZ integration is performed using Methfessel-Paxton first-order spreading. DFT calculations are applied to the epitaxy for each 4H-SiC/high-κ dielectric interface, which is selected based on minimizing the strain due to lattice mismatches between 4H-SiC and high-κ dielectrics (see Section 2.6 for details). The in-plane lattice constants of the supercells are set to be those of

SiC, yielding a lateral strain applied to high-κ dielectric layers. More details description of the interfaces will be discussed in following sections.

Table 5.1: Number of atoms (nat) in 4H-SiC/high-κ dielectric epitaxies, cutoff energies regarding the Kohn-Sham wave functions (ecutwfc (Ry)) and densities (ecutrho (Ry)), and Monkhorst-Pack mesh (nk1 nk2 nk3) for sampling the BZ.

Interface	nat	ecutwfc/ecutrho	nk1 $\times$ nk2 $\times$ nk3
Al_2O_3/4H-SiC	$\sim$250	50/400	$3\times3\times1$
LiF/4H-SiC	$\sim$370	50/400	Γ
MgF_2/4H-SiC	$\sim$250	60/400	$2\times2\times1$
CaF_2/4H-SiC	$\sim$340	60/400	$2\times2\times1$

Table 5.2: Parameters matrix [n_1^1 n_2^1 n_3^1;n_1^2 n_2^2 n_3^2;n_1^3 n_2^3 n_3^3] that defines primitive lattice vectors (PLVs) $\mathbf{a}'_x$ (x=1,2,3) of 4H-SiC (high-κ dielectrics) slabs in 4H-SiC/high-κ dielectric epitaxies using bulk 4H-SiC (high-κ dielectrics) PLVs $\mathbf{a}_x$ (x=1,2,3), according to the relation a'_x = $n_1^x a_1$+$n_2^x a_2$+$n_3^x a_3$ (see Section 2.6 for more details), PBE lattice constants a (b) and lateral strain.

Interface	4H-SiC PLVs	high-κ PLVs	a,b (Å)	strain
Al_2O_3/4H-SiC	[2 -1 0; 1 3 0; 0 0 -2]	[-1 2 -1; 2 -1 -1; 2 2 2]	8.18,8.18	1.8%
LiF/4H-SiC	[2 0 0; 4 5 0; 0 0 -3]	[1 -2 -1; 5 1 -5; 4 -4 4]	6.19,14.18,	4.2%
MgF_2/4H-SiC	[3 0 0; 3 3 0; 0 0 -1.5]	[1 -1 -2; 0 -2 0; 3.5 0 3.5]	9.28,9.28	2.2%
CaF_2/4H-SiC	[4 1 0; 3 4 0; 0 0 -1.5]	[0 -3 0; 0 -3 3; 6 -2 -2]	11.15,11.15	4.8%

5.4 Al_2O_3/4H-SiC Interfaces

The epitaxy of Al_2O_3/4H-SiC interfaces adopts the hexagonal unit cell for the rhombohedral Bravais lattice of Al_2O_3 to accommodate 7 SiC unit cells of cross section. The in-plane lattice constants are set to be that of SiC slab ($a = b = 8.18$ Å), yielding a $\sim$1.8% lateral tensile strain applied to Al_2O_3 layers (see Table 5.2). The near-interface regions of Al_2O_3/4H-SiC interface models with different surface treatments are demonstrated in Fig. 5.1 (a-c). The monolayer O atoms attaching to SiC (0001) joint 6 layers SiC and $\sim$20 Å thick oxide slabs. The primary system as shown in Fig. 5.1 (a) has no H passivation near the interface, in contrast to the interface in which 2 H atoms are inserted via formation of O-H bond to remove the dangling bonds from oxide in Fig. 5.1 (b). The interface with both N and H passivation in Fig. 5.1 (c) is derived from H-passivated interface by replacing one of monolayer O atoms with N atom. The C and O atoms at the end are H-passivated to diminish the edge states corresponding to the dangling bonds.

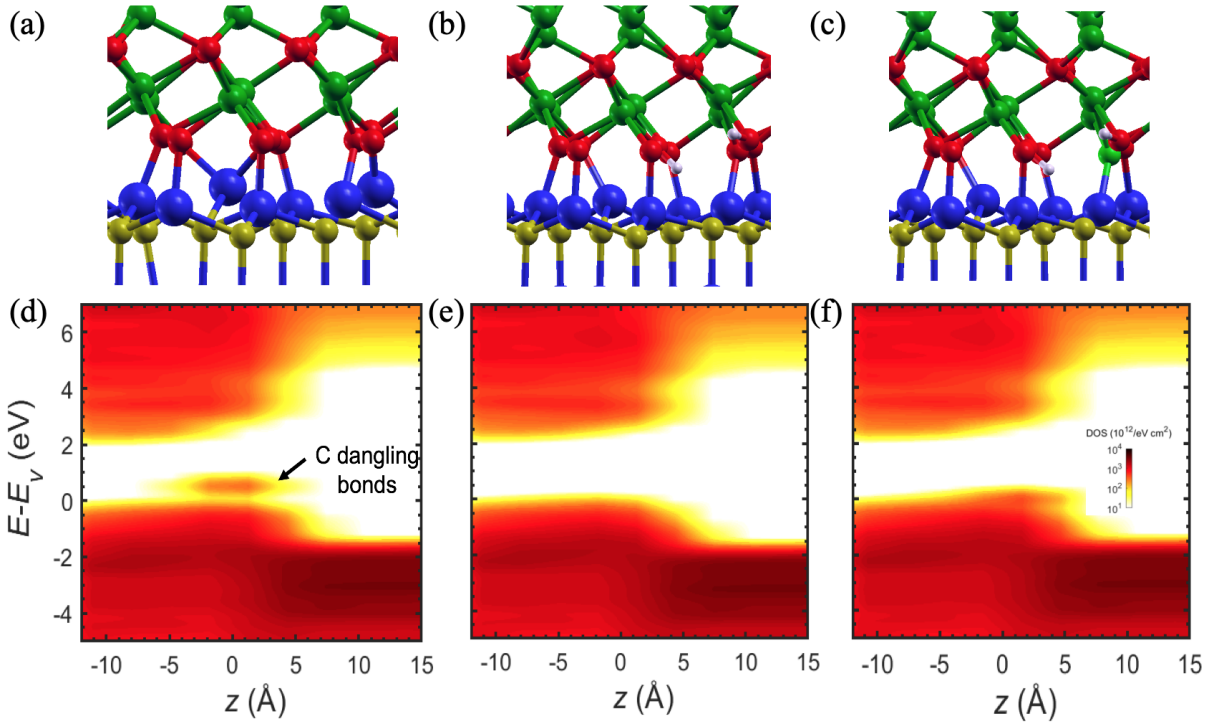

Figure 5.1: Schematics of Al_2O_3/SiC interfaces (a) without H passivation (b) with H passivation (c) with both N and H passivation; and in-plane average local DOS profiles (in log scale) along z direction for Al_2O_3/SiC interfaces (d) without H passivation (e) with H passivation and (f) with both N and H passivation. The position z is referred to the topmost C plane; the valence band maximum is set at 0.

In order to investigate the role of H and N atoms at the interface, we present the results of in-plane average of the local DOS for Al_2O_3/4H-SiC interfaces without H passivation, with H passivation, and with both N and H passivation, as illustrated in Fig. 5.1(d-f), respectively. The comparisons revealed that band gaps are negligibly affected after introduction of extrinsic atoms (H or N), though DFT underestimates the band gaps of all three systems. The result for interface prior to H or N addition demonstrates a few localized states above valence band maximum (VBM) (at energy levels between 0 to 1 eV) that are attributable to C dangling bonds existing in top SiC layer. In contrast, those mid-gap states can be removed, provided H or N atoms are inserted near the interface.

We speculate that the findings above might be due to the structural distortion near the interface. On the one hand, the monolayer O atoms are necessary to not only suffice removal of the dangling bonds originating in SiC slab, but also to serve as anions of Al_2O_3 slab. In the primary interface without involvement of H and N, SiC (0001) provides insufficient places

for both the O atoms from Al_2O_3 slab and monolayer O atoms. Some of the monolayer O atoms are dragged into the oxide leaving SiC distorted, which leads to a large strain between Si and C atoms. As a result, one of C atoms in top SiC layer is short of bonds that causes the observed mid-gap states. On the other hand, H or N insertion can drastically alleviate the local strain in top SiC layer. Consequently, this effectively remove the mid-gap states observed at similar energy levels. The results of our calculations find clear support for a recent experiment performed by Jayawardhena et al. [155]. They found that H_2 annealing at high temperature prior to ALD leads to lower interface trap density, and this reduction is further enhanced through sacrificial oxidation in NO followed by H_2 annealing, resulting in improved channel mobility and stability for the Al_2O_3/4H-SiC MOSFETs.

5.5 LiF/4H-SiC Interfaces

The LiF/4H-SiC epitaxy is formed using LiF in FCC phase and 4H-SiC, as described in Table 5.2. This epitaxial relation creates interface in a Monoclinic unit cell that consists of 6 layers SiC and ∼20 Å thick LiF for capturing the bulk properties of each. LiF layers bear a lateral strain of 4.2% while holding the in-plane lattice constants same as those of SiC. Note that we have considered interface system with low strain although the supercell is still large (as approximately large as 370 atoms).

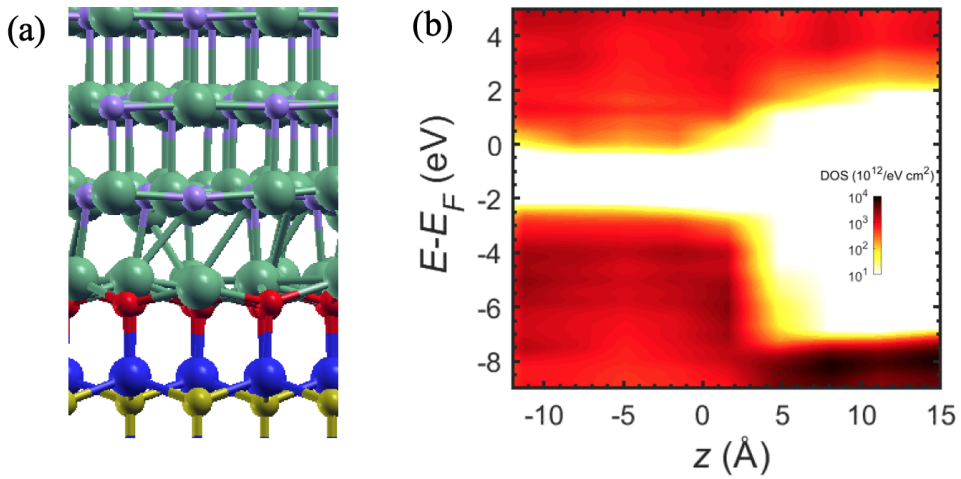

Figure 5.2: (a) Schematics of LiF/SiC interfaces with monolayer O atoms and (b) its in-plane average local DOS profiles (in log scale) along z direction. The position z is referred to the topmost C plane; the conduction band minima is set at 0.

Based on the results from Chapter 3, forming energetically and chemically stable LiF/4H-SiC might require compensation of atomic density mismatch between the SiC substrate and LiF film to a certain extent. Similarly, we simulate the resulting SiC surface from oxidation process by introducing a monolayer of O atoms. As seen in Fig. 5.2 (a), those O atoms form bonds with Li atoms from the bottom atomic layer of LiF while passivating the SiC (0001). In addition to Si atom, it is evident that each O atom has more nearest Li neighbors.

In order to quantify the effect of the monolayer O on LiF/4H-SiC interface, the in-plane average of the local DOS is analyzed and the result is shown in Fig. 5.2 (b). It is no surprising that the band gaps of both SiC and LiF are found consistently to be smaller than the values from experiments due to the limitations of DFT calculations. Nevertheless, a further novel finding is that no mid-gap states are observed across the interface, which supports the notion that an oxidized SiC surface is beneficial for preparation of LiF/4H-SiC interface. We speculate that this might be due to that those O atoms are treated as F atoms to form ionic bonds with Li atoms while transiting the atomic densities well from SiC to LiF.

5.6 AF$_2$/4H-SiC Interfaces

The AF$_2$/4H-SiC systems are formed by AF$_2$ (A = Mg and Ca) dielectric films and 6 layers of SiC, where the C face is terminated with H atoms. The epitaxy of these interfaces accommodates thick MgF$_2$ layers on ($\sqrt{3} \times \sqrt{3}$)-SiC or ($\sqrt{3} \times \sqrt{3}$)-CaF$_2$ layers on 4H-SiC slab with 13 unit cells of cross section leading to hexagonal unit cell, where the in-plane lattice constants are set to be those of 4H-SiC, yielding 2.2% (4.8%) lateral strain applied to MgF$_2$ (CaF$_2$) in Tetragonal (Face-Centered Cubic) phase (see Table 5.2). Note that although we pick the best eptaxies among considerable searches, the AF$_2$/4H-SiC interfaces discussed here still exhibit certain polar instability that arises in epitaxial AF$_2$ polar surfaces. Firstly, similar monolayer O is employed to MgF$_2$/4H-SiC and CaF$_2$/4H-SiC interfaces, as seen in Fig. 5.3 (a) and (c), respectively. The monolayer O is bonded to alkaline earth metals near the interfaces producing an oxidized SiC surface. Alternatively, as illustrated in Fig. 5.3 (b) and (d), excess F atoms are added not only directly at the Si face but also extend within AF$_2$ very close to the interfaces.

The amount and locations of F atoms that have been added play an active role in modifying the properties of the interfaces. More details will be discussed in the following.

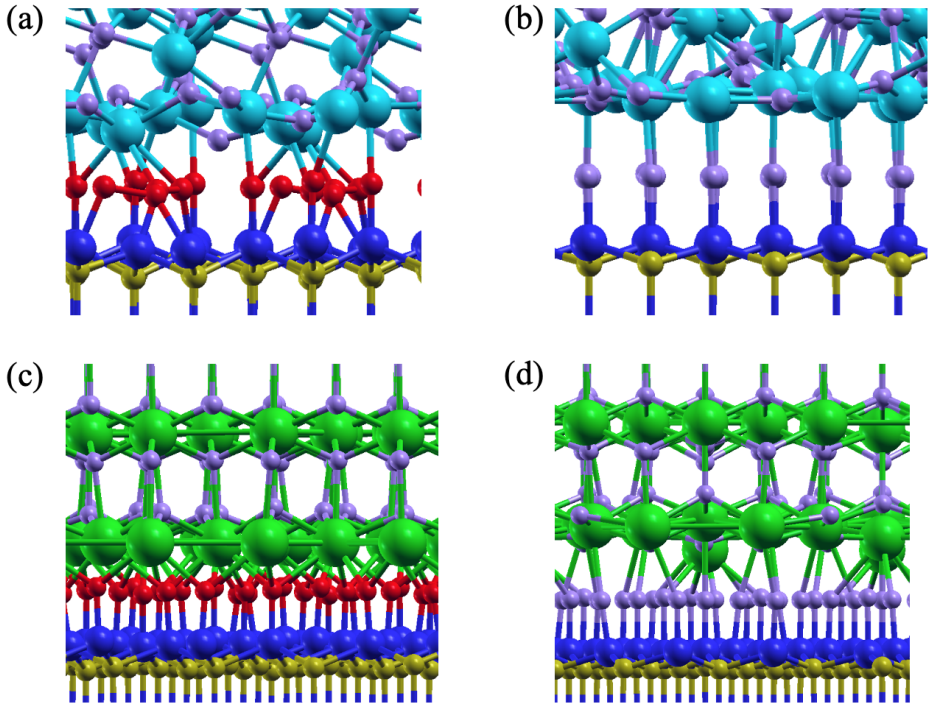

Figure 5.3: Schematic representation of MgF_2/4H-SiC interfaces: (a) with monolayer O atoms and (b) with insertion of excess F atoms; Schematic representation of CaF_2/4H-SiC interfaces: (c) with monolayer O atoms and (d) with insertion of excess F atoms.

The resulting in-plane average of the local DOS for these AF_2/4H-SiC systems is illustrated in Fig. 5.4. On the one hand, our results demonstrate a roughly consistent band gaps in SiC, MgF_2 and CaF_2 slabs regardless of surface treatments. On the other hand, based on the analysis of other interfaces described prior, O or F treatments, as a result of density mismatch compensation between SiC and AF_2 dielectrics, gives clearly better results with no substantial mid-gap states when comparing to primordial interfaces without any treatment.

One concern about the findings from this analysis is that the band-offsets appear to be questionable, especially regarding the MgF_2/4H-SiC interfaces, F passivation reverses the results from O termination. This does not seem to depend on the choice of surface treatments, but as inherited from the epitaxial dielectric slab. As noted earlier, the polar surface such as the epitaxial MgF_2 slab gives rise to the polar instability of the interfaces. We sought to change the charge distribution of the interfaces via insertion of F atoms, so that the polar instability of the

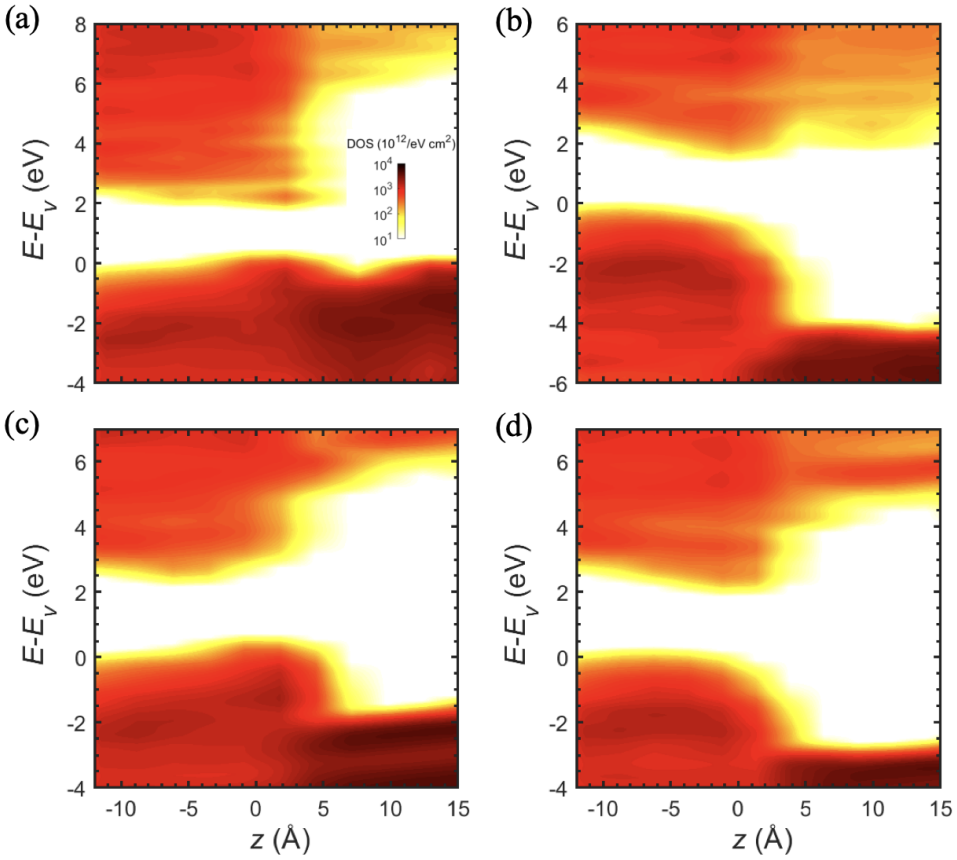

Figure 5.4: In-plane average local DOS profiles (in log scale) along z direction for (a-b) MgF_2/4H-SiC and (c-d) CaF_2/4H-SiC interfaces with monolayer O atoms and insertion of excess F atoms, respectively. The position z is referred to the topmost C plane; the valence band maximum is set at 0.

interfaces can be fairly resolved. The limitation of this method however is that the dipole can not be completely removed in the case of MgF_2/4H-SiC interfaces, which causes the drastic changes in band-offsets. This is very much the major obstacle in future attempts to produce more realistic MgF_2/4H-SiC interfaces with appropriate band offsets. Our next step may be searching for either different epitaxies or advanced surface treatments.

5.7 Band Alignments for High-κ dielectrics/4H-SiC Interfaces

In order to measure the experimental band alignments between 4H-SiC and high-κ dielectrics, a $\sim$350 (20$\sim$30) Å thick Al_2O_3 (MgF_2) film is deposited on thermally oxidized n-type 4H-SiC (0001). With these well-prepared samples, the valence band offset (ΔE_V) between dielectric and SiC can be measured by X-ray photoelectron spectroscopy (XPS), and the band gap (E_g^{diel}) of dielectric material is determined from reflection electron energy loss spectroscopy (REELS).

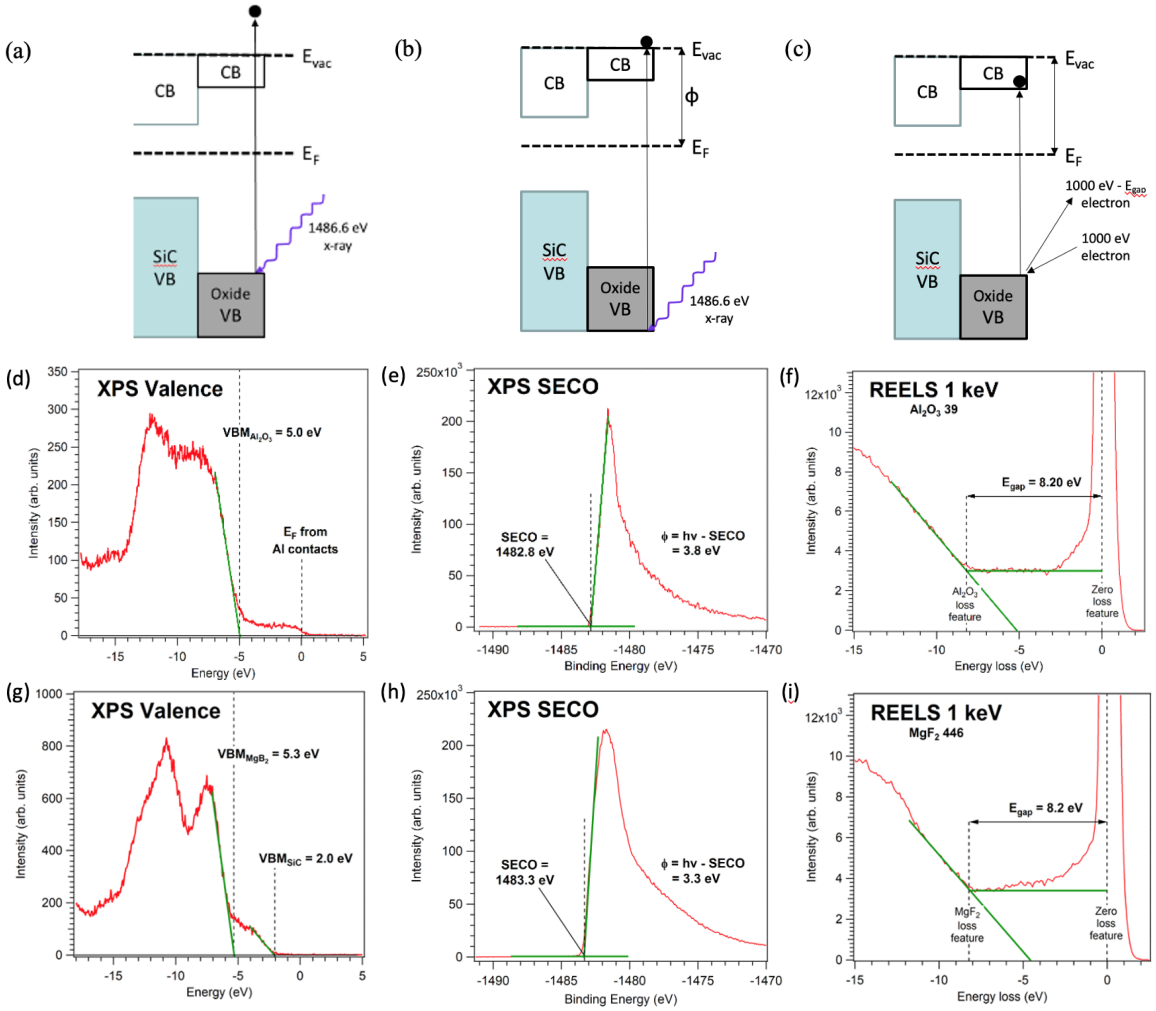

Figure 5.5: (a-c) Schematics of experimental techniques employed for determining band alignments between SiC and oxide; For Al_2O_3/4H-SiC sample prepared by Dr. D. Morisette and group (Purdue) and MgF_2/4H-SiC sample prepared by Dr. A. C. Ahyi (AU) and Dr. Victor Adedeji (Elizabeth City State Univ., NC), analysis of valence band maximum from (d,g) XPS spectra, work function from (e,h) XPS SECO spectra and dielectric band gap from (f,i) REELS data.

Accordingly, the conduction band offset (ΔE_C) can be computed by Eq. 5.1:

$$\Delta E_C = E_g^{diel} - \Delta E_V - E_g^{SiC} \tag{5.1}$$

where the band gap (E_g^{SiC}) of 4H-SiC is assumed to be 3.2 eV.

The experimental measurement, as schematically shown in Fig. 5.5, proceeds in two stages by Dr. Leonard Feldman's group from Rutgers University: (1) XPS measures the binding energies of the least tightly bound electrons (Fig. 5.5 (a)). As a result, the VBM is determined

based on the intersection of the flat XPS energy approaching the valence band of the dielectric and the linear fit of the leading valence band edge in the XPS data (Fig. 5.5 (d) and (g)). In addition, as the dielectric layer above SiC is thin, the VBM of SiC can also been identified in the same XPS data. Furthermore, electrons residing deeply inside the valence bands can be excited to vacuum level using x-ray source (hv = 1486.6 eV) (Fig. 5.5 (b)) to measure the difference to Fermi level that defines work function. As illustrated in Fig. 5.5 (e) and (h), SECO spectra are analyzed by similar linear extrapolation of features to zero intensity to measure the work function; (2) REELS is performed to excite 1 keV electrons from valence band to conduction band and measure energy loss of reflected beam (Fig. 5.5 (c)). Subsequently, the band gap is computed from the energy difference between the 1 keV electrons and the energy loss of reflected beam. In the REELS spectra (Fig. 5.5 (f)) and (i) zero loss feature corresponds to 1 keV electrons, the intersection of the zero intensity bar and the linear fit of the Al_2O_3 or MgF_2 loss feature corresponds to the reflected electrons beams. Some uncertainty in the band gap measurement is evident due to the uncertainty in position of the zero-intensity bar.

Simultaneously, theoretical band alignments for the interface models described earlier in this chapter are computed using the approach as discussed in Section 2.8. Here we compare the results from calculations with experiments in Table 5.3. The band gaps computed from HSE calculations for most high-κ dielectrics are consistent with experimental measurements except for the case of CaF_2. Regarding the band-offsets of Al_2O_3/4H-SiC interfaces, the discrepancy between the calculations and experimental measurements involves two simplifying assumptions. First, the samples are prepared without the process introducing H or N element, different from our model. Second, ALD Al_2O_3 in experiments is amorphous, on the contrary we adopt crystalline Al_2O_3 in the calculations.

As mentioned previously, MgF_2/4H-SiC interface models are treated using monolayer O or F passivation. The calculated ΔE_V (ΔE_C) of the former is apparently lower (higher) than that of the latter. In comparison with experimental band-offsets of thermally oxidized MgF_2/4H-SiC sample, the calculated ΔE_V (ΔE_C) is found to be much lower. In addition, the calculated band-offsets of LiF/4H-SiC and CaF_2/4H-SiC interfaces require future experimental

Table 5.3: Dielectric constants (κ) of bulk high-κ dielectrics, band gaps (E_g) of epitaxial high-κ dielectrics, valence band (ΔE_V) and conduction (ΔE_C) band-offsets of 4H-SiC/high-κ dielectrics interfaces obtained from calculations. Available experimental values shown in parentheses.

Interface type	κ	E_g (Expt.) (eV)	ΔE_V (Expt.) (eV)	ΔE_C (Expt.) (eV)
Al_2O_3/4H-SiC	10.6(9.0)	8.2(8.2)	1.9^N-2.0^H(3.0)	3.0^H-3.1^N(2.0)
LiF/4H-SiC	8.3(8.3)	11.6(13.6)	6.3^O	2.1^O
MgF_2/4H-SiC	5.3(4.9-5.9)	8.6(8.2)	1.5^O-5.0^F(3.3)	0.5^F-4.0^O(1.7)
CaF_2/4H-SiC	7.5(6.8-7.4)	9.8(12.0)	3.4^O-4.6^F	2.0^F-3.3^O

measurements for validations. Together, our analysis of band alignments for these models indicate the novelty of surface treatments that can significantly impact the results.

Chapter 6

$Mg_xCa_{1-x}O$/SiC Interface

6.1 Summary

In this chapter, we analyze the properties of $Mg_xCa_{1-x}O$/4H-SiC (0001) interface via first principles calculations within the density functional theory (DFT). The crystal structures of the ternary dielectric $Mg_xCa_{1-x}O$ are formed via randomly substitution of Mg atoms with Ca atoms. Analysis of the structural properties of $Mg_xCa_{1-x}O$ ternaries with different compositions reveals that $Mg_{0.74}Ca_{0.26}O$ presents the lowest lattice mismatch with 4H-SiC. In addition, the band offsets of $Mg_{0.74}Ca_{0.26}O$/4H-SiC (0001) interface are determined by combining electrostatic potential-based alignment method [100, 101] and Vegard's law. The valence band offset is estimated to be 2.5 eV and the conduction band offset is deduced to be 1.6 eV, indicating that the $Mg_xCa_{1-x}O$ produces roughly the same valence band offset with 4H-SiC in comparison with MgO (111)/4H-SiC and SiO_2/4H-SiC but smaller conduction band offset value than SiO_2/4H-SiC [67, 125]. Hence, this work highlights the significance of accurate determination of valence and conduction band offsets for the applications of $Mg_xCa_{1-x}O$/4H-SiC (0001) systems.

6.2 Background

In addition to the alternative gate dielectrics for 4H-SiC studied in previous chapters (Al_2O_3, LiF and AF_2), other binary dielectrics have also been proposed as the gate dielectrics to reduce the gate leakage currents. For instance, MgO is of particular interest due to its large band gap (7.8 eV) [157, 158] and high dielectric constant (κ = 9.8) [158]. MgO has a rocksalt

crystal structure, as shown in Fig. 6.1, that possesses $\sim$3% lattice mismatch with 4H-SiC when being deposited along the (111) face. Thus, most of the research focuses on the deposition methods [159, 160], band gap measurement [161] and band alignment [162, 163] of MgO/SiC interface. Similarly, CaO crystallizes in the rocksalt structure with high dielectric constant (κ = 11.8) [164] and large band gap (6$-$8 eV) [165, 166, 167], suitable as a gate dielectric for 4H-SiC.

The ternary dielectric $Mg_xCa_{1-x}O$ that preserves a rocksalt like structure is recently under the spotlight for SiC-based power electronic device. Here x in the definition is the composition of Mg atoms in the system. It is worth noting that the lattice constants are highly dependent on the composition of $Mg_xCa_{1-x}O$. By tuning the composition of $Mg_xCa_{1-x}O$ toward the substrate lattice constant, Bhuiyan et al. [168] and Lou et al. [169] have demonstrated the suitability of $Mg_xCa_{1-x}O$ film as a gate dielectric for GaN-based device. Therefore, it is highly possible to deposit $Mg_xCa_{1-x}O$ film on 4H-SiC (0001) that is similar to GaN (0001). From experiments, $Mg_{0.72}Ca_{0.28}O$ film has proven to show the highest epitaxy quality on 4H-SiC (0001) that was investigated and confirmed by cross-sectional transmission electron microscopy and X-ray diffraction [170]. However, to our knowledge, no study has yielded the band alignment of $Mg_xCa_{1-x}O$/4H-SiC interface. This study is an attempt to fill this gap, providing confirmatory evidence for the application of $Mg_xCa_{1-x}O$ as the gate dielectric for 4H-SiC.

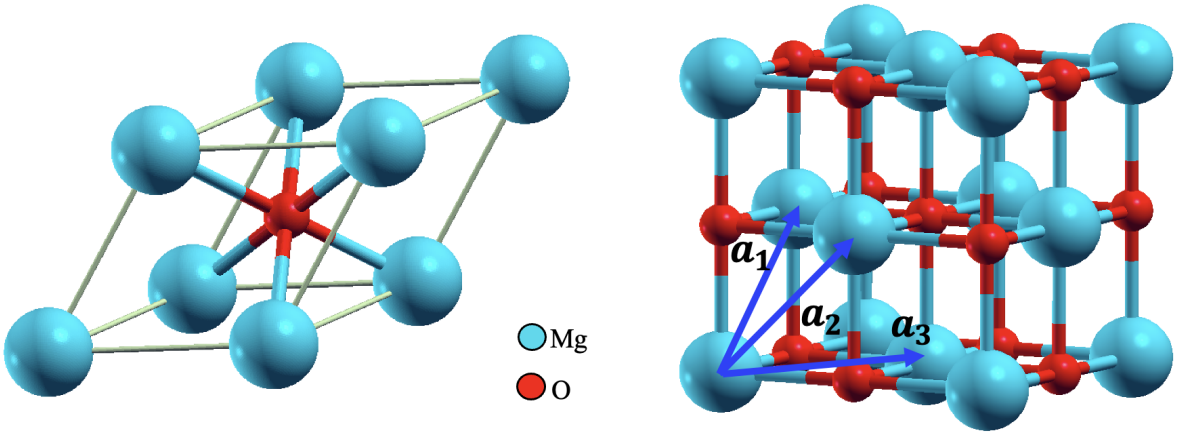

Figure 6.1: Crystal structure of rocksalt MgO: (left) primitive unit cell defined by primitive lattice vectors (b) conventional unit cell. The primitive lattice vectors $\mathbf{a_x}$ (x=1,2,3) shown in arrows (blue).

6.3 Computational Details

For the interface and bulk models described in forthcoming sections, in addition to the computational details described in Section 2.9, atomic positions are fully relaxed while the convergence thresholds of total energy and forces for ionic minimization is set to 3.0×10^{-4} Ry and 5 meV/Å, respectively. The Brillouin zone (BZ) is sampled using a Monkhorst-Pack mesh [120], where BZ integration is per-formed using Methfessel-Paxton first-order spreading [171] (see Table 6.1). The $Mg_xCa_{1-x}O$/4H-SiC interface calculations corresponding to large supercells (as large as $\sim$ 350) are performed with a Brillouin-zone sampling restricted to the Γ point. The core electrons are described with projector augmented wave (PAW) pseudopotentials [109] using energy cutoffs of 60 Ry and 400 Ry for the wave function and density, respectively.

Table 6.1: Number of atoms (nat), Monkhorst-Pack k-point mesh for sampling the BZ and PBE lattice constant (a) for $Mg_xCa_{1-x}O$ ternary, MgO/4H-SiC and $Mg_xCa_{1-x}O$/4H-SiC interfaces.

System	nat	k-point mesh	a (Å)
MgO/4H-SiC	35	$8\times8\times1$	3.09
$Mg_xCa_{1-x}O$	162	$2\times2\times1$	9.28
$Mg_xCa_{1-x}O$/4H-SiC	315	Γ	9.28

6.4 MgO/4H-SiC Interface

As described previously, the epitaxy of MgO (111)/4H-SiC interface is formed by depositing the Face-Centered Cubic (FCC) Bravais lattice of MgO (ICSD 159375) along the (111) face on 1×1 4H-SiC, where a $\sim$3% lateral tensile strain is applied to MgO layers while the in-plane lattice constant is set to be that of 4H-SiC ($a = b = 3.09$ Å). In order to examine the property changes stemming from the SiC Si or C face, as shown in Figs. 6.2 (a) and (b), the supercells of MgO (111)/4H-SiC (0001) and MgO (111)/4H-SiC ($000\bar{1}$) are created by depositing epitaxial MgO layer on Si and C face of 4H-SiC, respectively. These two models include at least 15 Å perpendicular vacuum space relative to their interface. In order to diminish the edge states, the end surfaces of both interfaces are passivated by H atoms. Additionally, the third supercell noted as MgO (111)/4H-SiC excludes the vacuum space in order to assume periodic boundary conditions in all three dimensions, as seen in Fig. 6.2 (c). All three of the

systems brings about no concern of any interfacial defect state arose from dangling bonds near the interface.

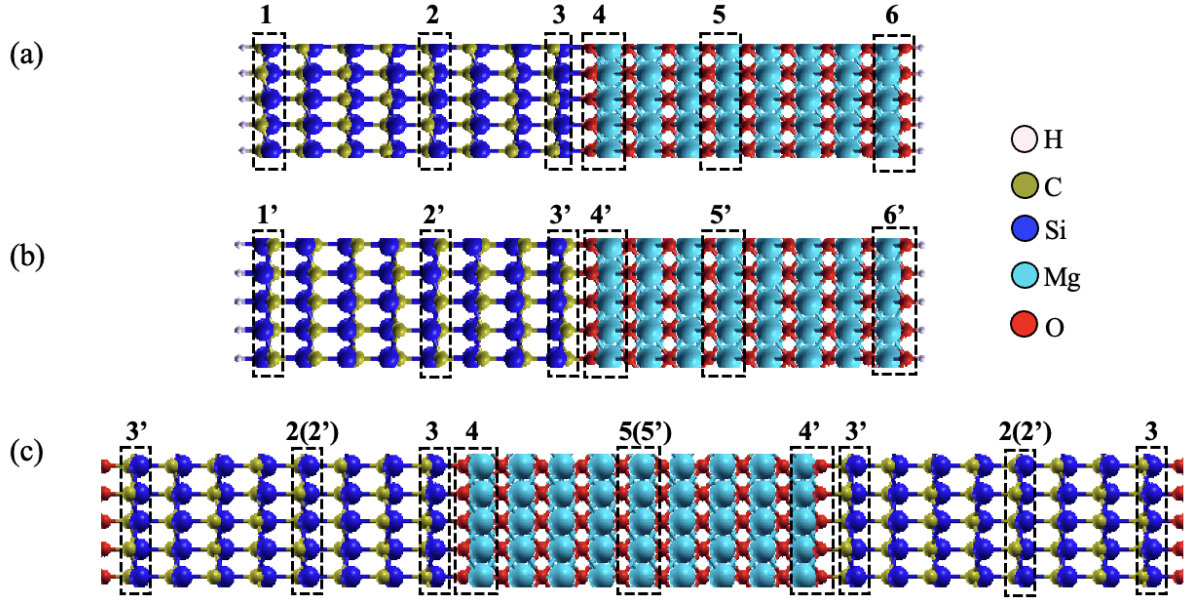

Figure 6.2: Schematic representations of MgO (111)/4H-SiC interfaces: (a) MgO (111) on the 4H-SiC (0001) Si face including vacuum space along z direction (b) MgO (111) on the 4H-SiC $(000\bar{1})$ C face including vacuum space along z direction and (c) MgO (111) on the 4H-SiC with periodic boundary conditions in three dimensions. The atom layers embraced by the dashed lines are labeled by numbers indicating different positions along z direction.

The electronic band structures of the modeled MgO (111)/4H-SiC (0001), MgO (111)/4H-SiC $(000\bar{1})$, MgO (111)/4H-SiC interfaces are analyzed and plotted in grey lines as seen in Fig. 6.3 (a-c), correspondingly. In order to visualize the contribution to the overall electronic band structure by the atom layers labeled in Fig. 6.2 (a), the projections of Bloch states onto localized atomic orbitals of C (yellow), Si (blue), O (red), and Mg (cyan) atoms residing in those layers representing the end surface, bulk or near-the-interface regions are superimposed on the total band structures as seen in Fig. 6.3. The results from this analysis demonstrate two things. First, MgO (111)/4H-SiC (0001) (Fig. 6.3 (a)) and MgO (111)/4H-SiC interfaces (Fig. 6.3 (c)) produce roughly identical electronic band structures and atomic projections for atoms from the same or equivalent surface or region, for instance, atomic projections for atoms from layer 2 to 5 as noted. This indicates the vacuum space is not essential in the calculations. Second, with the vacuum space in MgO (111)/4H-SiC (0001) (Fig. 6.3 (a)) and MgO (111)/4H-SiC $(000\bar{1})$ (Fig. 6.3 (b)), the atomic projections for MgO layer (layer 4 (4') as noted) due to the transition

from Si-O bonds to C-O bonds, seem to shift both the conduction and valence bands towards the Fermi level. Nonetheless, the atomic projections for similar Si or C atoms agree nearly one another, implying that the effect of the SiC Si or C face on the band structure is neglected. Employing the method discussed in Section 2.8, the valence band (ΔE_V) and conduction band

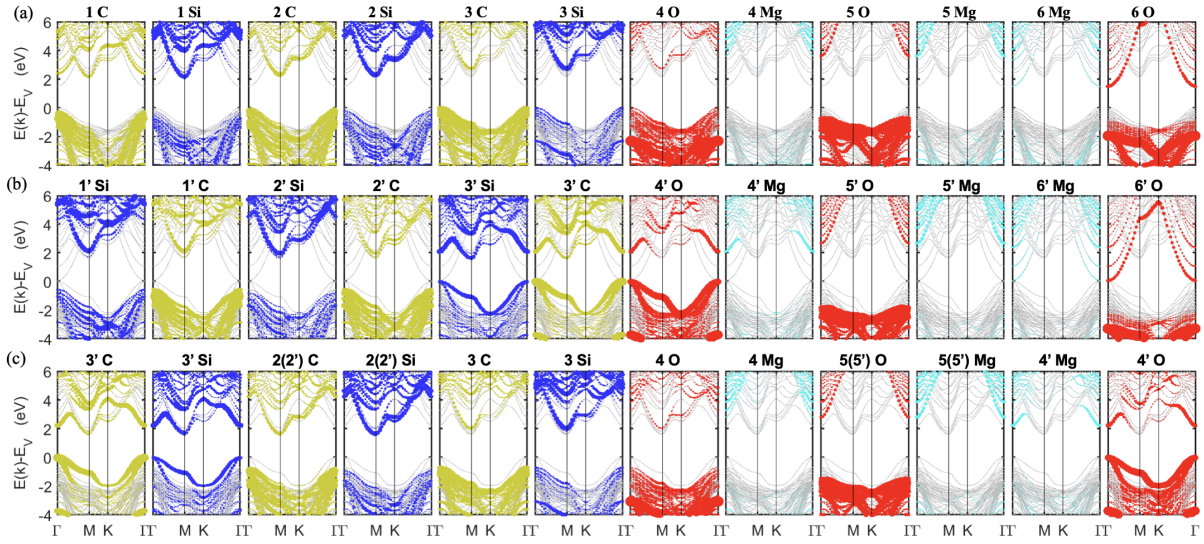

Figure 6.3: The electronic band structures (as shown in light grey lines) of MgO (111)/4H-SiC interfaces: MgO (111)/4H-SiC interfaces: (a) MgO (111) on the 4H-SiC (0001) Si face including vacuum space along z direction (b) MgO (111) on the 4H-SiC ($000\bar{1}$) C face including vacuum space along z direction and (c) MgO (111) on the 4H-SiC with periodic boundary conditions in three dimensions where atomic projections for C (yellow), Si (blue), O (red), Mg (cyan) atoms in layers labeled in Fig. 6.2 are plotted in panels as noted.

(ΔE_C) offsets of MgO/4H-SiC interface are determined by choosing the optimum mixing parameter (0.25 for SiC and 0.35 for MgO) in the HSE calculations. In comparison with the experimental ΔE_V of 3.65 eV and ΔE_C of 0.92 eV [162], we found that the band alignment with ΔE_V of 2.0 eV and ΔE_C of 2.5 eV.

6.5 $Mg_xCa_{1-x}O$ Ternaries

In order to build the primitive unit cell of $Mg_xCa_{1-x}O$ that can be epitaxially matched with 4H-SiC, the FCC Bravais lattice of MgO (see Fig. 6.1) is converted into a hexagonal unit cell that is then repeated three times in three directions. Correspondingly, the number of both Mg and O atoms in the enlarged hexagonal unit cell is increased by a factor of 27. Subsequently, a portion of Mg atoms in the new unit cell is randomly substituted by Ca atoms resulting in a

configuration of $Mg_xCa_{1-x}O$ ternary. This is achieved in two steps: 1) selecting unique indices of Mg atoms randomly in the unit cell that correspond to a certain amount of Mg atoms by employing "randperm" function in Matlab; 2) replacing all selected indices of Mg atoms with Ca atoms while other atoms remain the same.

An apparent limitation of the method above is that $Mg_xCa_{1-x}O$ ternary can not be considered as conclusive for a specific value of x because of merely one random selection process. Therefore, more selections for the ternary are necessarily conducted. In order to have sufficient candidate configurations of the compound as well as manageable calculations in DFT, we run the random selections 20 times. Namely, 20 distinct configurations of $Mg_xCa_{1-x}O$ for a specific value of x differ at least one of the replaced Mg atoms from one another, though there is consistently same amount of Mg atoms being substituted by Ca atoms.

Table 6.2: Number (no.) of Mg (Ca,O) atoms in $Mg_xCa_{1-x}O$, PBE lattice constant (a_{DFT}) in hexagonal unit cell of crystals (a_{DFT} for $Mg_xCa_{1-x}O$ shown here is the average value in the equivalent hexagonal unit cell for the FCC Bravais lattice of MgO), lattice constant (a_V) from Vegard's law.

Crystal	Mg no.	Ca no.	O no.	a_{DFT}	a_V
$Mg_{0.26}Ca_{0.74}O$	21	60	81	3.32	3.31
$Mg_{0.51}Ca_{0.49}O$	41	40	81	3.22	3.21
$Mg_{0.74}Ca_{0.26}O$	60	21	81	3.13	3.11
MgO				3.00	
CaO				3.41	
4H-SiC				3.09	

The lattice constant is highly dependent upon the composition of $Mg_xCa_{1-x}O$ ternary. In order to determine the composition of $Mg_xCa_{1-x}O$ leading to small enough lattice mismatch with 4H-SiC, here we explore the structural properties of three $Mg_xCa_{1-x}O$ ($x = 0.26, 0.51, 0.74$) ternaries. As seen in Table 6.2, the primitive unit cells of $Mg_{0.26}Ca_{0.74}O$, $Mg_{0.51}Ca_{0.49}O$, and $Mg_{0.74}Ca_{0.26}O$ are formed by randomly replacing 60, 40, and 21 Mg atoms in the enlarged hexagonal unit cell that containing 81 Mg atoms and 81 O atoms, respectively. For each ternary (with a specific value of x), the ground state of 20 distinct configurations are obtained by allowing the entire supercell and all atoms to fully relax within DFT. The configuration with the lowest DFT energy is identified to be most stable for further evaluation of

properties. For instance, $Mg_{0.74}Ca_{0.26}O$ supercell as depicted in Fig. 6.4 is the most stable one amongst 20 configurations.

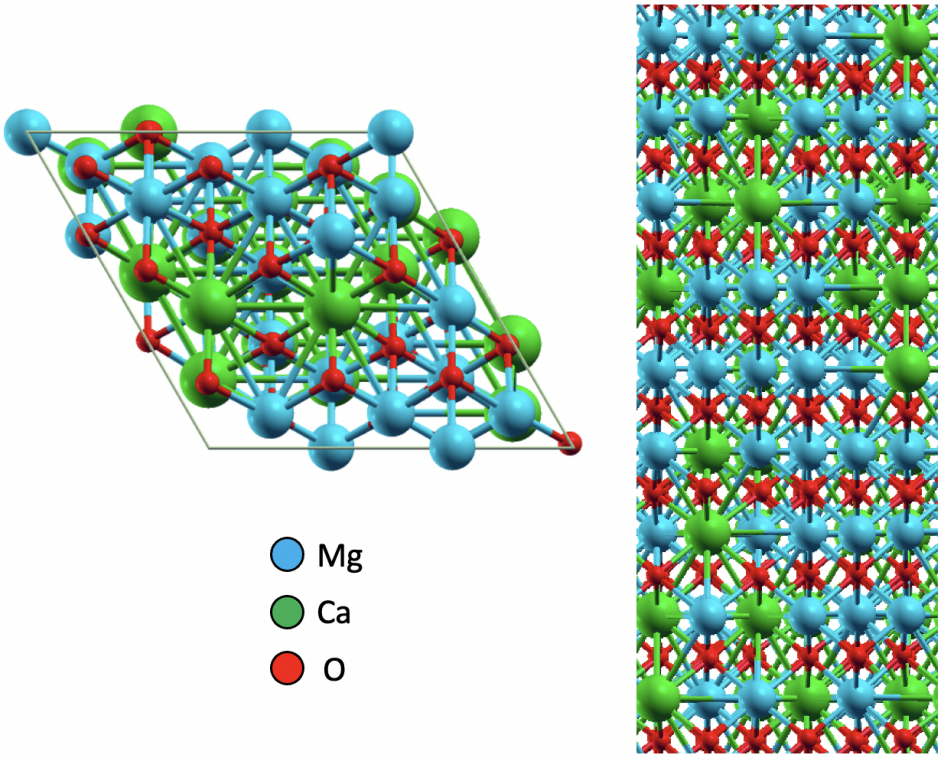

Figure 6.4: Top and side schematic of the $Mg_{0.74}Ca_{0.26}O$ supercell. Solid lines in the cross-sections mark the primitive unit cell.

Our argument in favor of picking from a pool of 20 configurations runs as analysis on the unit cell volume variation (ΔV_{uc}) and band gap variation (ΔE_g), as illustrated in Fig. 6.5. For the 20 configurations in each ternary, ΔV_{uc} (ΔE_g) is the percentage change in unit cell volume (band gap) with respect to the configuration with lowest DFT energy. We observe that within a small range of energy per atom difference from the lowest (ΔE_b), the unit cell volume of the 20 configurations for $Mg_{0.74}Ca_{0.26}O$ (green) has a smaller variation in comparison with $Mg_{0.26}Ca_{0.74}O$ (blue) and $Mg_{0.51}Ca_{0.49}O$ (red). In particular, we see more configurations with lower energies have unnoticeable changes in unit cell volume for $Mg_{0.74}Ca_{0.26}O$. Similarly, the stable configuration of $Mg_{0.74}Ca_{0.26}O$ at 0 has more neighbors indicating that more configurations for this ternary have comparable band gap and energy. We choose the lowest DFT energy configuration from the 20 samples analyzed. The similar properties obtained for the most stable

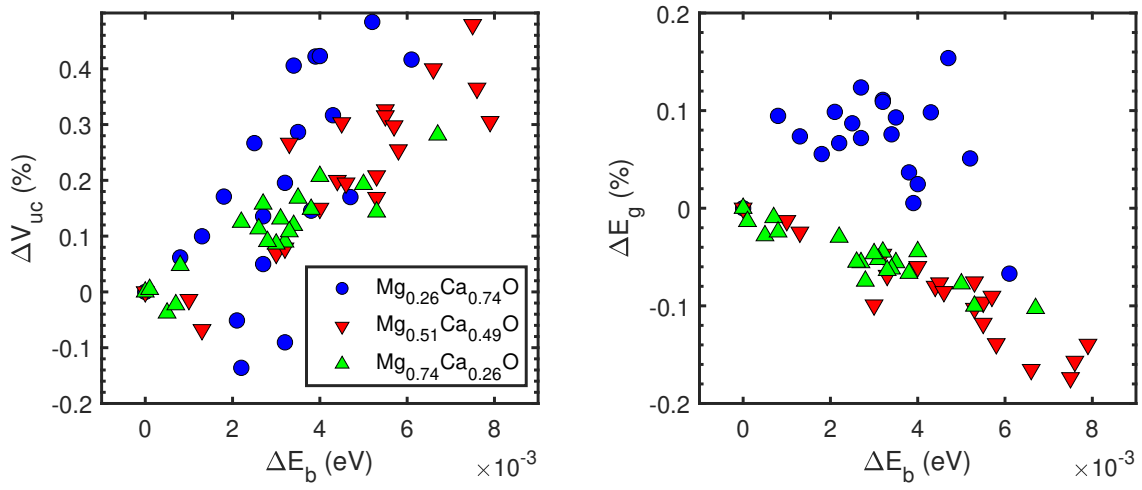

Figure 6.5: (Left) The unit cell volume variation (ΔV_{uc}) as a function of energy per atom variation (ΔE_b); (Right) The band gap variation (ΔE_g) as a function of energy per atom variation (ΔE_b).

configurations of the $Mg_{0.74}Ca_{0.26}O$ suggests that different choices may not exhibit significant outcomes.

Additionally, the optimized PBE lattice constants a_{DFT} of the most stable $Mg_xCa_{1-x}O$ ($x = 0.26, 0.51, 0.74$) configurations from relaxation, as shown in Table 6.2, are converted into an arithmetic average value in the equivalent hexagonal unit cell for the FCC Bravais lattice of MgO. It is more convenient to compare this value to the lattice constant of 4H-SiC. On the other hand, we can estimate the lattice constant of $Mg_xCa_{1-x}O$ from Vegard's law. This empirical prediction states a linear interpolation between the lattice parameters of a solid solution and its two constituents, as defined by Eq. 6.1 [172]

$$a_{A_{(1-x)}B_x} = (1-x)a_A + xa_B \tag{6.1}$$

where $a_{A_{(1-x)}B_x}$ is the lattice parameter of the solid solution, a_A and a_B are the lattice parameters of the pure constituents, and x is the molar fraction of component B in the solid solution. It has also proven that Vegard's law can be applied to the band gap [173].

We obtain the optimal lattice constants of rocksalt MgO (ICSD 159375) and rocksalt CaO (ICSD 61550) from DFT calculations, as seen in Table 6.2, the lattice constant a_V of $Mg_xCa_{1-x}O$ ($x = 0.26, 0.51, 0.74$) are then computed according to Eq. 6.1. For each ternary,

their lattice constants obtained from DFT calculations are in good agreement with Vegard's law. In addition, we find that $Mg_{0.74}Ca_{0.26}O$ has $\sim 1\%$ lattice mismatch from 4H-SiC. This composition of $Mg_xCa_{1-x}O$ exhibit roughly quantitative agreement with available experimental results that $Mg_{0.72}Ca_{0.28}O$ film shows the highest epitaxy quality on 4H-SiC (0001) [170]. From these results it is clear that a more realistic interface can be achieved while depositing $Mg_{0.74}Ca_{0.26}O$ layers on 4H-SiC.

6.6 $Mg_xCa_{1-x}O$/4H-SiC Interface

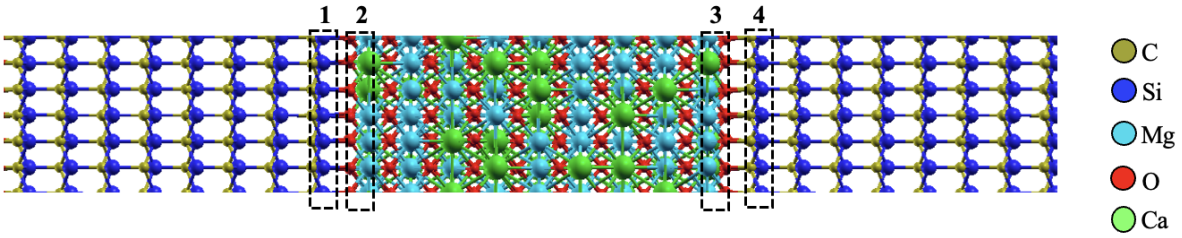

Figure 6.6: Side schematic of the $Mg_{0.74}Ca_{0.26}O$/4H-SiC supercell. Periodic boundary conditions are assumed in three directions.

The $Mg_{0.74}Ca_{0.26}O$/4H-SiC system as shown in Fig. 6.6 is formed by joining 8 layers SiC and $\sim$20 Å thick $Mg_{0.74}Ca_{0.26}O$ slab. As discussed prior, the ternary is modeled from 3×3 MgO (111), thus the $Mg_{0.74}Ca_{0.26}O$/4H-SiC system accommodates (3×3)-SiC while a $\sim 1\%$ lateral tensile strain is applied to the dielectric layers. Based on the results in Section 6.4, the superlattice calculation excludes vacuum space along z direction by assuming periodic boundary conditions in all three directions.

The electronic band structures of the $Mg_{0.74}Ca_{0.26}O$/4H-SiC interface are depicted in Fig. 6.7. The atomic projections for atoms from the layers as noted in Fig. 6.6 are superimposed on the total bands (grey lines). The O atoms near the interfaces are strongly coupled with Si or C face. In particular, we observe more edges states attributed to O (red), C (yellow) and Si (blue) near the C face. This result appears to suggest that Si-O bonds are more inert than C-O bonds near the $Mg_{0.74}Ca_{0.26}O$/4H-SiC interface. Therefore, it is anticipated to have epitaxial $Mg_{0.74}Ca_{0.26}O$ grown by molecular beam epitaxy (MBE) on SiC (0001) rather than

$(000\bar{1})$. Indeed, epitaxial $Mg_{0.75}Ca_{0.25}O$ grown by MBE on SiC (0001) has been previously reported as an alternative dielectric oxide [174].

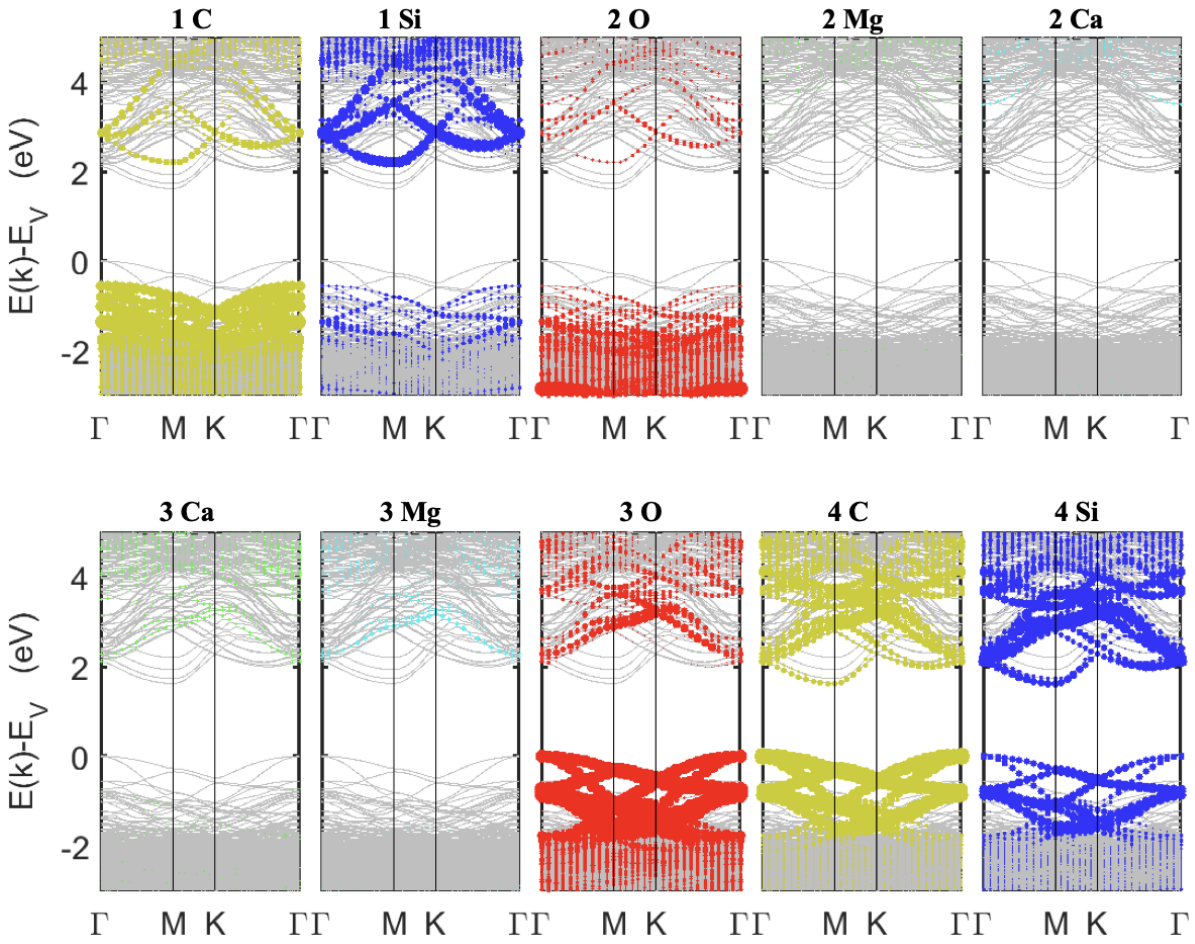

Figure 6.7: The electronic band structures (as shown in grey lines) of $Mg_{0.74}Ca_{0.26}O$/4H-SiC interface. The boundary conditions are assumed in three directions. Atomic projections for C (yellow), Si (blue), O (red), Mg (cyan), and Ca (green) atoms in layers labeled in Fig. 6.6 are plotted in panels as noted.

For $Mg_{0.74}Ca_{0.26}O$/4H-SiC interface, it is not feasible to determine the band offsets ΔE_V and ΔE_C directly from the electrostatic potential-based alignment method as described in Section 2.8. As seen in Table 6.2, there are total 162 atoms in the unit cell of $Mg_{0.74}Ca_{0.26}O$. Therefore, the electronic band structure calculations for $Mg_{0.74}Ca_{0.26}O$ using HSE functional is computationally expensive. In order to tackle this issue, we determine the local band edge with respect to the electrostatic potential and the band gap of bulk $Mg_{0.74}Ca_{0.26}O$ from Vegard's law. As shown in Fig. 2.8, affordable HSE calculations are first performed independently for bulk MgO or CaO to obtain their band gaps, electrostatic potentials and local edge edges. The

band gaps are roughly in agreement with experimental values when the mixing parameter is 0.35 for both dielectrics. Then, the $Mg_{0.74}Ca_{0.26}O$/4H-SiC interface calculation finds the electrostatic potential difference between the bulk-like regions of the ternary and 4H-SiC. Lastly, the valence band edge with respect to the electrostatic potential interpolated from Vegard's law (Eq. 6.1) are aligned by the potential difference from interface calculation.

The results for both MgO (111)/4H-SiC and $Mg_{0.74}Ca_{0.26}O$/4H-SiC interfaces are listed in Table 6.3. In addition to the band gap of SiC (3.2 eV), the band gaps of the reference bulk components are found to be 7.7 eV for MgO and 6.1 eV for CaO. Based on Vegard's law, the band gap of $Mg_{0.74}Ca_{0.26}O$ is 7.3 eV . Overall, we obtain reasonable band offsets of $Mg_{0.74}Ca_{0.26}O$/4H-SiC interfaces with the simple method described previously. Its valence band offset is slightly larger than that of MgO (111)/4H-SiC, while the conduction band offset is roughly 1 eV smaller. In addition, MgO (111)/4H-SiC has nearly the same ΔE_V but much smaller ΔE_C when compared to the SiO_2/4H-SiC interface. Note that the band offset errors in the calculations may exceed 1 eV. This is primarily due to the uncertainty in the band gap of CaO that in fact has been previously reported ranging from 6 to 8 eV [165, 166, 167]. Our results casts a new light on the application of $Mg_{0.74}Ca_{0.26}O$ as the gate dielectric for 4H-SiC possibly leading to comparable or reduced leakage current that is found in devices centered on MgO/4H-SiC interface.

Table 6.3: The band gaps (E_g^{HSE}) obtained from HSE calculations of bulk dielectrics (E_g^{HSE} of $Mg_{0.74}Ca_{0.26}O$ is obtained from Vegard's law), valence (ΔE_V) and conduction (ΔE_C) band offsets calculated for MgO (111)/4H-SiC and $Mg_{0.74}Ca_{0.26}O$/4H-SiC.

interface	E_g^{HSE} (eV)	ΔE_V	ΔE_C
MgO (111)/4H-SiC	7.7	2.0	2.5
$Mg_{0.74}Ca_{0.26}O$/4H-SiC	7.3	2.5	1.6

Chapter 7

Summary and Outlook

4H-SiC MOSFETs suffer from low channel mobility that is primarily attributed to the poor 4H-SiC/SiO_2 interface quality. Various chemical treatments have been adopted to reduce the interface defect densities, the channel mobility is still low. Alternatively, high-κ dielectrics with suitable band gaps offer another possibility to replace the conventional SiO_2 as gate insulators.

In Chapter 3, we characterize the role of nitrogen near the the 4H-SiC (0001)/SiO_2 interfaces using first-principles calculations within the density functional theory (DFT). To this end, we emulate the 4H-SiC/SiO_2 interfaces and analyze their properties in terms of composition and geometry. Our results show that addition of N atoms, in quantities and bonding configurations consistent with experiments, favors a Si-rich transition region that compensates the Si density mismatch between SiC and oxide. This change explains the unexpected electron density reduction near the interface observed in x-ray reflectivity (XRR) prior to nitridation. We further correlate nitridation to the band structure and local strain of these interfaces. We find that N stabilizes the interface by reducing strain with no introduction of interface states.

In Chapter 4, we are first to conduct a systematical study to describe the high throughput screening of alternative dielectrics from alkaline earth metal dihalides (AX_2, where A = Mg, Ca, Sr and Ba and X = F, Cl, Br and I) to replace SiO_2 as the gate dielectric for 4H-SiC. The structural and electronic properties of AX_2 are analyzed using first principles calculations within the DFT, Through analysis of their formation energies, the most stable AX_2 crystal structures of AX_2 crystals are identified. The band gaps of the stable structures are evaluated using different approximations of exchange-correlation functional. As a result, HSE calculations produce more consistent band gaps with experiments in contrast to the band gaps underestimated

by GGA calculations. Furthermore, the dielectric constants are computed within density functional perturbation theory using three different approximations in the DFT. We find that the dielectric constants calculated from GGA including dispersion forces highly agree with those calculated from local density approximation (LDA). Based on our results, the most promising candidate high-κ dielectrics are determined to be AF_2. Moreover, the properties of Al_2O_3 and LiF are examined using a similar approach.

In Chapter 5, we describe the interfaces formed using 4H-SiC and candidate high-κ dielectrics (Al_2O_3, LiF, MgF_2 and CaF_2) using first principles calculations within the DFT. Through analysis of the PDOS profiles of 4H-SiC/high-κ dielectric interfaces, we find the 4H-SiC surface treatments prior to deposition are beneficial for the reduction of interface defect states. Both H and N passivated Al_2O_3/4H-SiC interfaces effectively remove the mid-gap states that are attributed to C dangling bonds residing topmost SiC layer, consistent with the recent experimental findings that H_2 annealing or interfacial nitridation combined with H_2 annealing at high temperature prior to atomic layer deposition (ALD) leads to low interface trap density resulting in improved channel mobility and device stability. The monolayer O helps reduce the mid-gap states in LiF/4H-SiC and AF_x/4H-SiC (A = Ca or Mg) interfaces. We also find that the polar surfaces in the 4H-SiC/MgF_2 interface systems can significantly affect the band alignments. By incorporating intrinsic atoms, the polar instability can be resolved by modifying the charge distribution near the interface to some extent. Lastly, the band offsets for those 4H-SiC/high-κ dielectric interfaces are computed to compare with available experimental values.

In Chapter 6, the properties of MgO/4H-SiC and $Mg_xCa_{1-x}O$/4H-SiC (0001) heterostructures are characterized via first principles calculations within the DFT. Through analysis of the structural properties of $Mg_xCa_{1-x}O$ ternaries with different compositions, we identify that $Mg_{0.74}Ca_{0.26}O$ presents the lowest lattice mismatch with 4H-SiC. In addition, the band offsets of $Mg_{0.74}Ca_{0.26}O$/4H-SiC (0001) heterostructure are determined by combining electrostatic potential-based alignment method and Vegard's law. We obtain 2.5 eV for the valence band offset and 1.6 eV for the conduction band offset, roughly the same valence band offset in comparison with MgO (111)/4H-SiC and SiO_2/4H-SiC but smaller conduction band offset

than SiO_2/4H-SiC [67, 125]. Hence, more accurate estimations of valence and conduction band offsets are important for the applications of $Mg_xCa_{1-x}O$/4H-SiC (0001) systems.

Overall, our results demonstrate a strong effect of interfacial nitridation process on the properties of interfaces between 4H-SiC and SiO_2. This reveal the significance of chemical treatments and offers insights on the improvement of existing treatment methods. This work searches for alternative high-κ dielectrics from alkaline earth metal dihalides, which open the opportunity for studies of other alternative high-κ dielectrics in a similar approach.

References

[1] T. Ueda, "Reliability issues in gan and sic power devices," in *2014 IEEE international reliability physics symposium*. IEEE, 2014, pp. 3D–4.

[2] A. Imbruglia, M. Saggio, S. Cascino, A. Minotti, M. Renna, G. Gullotta, A. Lionetto, S. Primosole, J. Favre, F. Roccaforte *et al.*, "Winsic4ap: Wide band gap innovative sic for advanced power," in *2019 AEIT International Conference of Electrical and Electronic Technologies for Automotive (AEIT AUTOMOTIVE)*. IEEE, 2019, pp. 1–6.

[3] J. Jian and J. Sun, "A review of recent progress on silicon carbide for photoelectrochemical water splitting," *Solar RRL*, vol. 4, no. 7, p. 2000111, 2020.

[4] W. Choyke, "Optical properties of polytypes of sic: interband absorption, and luminescence of nitrogen-exciton complexes," in *Silicon Carbide–1968*. Elsevier, 1969, pp. S141–S152.

[5] U. Lindefelt, "Doping-induced band edge displacements and band gap narrowing in 3c–, 4h–, 6h–sic, and si," *Journal of Applied Physics*, vol. 84, no. 5, pp. 2628–2637, 1998.

[6] E. Tutorials, "Mosfet amplifier," 2022. [Online]. Available: https://www.electronics-tutorials.ws/amplifier/mosfet-amplifier.html.Accessed26June2022

[7] R. Estève, "Fabrication and characterization of 3c- and 4h-sic mosfets," Ph.D. dissertation, School of Information and Communication Technology (ICT) KTH, 2011.

[8] S. Cottenier *et al.*, "Density functional theory and the family of (l) apw-methods: a step-by-step introduction," *Instituut voor Kern-en Stralingsfysica, KU Leuven, Belgium*, vol. 4, no. 0, p. 41, 2002.

[9] W. Setyawan and S. Curtarolo, "High-throughput electronic band structure calculations: Challenges and tools," *Computational materials science*, vol. 49, no. 2, pp. 299–312, 2010.

[10] X. Li, S. Lee, M. Li, A. Ermakov, J. Medina-Ramos, T. Fister, V. Amarasinghe, T. Gustafsson, E. Garfunkel, P. Fenter, and L. C. Feldman, "Effect of nitrogen passivation on interface composition and physical stress in sio2 /sic(4h) structures," *Applied Physics Letters*, vol. 113, p. 131601, 09 2018.

[11] D. G. Schlom and J. H. Haeni, "A thermodynamic approach to selecting alternative gate dielectrics," *Mrs Bulletin*, vol. 27, no. 3, pp. 198–204, 2002.

[12] A. Siddiqui, R. Y. Khosa, and M. Usman, "High-k dielectrics for 4h-silicon carbide: Present status and future perspectives," *Journal of Materials Chemistry C*, vol. 9, no. 15, pp. 5055–5081, 2021.

[13] L. M. Tolbert, B. Ozpineci, S. K. Islam, and M. S. Chinthavali, "Wide bandgap semiconductors for utility applications," *semiconductors*, vol. 1, p. 3, 2003.

[14] F. Roccaforte, F. Giannazzo, and V. Raineri, "Nanoscale transport properties at silicon carbide interfaces," *Journal of Physics D: Applied Physics*, vol. 43, no. 22, p. 223001, 2010.

[15] J. Thomas, G. Stephan, J. Lemonnier, M. Nisar, and S. Robin, "Optical anisotropy of mgf, in its uv absorption region," *physica status solidi (b)*, vol. 56, no. 1, pp. 163–170, 1973.

[16] D. R. Lide *et al.*, *CRC Handbook of Chemistry and Physics, 84th*, ser. Electrochemical Series. CRC Press LLC, 2004.

[17] W. Pong, C. S. Inouye, and S. K. Okada, "Ultraviolet photoemission studies of baf_2 and $bacl_2$," *Phys. Rev. B*, vol. 18, pp. 4422–4425, Oct 1978. [Online]. Available: https://link.aps.org/doi/10.1103/PhysRevB.18.4422

[18] D. Roessler and W. Walker, "Electronic spectrum of crystalline lithium fluoride," *Journal of Physics and Chemistry of Solids*, vol. 28, no. 8, pp. 1507–1515, 1967.

[19] H. Gon and N. Veeraiah, "Dielectric properties of lif single crystals," *Journal of Materials Science*, vol. 16, no. 9, pp. 2571–2574, 1981.

[20] T. Kimoto and J. A. Cooper, *Fundamentals of silicon carbide technology: growth, characterization, devices and applications*. John Wiley & Sons, 2014.

[21] A. Yoshikawa, H. Matsunami, and Y. Nanishi, "Development and applications of wide bandgap semiconductors," in *Wide bandgap semiconductors*. Springer, 2007, pp. 1–24.

[22] D. A. M. Office, "Wide bandgap semiconductors: Pursuing the promise (doe/ee-0910)," *Retrieved 3 September 2014*, April 2013.

[23] P. G. Neudeck, R. S. Okojie, and L.-Y. Chen, "High-temperature electronics-a role for wide bandgap semiconductors?" *Proceedings of the IEEE*, vol. 90, no. 6, pp. 1065–1076, 2002.

[24] B. J. Baliga, *Fundamentals of power semiconductor devices*. Springer Science & Business Media, 2010.

[25] B. T. E. of Encyclopaedia, "Material science and device physics in SiC technology for high-voltage power devices," *Encyclopedia Britannica*, aug 2008. [Online]. Available: https://www.britannica.com/science/silicon-carbide.Accessed24June2022

[26] I. Institute, "Properties of silicon carbide," 2022. [Online]. Available: http://www.ioffe.ru/SVA/NSM/Semicond/SiC/.Accessed24June2022

[27] R. M. Laine and F. Babonneau, "Preceramic polymer routes to silicon carbide," *Chemistry of materials*, vol. 5, no. 3, pp. 260–279, 1993.

[28] M. Shur, S. L. Rumyantsev *et al.*, *SiC materials and devices*. World Scientific, 2006, vol. 1.

[29] M. Golio and J. Golio, *RF and microwave passive and active technologies*. CRC press, 2018.

[30] K. L. Ashley, *Analog electronics with LabVIEW*. Prentice Hall Professional, 2002.

[31] N. Saks and A. Agarwal, "Hall mobility and free electron density at the sic/sio2 interface in 4h–sic," *Applied Physics Letters*, vol. 77, no. 20, pp. 3281–3283, 2000.

[32] J. Cooper, Jr, "Advances in sic mos technology," *physica status solidi (a)*, vol. 162, no. 1, pp. 305–320, 1997.

[33] L. Lipkin and J. Palmour, "Improved oxidation procedures for reduced sio2/sic defects," *Journal of Electronic Materials*, vol. 25, no. 5, pp. 909–915, 1996.

[34] M. Cabello, V. Soler, G. Rius, J. Montserrat, J. Rebollo, and P. Godignon, "Advanced processing for mobility improvement in 4H-SiC MOSFETs: A review," *Materials Science in Semiconductor Processing*, vol. 78, pp. 22 – 31, 2018. [Online]. Available: http://www.sciencedirect.com/science/article/pii/S1369800117318978

[35] F. Roccaforte, P. Fiorenza, G. Greco, R. L. Nigro, F. Giannazzo, A. Patti, and M. Saggio, "Challenges for energy efficient wide band gap semiconductor power devices," *physica status solidi (a)*, vol. 211, no. 9, pp. 2063–2071, 2014.

[36] V. Afanasev, M. Bassler, G. Pensl, and M. Schulz, "Intrinsic sic/sio2 interface states," *physica status solidi (a)*, vol. 162, no. 1, pp. 321–337, 1997.

[37] S. Dhar, X. Chen, P. Mooney, J. Williams, and L. Feldman, "Ultrashallow defect states at sio2/4h–sic interfaces," *Applied Physics Letters*, vol. 92, no. 10, p. 102112, 2008.

[38] T. Kimoto, "Material science and device physics in SiC technology for high-voltage power devices," *Japanese Journal of Applied Physics*, vol. 54, no. 4, p. 040103, mar 2015. [Online]. Available: https://doi.org/10.7567%2Fjjap.54.040103

[39] G. Y. Chung, C.-C. Tin, J. Williams, K. McDonald, M. Di Ventra, S. Pantelides, L. Feldman, and R. Weller, "Effect of nitric oxide annealing on the interface trap densities near

the band edges in the 4h polytype of silicon carbide," *Applied Physics Letters*, vol. 76, pp. 1713–1715, 03 2000.

[40] D. Okamoto, H. Yano, T. Hatayama, and T. Fuyuki, "Removal of near-interface traps at SiO2/4H–SiC (0001) interfaces by phosphorus incorporation," *Applied Physics Letters*, vol. 96, no. 20, p. 203508, May 2010. [Online]. Available: https://aip.scitation.org/doi/10.1063/1.3432404

[41] H. Tochihara and T. Shirasawa, "The epitaxial crystalline silicon-oxynitride layer on SiC(0001): Formation of an ideal SiC–insulator interface," *Progress in Surface Science*, vol. 86, no. 11, pp. 295 – 327, 2011. [Online]. Available: http://www.sciencedirect.com/science/article/pii/S0079681611000347

[42] R. Kosugi, T. Umeda, and Y. Sakuma, "Fixed nitrogen atoms in the sio2/sic interface region and their direct relationship to interface trap density," *Applied Physics Letters*, vol. 99, no. 18, p. 182111, 2011.

[43] Y. Xu, X. Zhu, H. D. Lee, C. Xu, S. M. Shubeita, A. C. Ahyi, Y. Sharma, J. R. Williams, W. Lu, S. Ceesay, B. R. Tuttle, A. Wan, S. T. Pantelides, T. Gustafsson, E. L. Garfunkel, and L. C. Feldman, "Atomic state and characterization of nitrogen at the SiC/SiO $_2$ interface," *Journal of Applied Physics*, vol. 115, no. 3, p. 033502, Jan. 2014. [Online]. Available: http://aip.scitation.org/doi/10.1063/1.4861626

[44] A. Chanthaphan, T. Hosoi, T. Shimura, and H. Watanabe, "Study of sio2/4h-sic interface nitridation by post-oxidation annealing in pure nitrogen gas," *AIP Advances*, vol. 5, no. 9, p. 097134, 2015.

[45] S. Dhar, S. Wang, J. R. Williams, S. T. Pantelides, and L. C. Feldman, "Interface passivation for silicon dioxide layers on silicon carbide," *MRS bulletin*, vol. 30, no. 4, pp. 288–292, 2005.

[46] T. Umeda, K. Esaki, R. Kosugi, K. Fukuda, T. Ohshima, N. Morishita, and J. Isoya, "Behavior of nitrogen atoms in sic-sio2 interfaces studied by electrically detected magnetic resonance," *Applied Physics Letters*, vol. 99, no. 14, p. 142105, 2011.

[47] C. Cochrane, P. M. Lenahan, and A. Lelis, "The effect of nitric oxide anneals on silicon vacancies at and very near the interface of 4h sic metal oxide semiconducting field effect transistors using electrically detected magnetic resonance," *Applied Physics Letters*, vol. 102, no. 19, p. 193507, 2013.

[48] R. K. Chanana, "High density of deep acceptor traps near the 4h-sic conduction band limits surface mobility and dielectric breakdown field in an n-channel 4h-sic mosfet," *IOSR-JEEE*, vol. 14, no. 4, pp. 1–8, 2019.

[49] J. R. Williams, G. Chung, C. C. Tin, K. McDonald, D. Farmer, R. Chanana, R. A. Weller, S. T. Pantelides, O. Holland, M. K. Das *et al.*, "Passivation of the 4h-sic/sio2 interface with nitric oxide," in *Materials Science Forum*, vol. 389. Trans Tech Publ, 2002, pp. 967–972.

[50] M. Okamoto, Y. Makifuchi, T. Araoka, M. Miyazato, Y. Sugahara, T. Tsutsumi, Y. Onishi, H. Kimura, S. Harada, K. Fukuda *et al.*, "Improvement of channel mobility in 4h-sic c-face mosfets by h2 rich wet re-oxidation," in *Materials Science Forum*, vol. 778. Trans Tech Publ, 2014, pp. 975–978.

[51] G. Chung, J. Williams, K. McDonald, and L. Feldman, "4h-sic oxynitridation for generation of insulating layers," *Journal of Physics: Condensed Matter*, vol. 16, no. 17, p. S1857, 2004.

[52] D. Okamoto, H. Yano, K. Hirata, T. Hatayama, and T. Fuyuki, "Improved inversion channel mobility in 4h-sic mosfets on si face utilizing phosphorus-doped gate oxide," *IEEE Electron Device Letters*, vol. 31, no. 7, pp. 710–712, 2010.

[53] H.-f. Li, S. Dimitrijev, H. B. Harrison, and D. Sweatman, "Interfacial characteristics of N2O and NO nitrided SiO2 grown on SiC by rapid thermal processing," *Applied*

Physics Letters, vol. 70, no. 15, pp. 2028–2030, Apr. 1997. [Online]. Available: http://aip.scitation.org/doi/10.1063/1.118773

[54] H. Yano, F. Katafuchi, T. Kimoto, and H. Matsunami, "Effects of Wet Oxidation/Anneal on Interface Properties of Thermally Oxidized SiO /SiC MOS System and MOSFET's," *IEEE TRANSACTIONS ON ELECTRON DEVICES*, vol. 46, no. 3, p. 8, 1999.

[55] S. Harada, R. Kosugi, J. Senzaki, W.-J. Cho, K. Fukuda, K. Arai, and S. Suzuki, "Relationship between channel mobility and interface state density in sic metal–oxide–semiconductor field-effect transistor," *Journal of Applied Physics*, vol. 91, pp. 1568–1571, 02 2002.

[56] A. Perez-Tomas, P. Brosselard, P. Godignon, J. Millan, N. Mestres, M. Jennings, J. Covington, and P. Mawby, "Field-effect mobility temperature modeling of 4h-sic metal-oxide-semiconductor transistors," *Journal of Applied Physics*, vol. 100, pp. 114 508–114 508, 12 2006.

[57] P. Jamet, S. Dimitrijev, and P. Tanner, "Effects of nitridation in gate oxides grown on 4h-sic," *Journal of Applied Physics*, vol. 90, no. 10, pp. 5058–5063, 2001.

[58] S. Dhar, A. Ahyi, J. Williams, S. Ryu, and A. Agarwal, "Temperature dependence of inversion layer carrier concentration and hall mobility in 4h-sic mosfets," *Materials Science Forum*, vol. 717-720, pp. 713–716, 05 2012.

[59] G. Chung, C. Tin, J. Williams, K. Mcdonald, R. Chanana, R. Weller, S. Pantelides, L. Feldman, O. Holland, M. Das, and J. Palmour, "Improved inversion channel mobility for 4h-sic mosfets following high temperature anneals in nitric oxide," *IEEE Electron Device Letters*, vol. 22, p. 176, 04 2001.

[60] R. Kosugi, K. Fukuda, and K. Arai, "High temperature rapid thermal oxidation and nitridation of 4h-sic in diluted n2o and no ambient," *Materials Science Forum*, vol. 483, pp. 669–672, 01 2005.

[61] Y. Wang, K. Tang, T. Khan, M. Balasubramanian, H. Naik, W. Wang, and T.-S. Chow, "The effect of gate oxide processes on the performance of 4h-sic mosfets and gate-controlled diodes," *Electron Devices, IEEE Transactions on*, vol. 55, pp. 2046 – 2053, 09 2008.

[62] J. Rozen, A. Ahyi, X. Zhu, J. Williams, and L. Feldman, "Scaling between channel mobility and interface state density in sic mosfets," *Electron Devices, IEEE Transactions on*, vol. 58, pp. 3808 – 3811, 12 2011.

[63] A. Frazzetto, F. Giannazzo, P. Fiorenza, V. Raineri, and F. Roccaforte, "Limiting mechanism of inversion channel mobility in al-implanted lateral 4h-sic metal-oxide semiconductor field-effect transistors," *Applied Physics Letters*, vol. 99, no. 7, p. 072117, 2011.

[64] P. Fiorenza, F. Giannazzo, A. Frazzetto, and F. Roccaforte, "Influence of the surface morphology on the channel mobility of lateral implanted 4h-sic (0001) metal-oxide-semiconductor field-effect transistors," *Journal of Applied Physics*, vol. 112, no. 8, p. 084501, 2012.

[65] P. Fiorenza, F. Giannazzo, L. K. Swanson, A. Frazzetto, S. Lorenti, M. S. Alessandrino, and F. Roccaforte, "A look underneath the SiO_2 /4H-SiC interface after N_2O thermal treatments," *Beilstein Journal of Nanotechnology*, vol. 4, pp. 249–254, Apr. 2013. [Online]. Available: https://www.beilstein-journals.org/bjnano/articles/4/26

[66] G. Liu, B. R. Tuttle, and S. Dhar, "Silicon carbide: A unique platform for metal-oxide-semiconductor physics," *Applied Physics Reviews*, vol. 2, no. 2, p. 021307, 2015.

[67] T.-H. Kil and K. Kita, "Anomalous band alignment change of sio2/4h–sic (0001) and (000–1) mos capacitors induced by no-poa and its possible origin," *Applied Physics Letters*, vol. 116, no. 12, p. 122103, 2020.

[68] A. Chanthaphan, T. Hosoi, T. Shimura, and H. Watanabe, "Study of sio2/4h-sic interface nitridation by post-oxidation annealing in pure nitrogen gas," *AIP Advances*, vol. 5, no. 9, p. 097134, 2015.

[69] T. Kobayashi, J. Suda, and T. Kimoto, "Reduction of interface state density in sic (0001) mos structures by post-oxidation ar annealing at high temperature," *AIP Advances*, vol. 7, no. 4, p. 045008, 2017.

[70] S. Asaba, T. Schimizu, Y. Nakabayashi, S. Fukatsu, T. Ito, and R. Iijima, "Novel gate insulator process by nitrogen annealing for si-face sic mosfet with high-mobility and high-reliability," *Materials Science Forum*, vol. 924, pp. 457–460, 06 2018.

[71] L. Lipkin and J. Palmour, "Insulator investigation on sic for improved reliability," *IEEE Transactions on Electron Devices*, vol. 46, no. 3, pp. 525–532, 1999.

[72] P. Fiorenza, M. Vivona, S. Di Franco, E. Smecca, S. Sanzaro, A. Alberti, M. Saggio, and F. Roccaforte, "Properties of al2o3 thin films deposited on 4h-sic by reactive ion sputtering," *Materials Science in Semiconductor Processing*, vol. 93, pp. 290–294, 2019.

[73] M. Born and R. Oppenheimer, "Zur quantentheorie der molekeln," *Annalen der Physik*, vol. 389, no. 20, pp. 457–484, 1927. [Online]. Available: https://onlinelibrary.wiley.com/doi/abs/10.1002/andp.19273892002

[74] D. R. Hartree, "The wave mechanics of an atom with a non-coulomb central field. part i. theory and methods," in *Mathematical Proceedings of the Cambridge Philosophical Society*, vol. 24, no. 1. Cambridge university press, 1928, pp. 89–110.

[75] J. C. Slater, "The self consistent field and the structure of atoms," *Physical Review*, vol. 32, no. 3, p. 339, 1928.

[76] J. Gaunt, "A theory of hartree's atomic fields," in *Mathematical Proceedings of the Cambridge Philosophical Society*, vol. 24, no. 2. Cambridge University Press, 1928, pp. 328–342.

[77] J. C. Slater, "Note on hartree's method," *Physical Review*, vol. 35, no. 2, p. 210, 1930.

[78] V. Fock, "Selfconsistent field "mit austausch für natrium," *Zeitschrift für Physik*, vol. 62, no. 11, pp. 795–805, 1930.

[79] P. Hohenberg and W. Kohn, "Inhomogeneous electron gas," *Physical review*, vol. 136, no. 3B, p. B864, 1964.

[80] W. Kohn and L. J. Sham, "Self-consistent equations including exchange and correlation effects," *Physical review*, vol. 140, no. 4A, p. A1133, 1965.

[81] L. J. Sham and W. Kohn, "One-particle properties of an inhomogeneous interacting electron gas," *Physical Review*, vol. 145, no. 2, p. 561, 1966.

[82] P. A. Dirac, "Note on exchange phenomena in the thomas atom," in *Mathematical proceedings of the Cambridge philosophical society*, vol. 26, no. 3. Cambridge University Press, 1930, pp. 376–385.

[83] E. Wigner, "On the interaction of electrons in metals," *Physical Review*, vol. 46, no. 11, p. 1002, 1934.

[84] M. Gell-Mann and K. A. Brueckner, "Correlation energy of an electron gas at high density," *Physical Review*, vol. 106, no. 2, p. 364, 1957.

[85] D. M. Ceperley and B. J. Alder, "Ground state of the electron gas by a stochastic method," *Physical review letters*, vol. 45, no. 7, p. 566, 1980.

[86] S. H. Vosko, L. Wilk, and M. Nusair, "Accurate spin-dependent electron liquid correlation energies for local spin density calculations: a critical analysis," *Canadian Journal of physics*, vol. 58, no. 8, pp. 1200–1211, 1980.

[87] J. P. Perdew and A. Zunger, "Self-interaction correction to density-functional approximations for many-electron systems," *Physical Review B*, vol. 23, no. 10, p. 5048, 1981.

[88] L. A. Cole and J. Perdew, "Calculated electron affinities of the elements," *Physical Review A*, vol. 25, no. 3, p. 1265, 1982.

[89] J. P. Perdew, J. A. Chevary, S. H. Vosko, K. A. Jackson, M. R. Pederson, D. J. Singh, and C. Fiolhais, "Atoms, molecules, solids, and surfaces: Applications of the generalized

gradient approximation for exchange and correlation," *Physical review B*, vol. 46, no. 11, p. 6671, 1992.

[90] J. P. Perdew, K. Burke, and M. Ernzerhof, "Generalized gradient approximation made simple," *Physical Review Letters*, vol. 77, no. 18, p. 3865, 1996.

[91] L. He, F. Liu, G. Hautier, M. J. Oliveira, M. A. Marques, F. D. Vila, J. Rehr, G.-M. Rignanese, and A. Zhou, "Accuracy of generalized gradient approximation functionals for density-functional perturbation theory calculations," *Physical Review B*, vol. 89, no. 6, p. 064305, 2014.

[92] P. Haas, F. Tran, and P. Blaha, "Calculation of the lattice constant of solids with semilocal functionals," *Physical Review B*, vol. 79, no. 8, p. 085104, 2009.

[93] J. Heyd, G. E. Scuseria, and M. Ernzerhof, "Hybrid functionals based on a screened coulomb potential," *The Journal of chemical physics*, vol. 118, no. 18, pp. 8207–8215, 2003.

[94] D. L. Strout and G. E. Scuseria, "A quantitative study of the scaling properties of the hartree–fock method," *The Journal of chemical physics*, vol. 102, no. 21, pp. 8448–8452, 1995.

[95] J. C. Slater, "Quantum theory of molecules and solids, vol. 1: Electronic structure of molecules," *American Journal of Physics*, vol. 32, no. 1, pp. 65–66, 1964.

[96] J. Singleton, *Band theory and electronic properties of solids*. Oxford University Press, 2001, vol. 2.

[97] A. Bravais, "Les systemes formes par des pointes distribues regulierement sur un plan ou dans l'espace," *J. Ecole. Polytech.*, pp. 1–128, 1850.

[98] C. Kittel, P. McEuen, and P. McEuen, *Introduction to solid state physics*. Wiley New York, 1996, vol. 8.

[99] L. Brillouin, "Les électrons dans les métaux et le classement des ondes de de broglie correspondantes," *Comptes Rendus Hebdomadaires des Séances de l'Académie des Sciences*, vol. 191, p. 292, 1930.

[100] A. Alkauskas, P. Broqvist, F. Devynck, and A. Pasquarello, "Band Offsets at Semiconductor-Oxide Interfaces from Hybrid Density Functional Calculations," *Physical Review Letters*, vol. 101, no. 10, p. 106802, Sep 2008. [Online]. Available: http://arxiv.org/abs/0809.3119

[101] L. Weston, H. Tailor, K. Krishnaswamy, L. Bjaalie, and C. Van de Walle, "Accurate and efficient band-offset calculations from density functional theory," *Computational Materials Science*, vol. 151, pp. 174–180, 08 2018.

[102] J. Heyd, G. Scuseria, and M. Ernzerhof, "Erratum: "hybrid functionals based on a screened coulomb potential" [j. chem. phys.118, 8207 (2003)]," *Journal of Chemical Physics*, vol. 124, p. 9906, 05 2006.

[103] M. Chan and G. Ceder, "Efficient band gap prediction for solids," *Physical Review Letters*, vol. 105, no. 19, p. 196403, 2010.

[104] P. Giannozzi, O. Andreussi, T. Brumme, O. Bunau, M. B. Nardelli, M. Calandra, R. Car, C. Cavazzoni, D. Ceresoli, M. Cococcioni, N. Colonna, I. Carnimeo, A. D. Corso, S. de Gironcoli, P. Delugas, R. A. DiStasio, A. Ferretti, A. Floris, G. Fratesi, G. Fugallo, R. Gebauer, U. Gerstmann, F. Giustino, T. Gorni, J. Jia, M. Kawamura, H.-Y. Ko, A. Kokalj, E. Küçükbenli, M. Lazzeri, M. Marsili, N. Marzari, F. Mauri, N. L. Nguyen, H.-V. Nguyen, A. O. de-la Roza, L. Paulatto, S. Poncé, D. Rocca, R. Sabatini, B. Santra, M. Schlipf, A. P. Seitsonen, A. Smogunov, I. Timrov, T. Thonhauser, P. Umari, N. Vast, X. Wu, and S. Baroni, "Advanced capabilities for materials modelling with quantum ESPRESSO," *Journal of Physics: Condensed Matter*, vol. 29, no. 46, p. 465901, oct 2017. [Online]. Available: https://doi.org/10.1088%2F1361-648x%2Faa8f79

[105] T. Thonhauser, V. R. Cooper, S. Li, A. Puzder, P. Hyldgaard, and D. C. Langreth, "Van der waals density functional: Self-consistent potential and the nature of the van

der waals bond," *Phys. Rev. B*, vol. 76, p. 125112, Sep 2007. [Online]. Available: https://link.aps.org/doi/10.1103/PhysRevB.76.125112

[106] K. Berland, V. R. Cooper, K. Lee, E. Schröder, T. Thonhauser, P. Hyldgaard, and B. I. Lundqvist, "van der waals forces in density functional theory: a review of the vdw-df method," *Reports on Progress in Physics*, vol. 78, no. 6, p. 066501, 2015.

[107] M. Dion, H. Rydberg, E. Schröder, D. C. Langreth, and B. I. Lundqvist, "Van der waals density functional for general geometries," *Phys. Rev. Lett.*, vol. 92, p. 246401, Jun 2004. [Online]. Available: https://link.aps.org/doi/10.1103/PhysRevLett.92.246401

[108] V. R. Cooper, "Van der waals density functional: An appropriate exchange functional," *Phys. Rev. B*, vol. 81, p. 161104, Apr 2010. [Online]. Available: https://link.aps.org/doi/10.1103/PhysRevB.81.161104

[109] G. Kresse and D. Joubert, "From ultrasoft pseudopotentials to the projector augmented-wave method," *Physical Review B*, vol. 59, no. 3, p. 1758, 1999.

[110] L. Bengtsson, "Dipole correction for surface supercell calculations," *Physical Review B*, vol. 59, no. 19, p. 12301, 1999.

[111] S. Plimpton, "Fast parallel algorithms for short-range molecular dynamics," *Journal of computational physics*, vol. 117, no. 1, pp. 1–19, 1995, http://lammps.sandia.gov.

[112] T. Umeda, M. Okamoto, R. Kosugi, S. Harada, R. Arai, Y. Sato, T. Makino, and T. Ohshima, "Sic mos interface states: Difference between si face and c face," *ECS Transactions*, vol. 58, no. 7, p. 55, 2013.

[113] P. Deák, J. M. Knaup, T. Hornos, C. Thill, A. Gali, and T. Frauenheim, "The mechanism of defect creation and passivation at the SiC/SiO_2 interface," *Journal of Physics D: Applied Physics*, vol. 40, no. 20, pp. 6242–6253, Oct. 2007. [Online]. Available: http://stacks.iop.org/0022-3727/40/i=20/a=S09?key=crossref.d7bf69efe0929a290f3d6d9403a848d9

[114] F. Devynck, F. Giustino, P. Broqvist, and A. Pasquarello, "Structural and electronic properties of an abrupt 4h-sic (0001)/sio2 interface model: Classical molecular dynamics simulations and density functional calculations," *Physical Review B*, vol. 76, no. 7, p. 075351, 2007.

[115] T. Shirasawa, K. Hayashi, S. Mizuno, S. Tanaka, K. Nakatsuji, F. Komori, and H. Tochihara, "Epitaxial silicon oxynitride layer on a 6 h- sic (0001) surface," *Physical Review Letters*, vol. 98, no. 13, p. 136105, 2007.

[116] D. Ettisserry, N. Goldsman, A. Akturk, and A. Lelis, "Mechanisms of nitrogen incorporation at 4h-sic/sio2 interface during nitric oxide passivation – a first principles study," *Materials Science Forum*, vol. 858, pp. 465–468, 05 2016.

[117] T. Kaneko, N. Tajima, T. Yamasaki, J. Nara, T. Schimizu, K. Kato, and T. Ohno, "First-principles modeling of defect-free abrupt SiC/SiO $_2$ interfaces on *a* - and *m* -face 4H-SiC," *Applied Physics Express*, vol. 11, no. 10, p. 101304, Oct. 2018. [Online]. Available: http://stacks.iop.org/1882-0786/11/i=10/a=101304?key=crossref.cbc5a90599a7a6eed4c666c4efcda8d9

[118] L. Johansson, F. Owman, and P. Mårtensson, "High-resolution core-level study of 6h-sic (0001)," *Physical Review B*, vol. 53, no. 20, p. 13793, 1996.

[119] N. Sieber, T. Seyller, R. Graupner, L. Ley, R. Mikalo, P. Hoffmann, D. R. Batchelor, and D. Schmeißer, "PES and LEED study of hydrogen- and oxygen-terminated 6H–SiC(0 0 0 1) and (000$\bar{1}$) surfaces," *Applied Surface Science*, vol. 184, no. 1, pp. 278 – 283, 2001. [Online]. Available: http://www.sciencedirect.com/science/article/pii/S0169433201005086

[120] H. J. Monkhorst and J. D. Pack, "Special points for brillouin-zone integrations," *Physical Review B*, vol. 13, no. 12, p. 5188, 1976.

[121] A. C. T. V. Duin, R. Strachan, S. Stewman, Q. Zhang, X. Xu, and W. A. Goddard, "Reaxff sio reactive force field for silicon and silicon oxide systems," *J. Phys. Chem. A*, vol. 107, p. 3803, 2003.

[122] J. C. Fogarty, H. M. Aktulga, A. Y. Grama, A. C. Van Duin, and S. A. Pandit, "A reactive molecular dynamics simulation of the silica-water interface," *The Journal of chemical physics*, vol. 132, no. 17, p. 174704, 2010.

[123] C. Freysoldt, B. Grabowski, T. Hickel, J. Neugebauer, G. Kresse, A. Janotti, and C. G. Van de Walle, "First-principles calculations for point defects in solids," *Reviews of Modern Physics*, vol. 86, no. 1, pp. 253–305, Mar. 2014. [Online]. Available: https://link.aps.org/doi/10.1103/RevModPhys.86.253

[124] T. Kobayashi and Y.-i. Matsushita, "Structure and energetics of carbon defects in sic (0001)/sio2 systems at realistic temperatures: Defects in sic, sio2, and at their interface," *Journal of Applied Physics*, vol. 126, no. 14, p. 145302, 2019.

[125] V. V. Afanas'ev, F. Ciobanu, S. Dimitrijev, G. Pensl, and A. Stesmans, "Band alignment and defect states at SiC/oxide interfaces," *Journal of Physics: Condensed Matter*, vol. 16, no. 17, pp. S1839–S1856, apr 2004. [Online]. Available: https://doi.org/10.1088%2F0953-8984%2F16%2F17%2F019

[126] D. Hamann, "Energetics of silicon suboxides," *Physical Review B*, vol. 61, no. 15, p. 9899, 2000.

[127] F. Roccaforte, P. Fiorenza, G. Greco, R. L. Nigro, F. Giannazzo, F. Iucolano, and M. Saggio, "Emerging trends in wide band gap semiconductors (sic and gan) technology for power devices," *Microelectronic Engineering*, vol. 187, pp. 66–77, 2018.

[128] Y. Y. Illarionov, A. G. Banshchikov, D. K. Polyushkin, S. Wachter, T. Knobloch, M. Thesberg, M. I. Vexler, M. Waltl, M. Lanza, N. S. Sokolov *et al.*, "Reliability of scalable mos2 fets with 2 nm crystalline caf2 insulators," *2D Materials*, vol. 6, no. 4, p. 045004, 2019.

[129] Y. Y. Illarionov, A. G. Banshchikov, D. K. Polyushkin, S. Wachter, T. Knobloch, M. Thesberg, L. Mennel, M. Paur, M. Stöger-Pollach, A. Steiger-Thirsfeld *et al.*, "Ultrathin calcium fluoride insulators for two-dimensional field-effect transistors," *Nature Electronics*, vol. 2, no. 6, pp. 230–235, 2019.

[130] S. Vishwanath, X. Liu, S. Rouvimov, P. C. Mende, A. Azcatl, S. McDonnell, R. M. Wallace, R. M. Feenstra, J. K. Furdyna, D. Jena *et al.*, "Comprehensive structural and optical characterization of mbe grown mose2 on graphite, caf2 and graphene," *2D Materials*, vol. 2, no. 2, p. 024007, 2015.

[131] S. Vishwanath, A. Sundar, X. Liu, A. Azcatl, E. Lochocki, A. R. Woll, S. Rouvimov, W. S. Hwang, N. Lu, X. Peng *et al.*, "Mbe growth of few-layer 2h-mote2 on 3d substrates," *Journal of Crystal Growth*, vol. 482, pp. 61–69, 2018.

[132] L. Sang, M. Liao, Y. Koide, and M. Sumiya, "High-performance metal-semiconductor-metal ingan photodetectors using caf2 as the insulator," *Applied Physics Letters*, vol. 98, no. 10, p. 103502, 2011.

[133] C. Deiter, M. Bierkandt, A. Klust, C. Kumpf, Y. Su, O. Bunk, R. Feidenhans, and J. Wollschläger, "Structural transitions and relaxation processes during the epitaxial growth of ultrathin caf2 films on si (111)," *Physical Review B*, vol. 82, no. 8, p. 085449, 2010.

[134] J. Harada, I. Takahashi, Y. Itoh, N. Sokolov, N. Yakovlev, Y. Shusterman, and J. Alvarez, "X-ray scattering from surfaces and interfaces and its application to the characterization of caf2si (111) interfaces," *Journal of crystal growth*, vol. 163, no. 1-2, pp. 31–38, 1996.

[135] T. Bischoff, I. Reshetnyak, and A. Pasquarello, "Band alignment at the caf2/si (111) interface through advanced electronic structure calculations," *Physical Review B*, vol. 101, no. 23, p. 235302, 2020.

[136] S. Curtarolo, W. Setyawan, G. L. W. Hart, M. Jahnatek, R. V. Chepulskii, R. H. Taylor, S. Wang, J. Xue, K. Yang, O. Levy, M. J. Mehl, H. T. Stokes, D. O. Demchenko,

and D. Morgan, "AFLOW: An automatic framework for high-throughput materials discovery," *Computational Materials Science*, vol. 58, pp. 218 – 226, 2012. [Online]. Available: http://www.sciencedirect.com/science/article/pii/S0927025612000717

[137] X. Gonze and C. Lee, "Dynamical matrices, born effective charges, dielectric permittivity tensors, and interatomic force constants from density-functional perturbation theory," *Physical Review B*, vol. 55, no. 16, p. 10355, 1997.

[138] J. P. Perdew, E. R. McMullen, and A. Zunger, "Density-functional theory of the correlation energy in atoms and ions: A simple analytic model and a challenge," *Phys. Rev. A*, vol. 23, pp. 2785–2789, Jun 1981. [Online]. Available: https://link.aps.org/doi/10.1103/PhysRevA.23.2785

[139] J. P. Perdew, K. Burke, and M. Ernzerhof, "Generalized gradient approximation made simple," *Phys. Rev. Lett.*, vol. 77, pp. 3865–3868, Oct 1996. [Online]. Available: https://link.aps.org/doi/10.1103/PhysRevLett.77.3865

[140] K. Yim, Y. Yong, J. Lee, K. Lee, H.-H. Nahm, J. Yoo, C. Lee, C. S. Hwang, and S. Han, "Novel high-κ dielectrics for next-generation electronic devices screened by automated ab initio calculations," *NPG Asia Materials*, vol. 7, no. 6, pp. e190–e190, 2015.

[141] S. Dhar, O. Seitz, M. D. Halls, S. Choi, Y. J. Chabal, and L. C. Feldman, "Chemical Properties of Oxidized Silicon Carbide Surfaces upon Etching in Hydrofluoric Acid," *Journal of the American Chemical Society*, vol. 131, no. 46, pp. 16 808–16 813, Nov. 2009. [Online]. Available: https://pubs.acs.org/doi/10.1021/ja9053465

[142] S. Thomas, Y. Sharma, M. Crouch, C. Fisher, A. Perez-Tomas, M. Jennings, and P. Mawby, "Enhanced field effect mobility on 4h-sic by oxidation at 1500 c," *IEEE Journal of the Electron Devices Society*, vol. 2, no. 5, pp. 114–117, 2014.

[143] K. Fukuda, S. Suzuki, T. Tanaka, and K. Arai, "Reduction of interface-state density in 4h–sic n-type metal–oxide–semiconductor structures using high-temperature hydrogen annealing," *Applied Physics Letters*, vol. 76, no. 12, pp. 1585–1587, 2000.

[144] W.-J. Cho, R. Kosugi, K. Fukuda, K. Arai, and S. Suzuki, "Improvement of charge trapping by hydrogen post-oxidation annealing in gate oxide of 4h–sic metal–oxide–semiconductor capacitors," *Applied Physics Letters*, vol. 77, no. 8, pp. 1215–1217, 2000.

[145] A. Renz, O. Vavasour, P. Gammon, F. Li, T. Dai, M. Antoniou, G. Baker, E. Bashar, N. Grant, J. Murphy *et al.*, "The improvement of atomic layer deposited sio2/4h-sic interfaces via a high temperature forming gas anneal," *Materials Science in Semiconductor Processing*, vol. 122, p. 105527, 2021.

[146] T. Hatayama, S. Hino, N. Miura, T. Oomori, and E. Tokumitsu, "Remarkable increase in the channel mobility of sic-mosfets by controlling the interfacial sio2 layer between al2o3 and sic," *IEEE transactions on electron devices*, vol. 55, no. 8, pp. 2041–2045, 2008.

[147] F. Arith, J. Urresti, K. Vasilevskiy, S. Olsen, N. Wright, and A. O'Neill, "Increased mobility in enhancement mode 4h-sic mosfet using a thin sio2/al2o3 gate stack," *IEEE Electron Device Letters*, vol. 39, no. 4, pp. 564–567, 2018.

[148] J. Urresti, F. Arith, S. Olsen, N. Wright, and A. O'Neill, "Design and analysis of high mobility enhancement-mode 4h-sic mosfets using a thin-sio2/al2o3 gate-stack," *IEEE Transactions on Electron Devices*, vol. 66, no. 4, pp. 1710–1716, 2019.

[149] L. Huang and X. Gu, "Effects of sacrificial oxidation on surface properties of n-and p-type 4h-sic: implications for metal contact behaviors," *Semiconductor Science and Technology*, vol. 34, no. 1, p. 015011, 2018.

[150] H. Tsuchida, I. K. I. Kamata, and K. I. K. Izumi, "Si-h bonds on the 6h-sic (0001) surface after h2 annealing," *Japanese journal of applied physics*, vol. 36, no. 6A, p. L699, 1997.

[151] H. Tsuchida, I. Kamata, and K. Izumi, "Infrared spectroscopy of hydrides on the 6h-sic surface," *Applied physics letters*, vol. 70, no. 23, pp. 3072–3074, 1997.

[152] ——, "Infrared attenuated total reflection spectroscopy of 6h-sic (0001) and (000$\bar{1}$) surfaces," *Journal of applied physics*, vol. 85, no. 7, pp. 3569–3575, 1999.

[153] N. Sieber, B. Mantel, T. Seyller, J. Ristein, L. Ley, T. Heller, D. R. Batchelor, and D. Schmeißer, "Electronic and chemical passivation of hexagonal 6h–sic surfaces by hydrogen termination," *Applied Physics Letters*, vol. 78, no. 9, pp. 1216–1218, 2001.

[154] T. Seyller, "Electronic properties of sic surfaces and interfaces: some fundamental and technological aspects," *Applied Physics A*, vol. 85, no. 4, pp. 371–385, 2006.

[155] I. Jayawardhena, R. Ramamurthy, D. Morisette, A. Ahyi, R. Thorpe, M. Kuroda, L. Feldman, and S. Dhar, "Effect of surface treatments on ald al2o3/4h-sic metal–oxide–semiconductor field-effect transistors," *Journal of Applied Physics*, vol. 129, no. 7, p. 075702, 2021.

[156] U. Sharopov, K. Kaur, M. Kurbanov, D. S. Saidov, S. R. Nurmatov, M. Sharipov, and B. Egamberdiev, "Comparison of electron irradiation on the formation of surface defects in situ and post thin-film lif/si (111) deposition," *Thin Solid Films*, vol. 735, p. 138902, 2021.

[157] D. Roessler and W. Walker, "Electronic spectrum and ultraviolet optical properties of crystalline mgo," *Physical Review*, vol. 159, no. 3, p. 733, 1967.

[158] O. Madelung, U. Rossler, and M. Schulz, *Non-tetrahedrally bonded elements and binary compounds*. Springer, 1998, vol. 41.

[159] T. Goodrich, Z. Cai, and K. Ziemer, "Stability of mgo (1 1 1) films grown on 6h-sic (0 0 0 1) by molecular beam epitaxy for two-step integration of functional oxides," *Applied surface science*, vol. 254, no. 10, pp. 3191–3199, 2008.

[160] C. Bondoux, P. Prené, P. Belleville, F. Guillet, S. Lambert, B. Minot, and R. Jérisian, "Mgo insulating films prepared by sol–gel route for sic substrate," *Journal of the European Ceramic Society*, vol. 25, no. 12, pp. 2795–2798, 2005.

[161] S. Heo, E. Cho, H.-I. Lee, G. S. Park, H. J. Kang, T. Nagatomi, P. Choi, and B.-D. Choi, "Band gap and defect states of mgo thin films investigated using reflection electron energy loss spectroscopy," *AIP Advances*, vol. 5, no. 7, p. 077167, 2015.

[162] B. Zhang, F. Cai, G. Sun, H. Fan, P. Zhang, H. Wei, X. Liu, S. Yang, Q. Zhu, and Z. Wang, "Valence band offset of mgo/4h-sic heterojunction measured by x-ray photoelectron spectroscopy," *Applied Physics Letters*, vol. 93, no. 7, p. 072110, 2008.

[163] R. Lewandków, M. Grodzicki, P. Mazur, and A. Ciszewski, "Properties of thin mgo films on 6h-sic and gan: Photoelectron studies." *Acta Physica Polonica, A.*, vol. 141, no. 2, 2022.

[164] J. Jacobson and E. Nixon, "Infrared dielectric response and lattice vibrations of calcium and strontium oxides," *Journal of Physics and Chemistry of Solids*, vol. 29, no. 6, pp. 967–976, 1968.

[165] B. Ul'ritsi, V. Ul'ritsi, and N. Kovalev, "Optical absorption in sro single crystals," *Fizika Tverdogo Tela*, vol. 17, no. 12, pp. 3533–3537, 1975.

[166] N. Daude, C. Jouanin, and C. Gout, "Electronic band structure of magnesium and calcium oxides," *Physical Review B*, vol. 15, no. 4, p. 2399, 1977.

[167] M. J. Weber, *CRC handbook of laser science and Technology supplement 2: optical materials*. CRC press, 2020.

[168] M. A. Bhuiyan, H. Zhou, S.-J. Chang, X. Lou, X. Gong, R. Jiang, H. Gong, E. X. Zhang, C.-H. Won, J.-W. Lim *et al.*, "Total-ionizing-dose responses of gan-based hemts with different channel thicknesses and moshemts with epitaxial mgcao as gate dielectric," *IEEE Transactions on Nuclear Science*, vol. 65, no. 1, pp. 46–52, 2017.

[169] X. Lou, H. Zhou, S. B. Kim, S. Alghamdi, X. Gong, J. Feng, X. Wang, P. D. Ye, and R. G. Gordon, "Epitaxial growth of $mg_xca_{1-x}o$ on gan by atomic layer deposition," *Nano letters*, vol. 16, no. 12, pp. 7650–7654, 2016.

[170] X. Lou, X. Gong, S. B. Kim, and R. G. Gordon, "Epitaxial growth of $mg_xca_{1-x}o$ on 4h–sic (0001) and β-ga_2o_3 ($\bar{2}01$) wide band gap semiconductors with atomic layer deposition," *Journal of Materials Research*, vol. 35, no. 7, pp. 831–839, 2020.

[171] M. Methfessel and A. Paxton, "High-precision sampling for brillouin-zone integration in metals," *Physical Review B*, vol. 40, no. 6, p. 3616, 1989.

[172] L. Vegard, "Die konstitution der mischkristalle und die raumfüllung der atome," *Zeitschrift für Physik*, vol. 5, no. 1, pp. 17–26, 1921.

[173] R. Nahory, M. Pollack, W. Johnston Jr, and R. Barns, "Band gap versus composition and demonstration of vegard's law for $in_{1-x}ca_xas_yp_{1-y}$ lattice matched to inp," *Applied Physics Letters*, vol. 33, no. 7, pp. 659–661, 1978.

[174] D. Stodilka, A. Gerger, M. Hlad, P. Kumar, B. Gila, R. Singh, C. Abernathy, S. Pearton, and F. Ren, "Alternative magnesium calcium oxide gate dielectric for silicon carbide mos application," *MRS Online Proceedings Library (OPL)*, vol. 911, 2006.

[175] B. Van Beest, G. J. Kramer, and R. Van Santen, "Force fields for silicas and aluminophosphates based on ab initio calculations," *Physical review letters*, vol. 64, no. 16, p. 1955, 1990.

[176] P. Fathi-Hafshejani, N. Azam, L. Wang, M. A. Kuroda, M. C. Hamilton, S. Hasim, and M. Mahjouri-Samani, "Two-dimensional-material-based field-effect transistor biosensor for detecting covid-19 virus (sars-cov-2)," *ACS nano*, vol. 15, no. 7, pp. 11 461–11 469, 2021.

[177] T. Tian, B. Singhana, L. E. Englade-Franklin, X. Zhai, T. R. Lee, and J. C. Garno, "Surface assembly and nanofabrication of 1, 1, 1-tris (mercaptomethyl) heptadecane on au (111) studied with time-lapse atomic force microscopy," *Beilstein journal of nanotechnology*, vol. 5, no. 1, pp. 26–35, 2014.

[178] F. Teng, K. Hu, W. Ouyang, and X. Fang, "Photoelectric detectors based on inorganic p-type semiconductor materials," *Advanced Materials*, vol. 30, no. 35, p. 1706262, 2018.

[179] B. Liu, M. Fathi, L. Chen, A. Abbas, Y. Ma, and C. Zhou, "Chemical vapor deposition growth of monolayer wse2 with tunable device characteristics and growth mechanism study," *ACS nano*, vol. 9, no. 6, pp. 6119–6127, 2015.

[180] H. Nam, B.-R. Oh, M. Chen, S. Wi, D. Li, K. Kurabayashi, and X. Liang, "Fabrication and comparison of mos2 and wse2 field-effect transistor biosensors," *Journal of Vacuum Science & Technology B, Nanotechnology and Microelectronics: Materials, Processing, Measurement, and Phenomena*, vol. 33, no. 6, p. 06FG01, 2015.

Appendices

Appendix A

Selection Criteria for Bulk SiO_2

Suitable epitaxies for the 4H-SiC (0001) and its native oxide SiO_2 are established employing a systematic approach based on DFT. We identify 31 unique SiO_2 structures from the AFLOW library [136], and compute their electronic properties (E_{uc}, E_g, and ρ_e) using the computational details provided before. The results, presented in Fig. A.1, show the DFT band gap and electron density as a function of the formation energy per formula. The latter quantity is computed relative to the case of β-cristobalite ($\delta E = E_{uc} - \bar{E}_{uc}$). As seen in Fig. A.1 (top), the structures with the formation $\delta E < 0.1$ eV have the largest DFT band gaps in a range between 5.35 and 5.8 eV, sensibly lower than experimental band gaps due to well-known DFT limitations [103]. Meanwhile, these same structures give electron densities between 0.55 and 0.75 $e^-/Å^3$.

We further restrict our search of epitaxial interfaces to structures with densities in the 0.6–0.7 $e^-/Å^3$ to match values found experimentally for amorphous silica (ρ_{exp} = 0.662 $e^-/Å^3$) in [3], as denoted by the rectangular box of Fig. A.1 (bottom). We impose an additional constraint on the lattice mismatch ($< 2\%$) between the chosen epitaxy of SiO_2 and 4H-SiC to minimize artifacts of strain and allow for sheer strain. Within these limitations we find that a suitable epitaxy is that of β-cristobalite phase of SiO_2 (ICDS 162246), which results in system sizes of approximately 250 atoms that can be analyzed within DFT. While our work mainly analyzes interfaces with this phase in the main manuscript, the results for other structures, 4H-SiC/α-quartz (ICSD 100341) and 4H-SiC/tridymite SiO_2 (ICSD 170513) interfaces, with higher strain (7% and 2%, respectively) are shown in Appendix C.

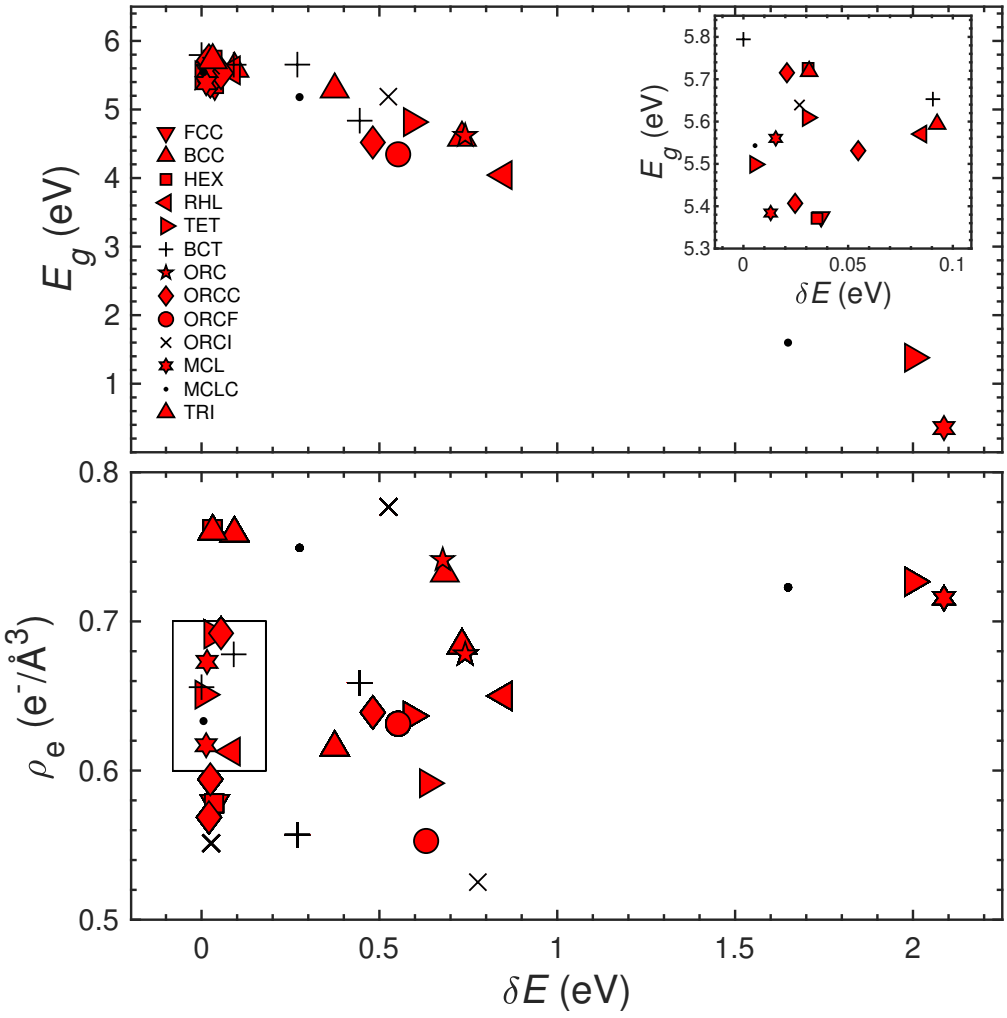

Figure A.1: (Top) DFT band gap E_g as a function of δE. Those most stable SiO_2 structures are encircled by rectangular box. The inset details the interested SiO_2. (Bottom) Electron density ρ_e as a function of δE. The structures encircled have electron density values close to experimental values.

Appendix B

Interface Formation Energy

The interfaces described in Chapter 3 correspond to the representative ones (either because they appear to be the most stable or have significance) within a more extensive study. For the β-cristobalite SiO_2 case, other interfaces that differ in their geometric configurations and do not contain N are also analyzed (models 1a and 2a). Table B.1 presents a summary of the number of atoms added/removed per supercell relative to model 1 and their corresponding interface formation energy (as described in Section II of the main manuscript). As a result of the impact of the choices of chemical potentials and the number of atoms added to/removed from reference model on the measurements of E_{if}, we considered different conditions under which the chemical potentials are computed for our models.

Table B.1: Atomic composition changes n_i for the i-species of interface models measured with respect to the reference interface (model 1). The corresponding formation energies (E_{if}) with respect to model 1 are determined under the C-poor condition (Case 1, $\mu_{\text{Si}} = E_{\text{Si}}/2$) and the Si-poor condition (Case 2, $\mu_{\text{C}} = E_{\text{C}}/4$), respectively, as described in the main manuscript. We also provide the formation energies normalized by the cross sectional area of the interface $\varepsilon_{if} \equiv E_{if}/A$.

Type	Model	n_{Si}	n_{O}	n_{N}	n_{H}	E_{if} (eV) [ε_{if} (eV/Å^2)]	
						Case 1	Case 2
Interfaces with no nitrogen	1	0	0	0	0	0	0
	1a	0	0	0	0	0.5 [0.007]	0.5 [0.007]
	2	1	2	0	0	1.5 [0.012]	1.5 [0.012]
	2a	1	2	0	0	2.5 [0.034]	2.5 [0.034]
Nitrided interfaces	3	2	-1	3	-1	-4.7 [-0.063]	-3.5 [-0.047]
	3a	2	-1	3	-1	-4.2 [-0.056]	-3.0 [-0.041]
	4	3	1	3	-1	-5.7 [-0.076]	-4.5 [-0.061]
	5	1	-3	3	-1	-3.9 [-0.052]	-2.7 [-0.036]

Table B.2: Formation energy (E_{if}) of interface model supercells determined from different choices of chemical potentials. Values are measured with respect to the reference interface (model 1).

Type	Model	E_{if}^{ref} (eV) [$\varepsilon_{if}^{\text{ref}}$ (eV/Å^2)]			
		Case 1	Case 3	Case 4	Case 5
Interfaces with	1a	0.5 [0.007]	0.5 [0.007]	0.5 [0.007]	0.5 [0.007]
no nitrogen	2	1.5 [0.020]	-7.9 [-0.106]	1.5 [0.020]	1.5 [0.020]
	2a	2.5 [0.034]	-6.9 [-0.092]	2.5 [0.034]	2.5 [0.034]
Nitrided	3	-4.7 [-0.063]	0.01 [0.000]	-20.9 [-0.281]	1.1 [0.015]
	3a	-4.2 [-0.056]	0.5 [0.007]	-20.4 [-0.274]	1.6 [0.022]
interfaces	4	-5.7 [-0.076]	-10.4 [-0.139]	-21.9 [-0.294]	0.1 [0.002]
	5	-3.9 [-0.052]	10.2 [0.137]	-20.1 [-0.270]	1.9 [0.026]

We first consider the cases of the C-poor (Case 1) and Si-poor (Case 2) conditions discussed in the main manuscript where μ_{Si} from diamond Si and μ_{C} from graphite are assumed, respectively. The values employed to determine the chemical potentials are E_{Si} (-1271.5 eV), E_{C} (-1001.7 eV), E_{SiC} (-887.1 eV), E_{SiO_2} (-1773.9 eV), E_{N} (-967.8 eV), and E_{SiH_4} (-699.2 eV) obtained as the DFT energies of diamond Si, graphite, 4H-SiC, bulk β-cristobalite SiO_2, N_2 molecule, and SiH_4 molecule per formula unit, respectively. We note that (i) the energy E_{SiO_2} accounts for the lateral strain required to form the epitaxial interface with 4H-SiC; (ii) μ_{H} obtained from SiH_4, consistent with previous work [124], yielded formation energies similar to those calculated using H_2.

In addition, we analyze other choices for μ_{O} and μ_{N} stemming from different conditions may impact our predictions, shown in Table B.2. First we consider the case of C-poor and O-rich regime (Case 3) which differs from case 1 by assuming that $\mu_{\text{O}} = E_{\text{O}}/2$, where E_{O} (-1128.7 eV) is the DFT energy of O_2 molecule per formula unit. This case gives formation energies lower than the O-poor condition for non-nitrided interfaces with high O density in the transition region (models 2 and 2a). These latter interfaces, however, do not present the electronic density reduction near the interface observed in XRR experiments, suggesting that such μ_{O} choice may not be suitable for nitridation taking place during post-oxidation annealing. Also, while evaluating the impact of the choice of μ_{N} we compare the cases of NO (Case 4), and Si_3N_4 (Case 5) against N_2 (Case 1). In these cases the nitrogen chemical potential is given by $\mu_{\text{N}} = E_{\text{NO}} - \mu_{\text{O}}$ and $\mu_{\text{N}} = (E_{\text{Si}_3\text{N}_4} - 3\,\mu_{\text{Si}})/4$, respectively, using E_{NO} (-947.6 eV) and $E_{\text{Si}_3\text{N}_4}$ (-13802.6 eV) obtained as the DFT energies of NO molecule and Si_3N_4 per formula unit. The

results, presented in Table B.2, allude to higher stability (more negative formation energies) in the case of reference chemical potential μ_{N} obtained from NO. In contrast, the choice of Si_3N_4 as a reference appears as inadequate for describing the nitridation process as it results in higher (positive) formation energies for nitrided interfaces deemed stable in Case 1 (or Case 4).

Appendix C

Electron Density Profiles

For the β-cristobalite SiO_2 case, other interfaces that differ in their geometric configurations and do not contain N are also analyzed (models 1a and 2a). A schematic representation of their interfaces is provided in Fig. C.1. They give slightly higher formation energies than models 1 and 2 (see Table B.1) but offer similar electron density profiles. It is worth mentioning that while the interfaces with high Si density (models 2 and 2a) remove the dip in the electron density profiles in the TR, they become energetically less favorable than those with less Si (models 1 and 1a). Conversely, nitrided interface with low Si density (model 5) also presents a dip but its formation energy is higher than that of models 6 and 7.

Last, we consider the case of the tridymite phase (ICSD 170513) on interfaces corresponding to a 4H-SiC slab with 7 SiC unit cells of cross section ($\sqrt{7} \times \sqrt{7}$ supercell). The TR portions of these interfaces and the corresponding density profiles are presented in Fig. C.2. These profiles produce features similar to those found in the cristobalite case where the dip in the electronic density near the interface is removed after nitrogen facilitates the increase in atomic density. In this case, the electronic density in the bulk SiO_2 is considerably lower than that of the amorphous oxide.

We note that ideally amorphous SiO_2 (a-SiO_2) would be desirable to model interfaces. The simulations of oxide slabs following the melting (4000 K for 200 ps)/quenching (5 K/ps) procedure were performed via classical molecular dynamics (MD) simulations conducted within the LAMMPS package. We employed the modified vanBeest–Kramer–vanSanten (BKS) interatomic potential [175] in systems with sizes similar to those of the crystalline silica slab of the main manuscript. In Fig. C.3(b) we show an example of results where large oscillations

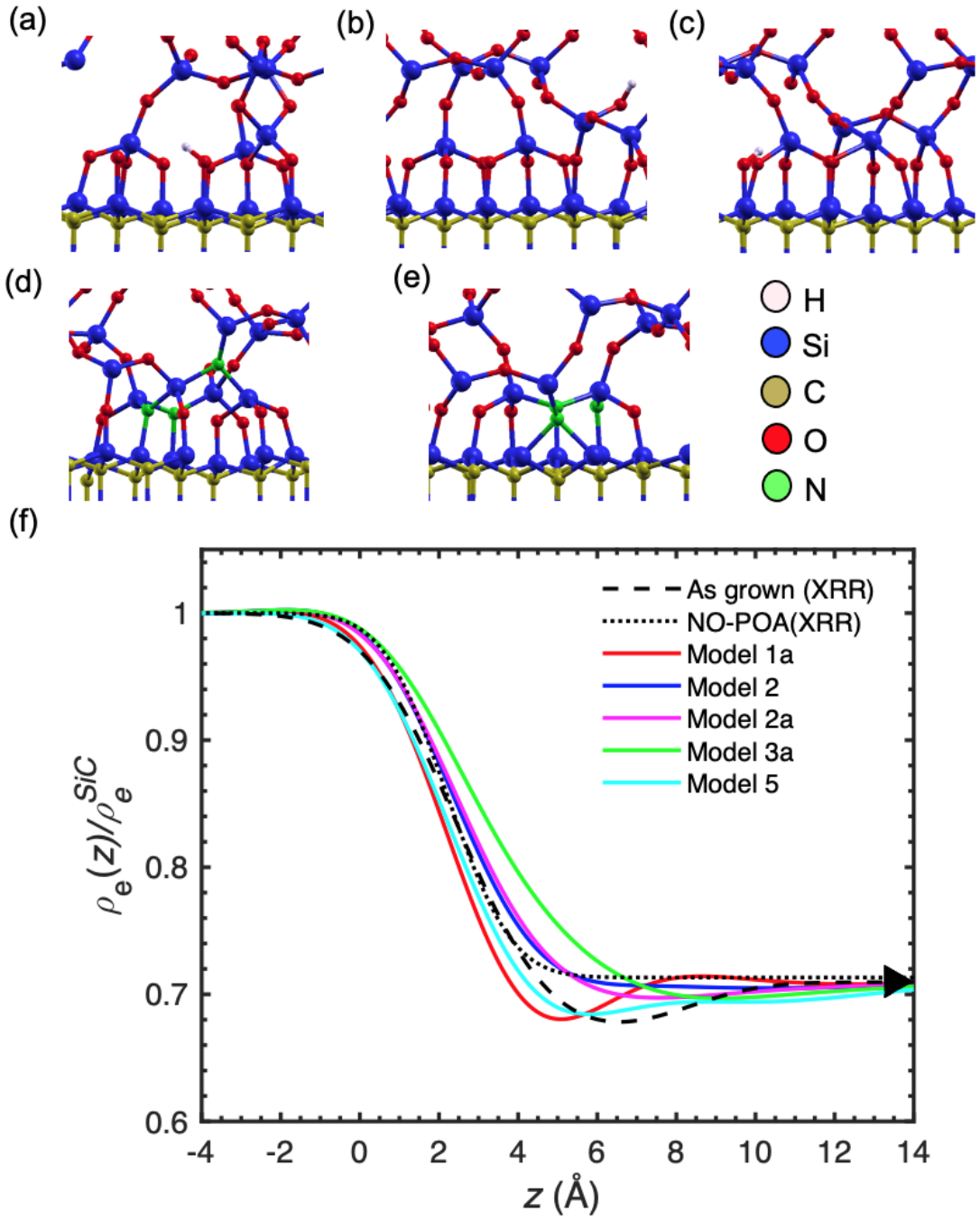

Figure C.1: Schematic representations of additional 4H-SiC/β-cristobalite SiO_2 interface models. Details of the TRs for the interfaces analyzed here (a) model 1a: interface with 3 Si atoms in TR and H-passivated monolayer O; (b) model 2: interface with 4 Si atoms in TR and H-passivated O; (c) model 2a: interface with 4 Si atoms in TR and H-passivated monolayer O; (d) model 3a: interface with 5 Si atoms in TR and a N areal density of $\sim 4 \times 10^{14}$ cm^{-2}; (e) model 5: interface with 4 Si atoms in TR and with a N areal density of $\sim 4 \times 10^{14}$ cm^{-2}. (f) Electron density profiles. The normalized electron density for bulk β-cristobalite SiO_2 is specified with triangle shape at $\sim$0.71.

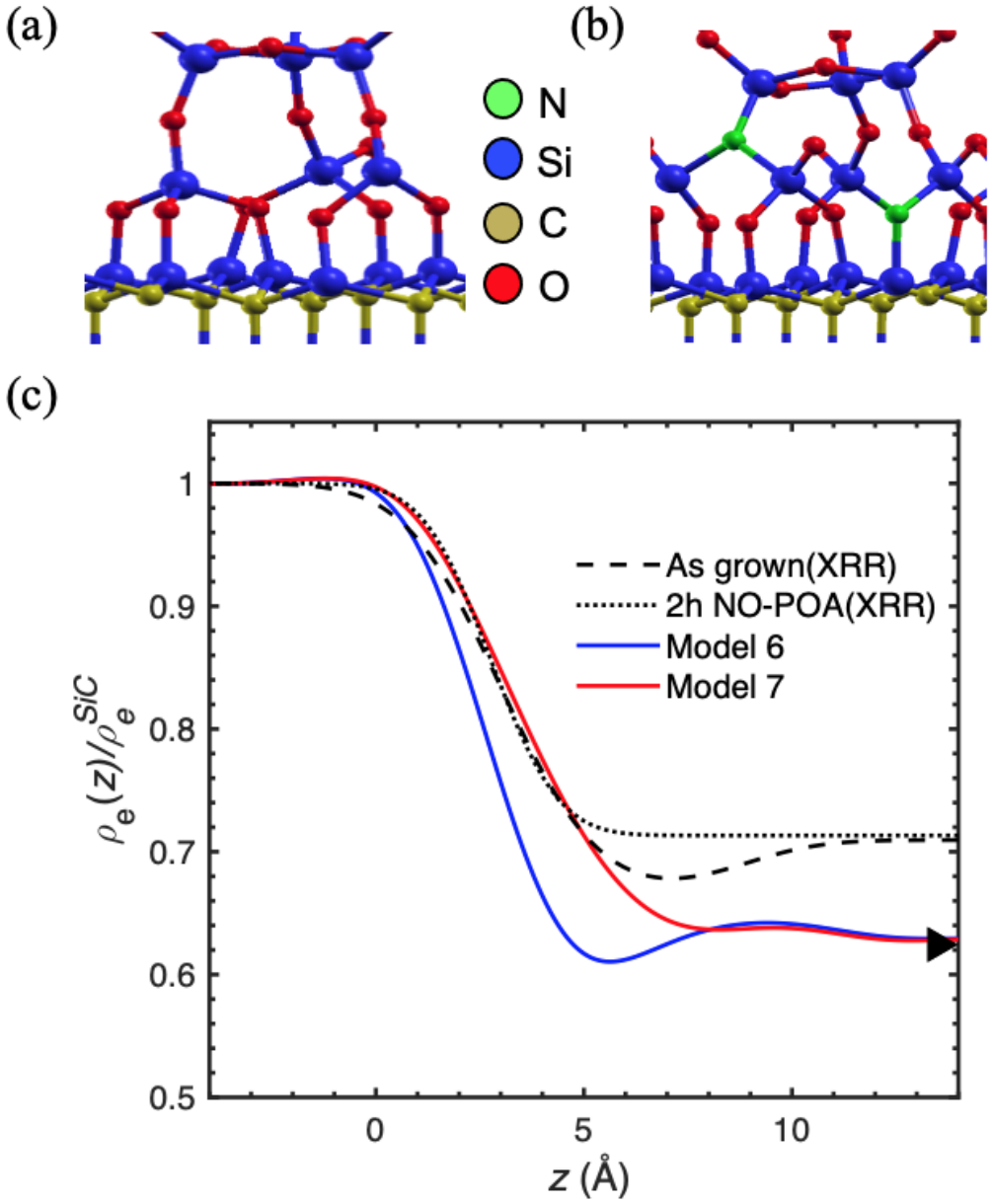

Figure C.2: Schematic representations of 4H-SiC/tridymite SiO_2 interface model. Details of the TR for interfaces analyzed here (a) model 6: interface with 3 Si atoms in TR with no N; (b) model 7: interface with 4 Si atoms in TR with a N areal density of $\sim 3.4 \times 10^{14}$ cm^{-2}. (c) Electron density profiles for models 6-7. The normalized electron density for bulk tridymite SiO_2 ($\sim$0.62) is indicated by the solid triangle.

in the macroscopic average of the electron density can be observed. These results suggest that larger in-plane slabs are required to properly describe a-SiO_2 to allow the distinction of density fluctuations in the silica with respect to those at the interface. However, due to the thickness of the interfaces considered here, these become computationally intractable within the DFT formalism.

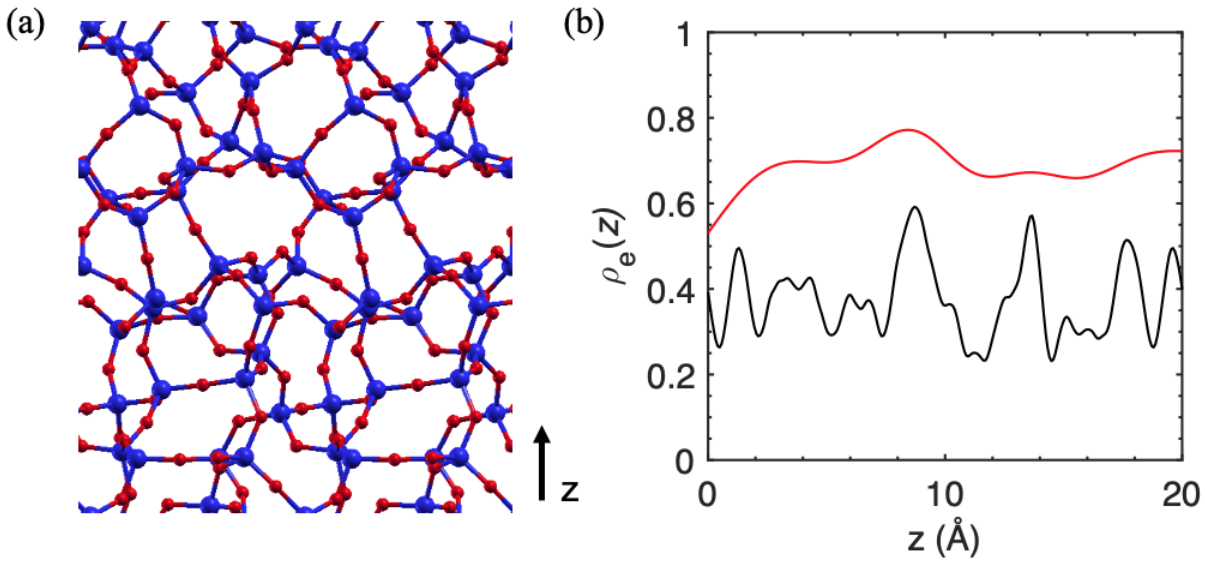

Figure C.3: (a) Schematic representation of a-SiO_2 structure obtained in this work (b)valence electron density profile (black solid line) prior to GS and the total electronic density profile (with Gaussian smoothing, detailed in next section) as a function of z.

Appendix D

Two-Dimensional-Material-Based Field-Effect Transistor Biosensor for Detecting COVID-19 Virus (SARS-CoV-2)

During the work of my dissertation, I have also investigated the interfacial properties of biosensors formed through the functionalization of transition metal dichalcogenide (TMDC) WSe_2. This work was published in ACS Nano (see Ref. [176] for more details) and our contribution is briefly described below.

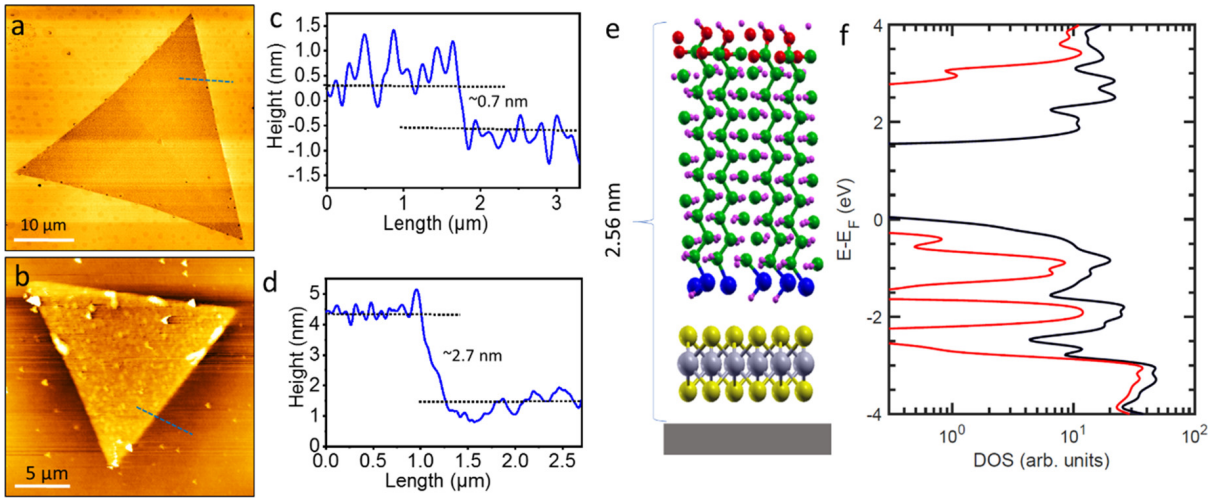

Figure D.1: AFM images and line profiles of the monolayer WSe_2 crystals prior to and after MUA functionalization. A pristine monolayer WSe_2 image (a) shows a clean and uniform topography with the line profile (c) of about $\sim$0.7 nm corresponding to a single layer crystal. MUA-functionalized monolayer WSe_2 image (b) with a line profile (d) of about 2.7 nm indicates full coverage of one vertically standing monolayer MUA on the WSe_2 crystal. (e) Schematic of MUA monolayer on top of WSe_2. (f) The density of states near the Fermi level of the full system (black) and the MUA (red) show that MUA states reside outside the band edge suggesting no charge transfer between the pristine TMDC and the molecule. Fermi level is placed (E_F) at the valence band edge of WSe_2.

We modeled the 11-mercaptoundecanoic acid (MUA) monolayer on top of the pristine WSe_2 monolayer using first-principles within the density functional theory (DFT), as presented

in Fig. D.1 (e). Consistent with the atomic force microscopy (AFM) experiments (Figs. D.1 (a)-(d)) and previous reports on the MUA length (∼1.7 nm) [177], this model yielded a height of 2.56 nm after accounting for the physical distance (2.25 nm) and vdW radii of H and Se (0.31 nm). We note that for the high-density limit of MUA molecules, interactions with adjacent molecules favor the vertical orientation that result in the MUA self-assembled monolayer (SAM). In addition, as shown in Fig. D.1 (f), analysis of the density of states (DOS) near the Fermi level indicates that the orbitals of MUA molecules reside outside the gap of the TMDC and, hence, no charge transfer is expected between the two components.

Our DFT calculations shed light on a possible mechanism leading to decreased conductivity upon MUA functionalization. Namely, the Se vacancies that result in p-type behavior of WSe_2 [178, 179] may serve as a docking site for MUA molecules (Fig. D.2 (a)). In this scenario, the Se vacancy (V_{Se}) and nearby dangling bonds become compensated by the S atom and H atom from MUA and remove the midgap states, as shown in Figs. D.2 (b) and (c). As a result of the MUA chemisorption, the p-type behavior of the device due to the vacancy filling becomes weaker [180]. The slight increase after the addition of the SARS-CoV-2 antibody and spikes is possibly due to charge transfer processes.

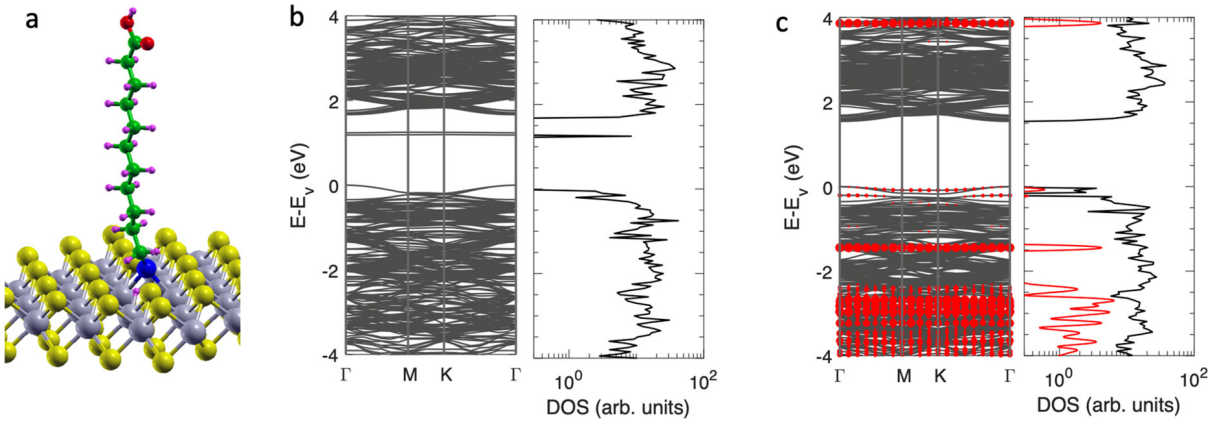

Figure D.2: Schematic of MUA adsorbed on a selenium vacancy site (V_{Se}) in the WSe_2 monolayer (a). Band structure and corresponding DOS of WSe_2 crystal with single V_{Se} (b) and with adsorbed MUA molecule (c). To facilitate comparison, energies are referred to the valence band edge (E_V). The red symbols in (c) denote the contributions from localized atomic orbitals in the MUA molecule. The defect level located at ∼1.3 eV above the valence band edge is removed upon functionalization.